SPIN TRANSFER TORQUES IN COBALT / PLATINUM BASED CHIRAL MAGNETS

A Dissertation

Presented to the Faculty of the Graduate School

of Cornell University

in Partial Fulfillment of the Requirements for the Degree of

Doctor of Philosophy

by

Jennifer Laura Grab

December 2017

SPIN TRANSFER TORQUES IN COBALT / PLATINUM BASED CHIRAL MAGNETS

Jennifer Laura Grab, Ph.D.

Cornell University 2017

Skyrmions are topologically protected quasiparticles in the form of stable spin textures in a magnetic material. Because skyrmions can be smaller than the domain size in a ferromagnet, they are promising candidates for high density information storage. Finding an efficient way to create and annihilate individual skyrmions under ambient conditions is an important first step toward realizing skyrmion-based technologies. In this dissertation, I will discuss two experiments where we attempt to create a static or dynamic skyrmion in cobalt / platinum bilayers using a spin valve like device geometry. I will also cover in detail the growth and characterization of the perpendicularly magnetized Co/Pt films necessary for this work.

The first project involves a hard Co/Pt bilayer with a strong Dzyaloshinskii Moriya Interaction, in addition to strong perpendicular anisotropy. Micromagnetic simulations have predicted that it should be possible to excite skyrmion dynamics in such systems using a spin polarized current. Although our experimental results are inconclusive, we have developed a fabrication process and measurement techniques that will be useful for future investigation of dynamics in similar materials.

The second project is related, but instead uses very soft Co/Pt bilayers, which show chiral stripe domains at zero field. We are able to separate out the behavior of the film beneath the nanopillar from the bulk film and show that the

two switch independently of each other. This indicates that there is some sort of domain, potentially a skyrmion, that we are able to control separately from the rest of the film. This project is a good first step toward controlling and creating room temperature skyrmions using spin transfer torque.

BIOGRAPHICAL SKETCH

Jennifer Laura Grab was born in Scranton, Pennsylvania to Kim and Tom Grab, a township secretary / tax collector and an excavating contractor, and grew up in a very small, rural town called Thornhurst. She was always an inquisitive child, so much so that her parents started buying her science books as soon as she was able to read. Spending a lot of time outdoors, Jen was particularly curious about the natural world. She learned the names of trees, plants, and animals and loved to study how they lived and survived. She also loved to build and design things, much preferring her K'Nex over Barbies and My Little Ponies.

Once Jen started going to school, she soon discovered she also loved math, especially when applied to the real world. After graduating valedictorian in the Class of 2006 at North Pocono High School, she attended Lafayette College, a small liberal arts school in Easton, PA, with the intent of majoring in Biochemistry. However, after one semester, she realized that biology wasn't "mathy" enough for her tastes and switched to a double major in Chemistry and Mathematics. After yet another semester, she realized she didn't like memorizing naming conventions and chemical reactions (no offense, chemists) and at last settled on a Physics and Mathematics double major.

She joined the lab of Professor Andy Kortyna in 2008 at the end of her sophomore year and worked on a project studying the associative ionization of cesium, learning skills in optics, programming, and electronics. This work lead to her first publication and was the subject of her senior thesis.

The next summer, in 2009, Jen had the amazing opportunity to work as an REU student at CERN in Geneva, Switzerland. There, she worked with Dr. Slawomir Tkaczyk on the Compact Muon Solenoid (CMS) experiment for the

Large Hadron Collider (LHC). Jen was originally supposed to help with data analysis while the LHC was in operation, but due to an unfortunate superconducting magnet quench, the collider was down until November 2009. Instead, she was tasked with developing software to search for faulty pixels in the tracker, which is the innermost part of the CMS detector designed to track the position of charged particles after a collision. Jen was thus able to develop her programming skills even further, while also attending talks by world renowned physicists and exploring Europe.

Upon her return to Lafayette, Jen continued to work in Andy's lab and graduated with honors in 2010. She was overjoyed to be accepted into Cornell's graduate program in Physics, planning to join one of the research groups that work on the LHC. However, when she took the 510 lab course in her first semester, she was reminded how much she loved the hands on aspect of experimental physics. While high energy physics is quite the interesting topic, it involves a vast amount of time sitting at a desk programming rather than designing and building experiments. The Cornell Nanofabrication Facility (CNF) also piqued her interest, and so she decided to try research in condensed matter physics for a summer. Well, it goes without saying that she never looked back! She joined the Ralph group in 2011, studying spin transport in topological insulators with Alex Mellnik. This led to her second publication as fourth author in Nature. After reaching a dead end with the topological insulator research, Jen became interested in skyrmions, which became the focus of her research and thesis.

After completing her Ph.D., Jen would like to find an industry job that makes use of her expertise in both nanofabrication and magnetics.

This thesis is dedicated to my parents, Kim and Tom Grab, who lovingly encouraged me from an early age to pursue my curiosity of the world.

ACKNOWLEDGEMENTS

First, I would like to thank my adviser, Dan Ralph, for providing valuable expertise, resources, and guidance, while also allowing me the freedom to pursue my own project ideas. Dan's ideas were what originally got me interested in skyrmions, and for that, I am grateful. It is safe to say that without Dan, it would have been very difficult to get this research to work.

I would also like to thank the members of my committee, Eun-Ah Kim and Jeevak Parpia, for reviewing this thesis.

A huge thank you to my undergraduate researcher and friend, Alison Rugar, for pursuing side projects I didn't have the time for, for her assistance with fabrication and measurements, and for her work in building a widefield MOKE setup in our lab. I wish her the best of luck at Stanford and beyond.

Thank you to Alex Mellink for his mentorship when I first joined the Ralph group. Alex helped me learn nanofabrication and basic techniques and later proved to be an excellent collaborator in our work with topological insulators.

Thank you to David MacNeill for help with simulations and theory, and also for moral support and friendship.

Thank you to Marcos Guimaraes for advice on measurement and for collaboration on several projects that sadly didn't work out.

I would like to thank all of the other members of the Ralph group, past and present, for valuable discussion and insight, and friendship, too. Jonathan Gibbons, Neal Reynolds, Greg Stiehl, Colin Jermain, Sriharsha Aradhya, John Heron, Peter Mintun, Colin Heikes, Ted Gudmunsen, Chen Wang, Lin Xue, Eugenia Tam, Wan Li, Yongtao Cui, Sufei Shi, Ruofan Li, and Vishakha Gupta.

And thank you to members of the Buhrman group for letting me use your equipment and for providing initial advice on fabrication - Chi-Feng Pai, Junbo

Park, Praveen Gowtham, Graham Rowlands, Min-Hai Nguyen, and Yongxi Ou.

Thank you to all of the people who helped with imaging. Kayla Nguyen and David Muller for their expertise with TEM. Matt Ferguson and Katja Nowack for their work with scanning SQUID. And the researchers at IBM Almadan for assisting Alison with MOKE.

Thank you to the Cornell Nanoscale Science and Technology Facility (CNF) staff. Alan Bleier, for teaching me the complexities of electron beam lithography. Garry Bordonaro, for his patience in fixing the 5X stepper every single time it broke for no apparent reason. Rob Ilic for help with imaging, sputtering, and electron beam lithography. And everyone else, for answering my questions and keeping the facility up and running.

Thank you to the Cornell Center for Materials Research (CCMR) staff, particularly Steve Kriske for training me on the various measurement tools and Nate Ellis for machine shop training.

Thank you to Andy Kortyna and the other members of the Lafayette College physics department, for your mentorship, for introducing me to physics, and for encouraging me to continue on into graduate school.

And last, but not least, thank you to all my friends and family for your support. My parents, Kim and Tom Grab. My sister, Lisa. My friends, Veronica Pillar, Bob de Alba, Nathan Mirman, Kathryn McGill, Azar Eyvazov, Alex Grant, Jordan Moxon, Heather Williams, Anthony Siska, Luna and Flash, and many others. While a lot of you may not fully understand the intricacies of my research, you encouraged me to never give up, even when my experiments were failing. Your confidence in me was inspiring, and for that I am forever grateful.

TABLE OF CONTENTS

LIST OF FIGURES

CHAPTER 1

INTRODUCTION

Because of their capacity to support skyrmions, topologically stable magnetic vortices, chiral magnets have been of increasing interest in recent years. The desire for smaller, denser, and more stable information storage has been a significant motivating factor, as skyrmions are expected to be more thermally stable than nontopological domains and can be as small as several nanometers in diameter. Because they are easy to move around via spin orbit torque, skyrmions have been proposed as suitable candidates for racetrack memory [1].

In this chapter, I start out with an introduction to chiral magnets and then follow with an overview of skyrmion research as it stands today. A basic understanding of spin valves is also necessary, so I conclude with a discussion of spin transfer torque and giant magnetoresistance.

1.1 Magnetic Ordering in Chiral Magnets

In most ferromagnetic materials, the magnetic order is determined by the Heisenberg exchange interaction and the dipole interaction. The exchange interaction is typically written as,

$$H_{ex} = -J(\mathbf{S_1} \cdot \mathbf{S_2}) \tag{1.1}$$

for neighboring spins $\mathbf{S_1}$ and $\mathbf{S_2}$, where J is the exchange constant. In ferromagnetic materials, J is positive, and thus short-range parallel alignment of electron spins is energetically favorable. The magnetic dipole interaction, on the other

hand, can favor long range parallel or antiparallel alignment. This interaction can be written as,

$$H \propto -\frac{1}{|\mathbf{r}|^3}(3(\mathbf{S_1}\cdot\hat{\mathbf{r}})(\mathbf{S_2}\cdot\hat{\mathbf{r}}) - \mathbf{S_1}\cdot\mathbf{S_2}) \tag{1.2}$$

where $\mathbf{r}$ is the vector connecting the two spins $\mathbf{S_1}$ and $\mathbf{S_2}$. Compared to the exchange interaction, the dipole interaction is very weak, roughly 1000 times smaller for nearest neighbor spins. However, the exchange interaction dies off exponentially with distance, leaving the weaker dipole interaction to dominate on longer length scales. This is the primary reason why magnetic domains are energetically favorable in macroscopic ferromagnetic materials.

1.1.1 The Dzyaloshinskii-Moriya Interaction

In certain materials, another type of ordering can occur, in addition to the two already described. In 1960, Igor Dzyaloshinskii developed a theory for weak ferromagnetism in which he introduced an asymmetric exchange term in the Hamiltonian [2]. Shortly after, Toru Moriya found that this term partially results from strong spin-orbit coupling, in addition to broken inversion symmetry [3]. Thus the interaction is now called the Dzyaloshinskii-Moriya Interaction (DMI).

The antisymmetric exchange interaction, or Dzyaloshinskii-Moriya Interaction (DMI) [2][3], can be written as,

$$H = -\mathbf{D}\cdot(\mathbf{S_1}\times\mathbf{S_2}) \tag{1.3}$$

where $\mathbf{D}$ is a constant vector. This interaction favors orthogonal alignment of neighbor spins, with a chirality determined by the direction of the DMI vector $\mathbf{D}$. Ferromagnetic materials with strong DMI, often called chiral or helical magnets, tend to support domain structures with a fixed chirality, such as stripes

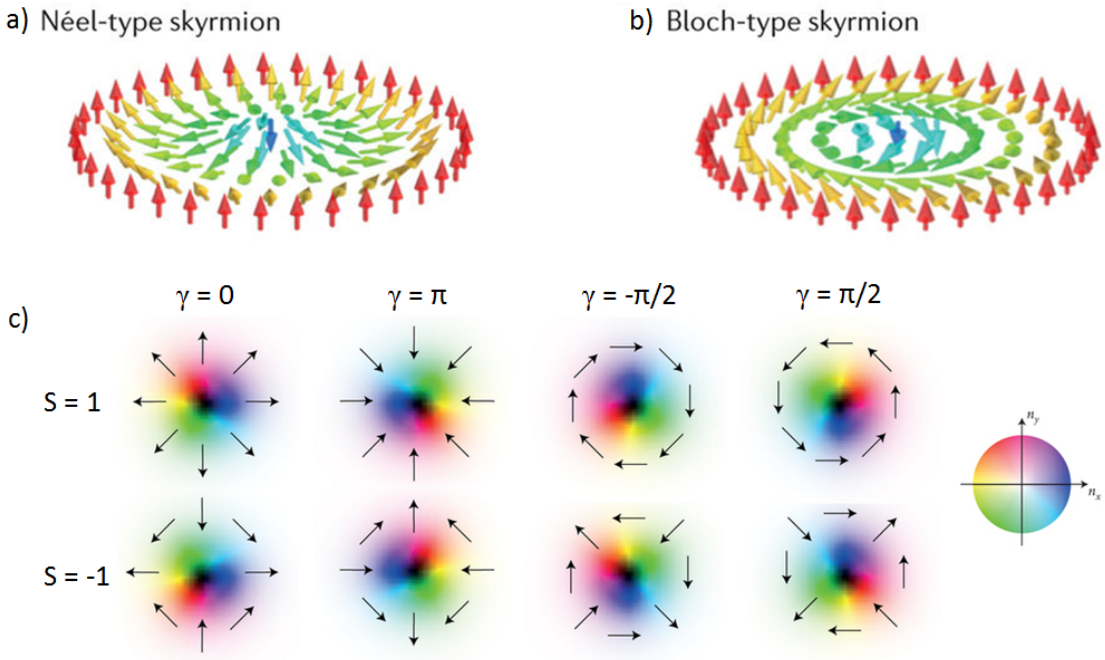

Figure 1.1: Examples of **(a)** Néel-type and **(b)** Bloch-type skyrmions with a winding number of 1. **(c)** Skyrmions (S=1) and antiskyrmions (S=-1) with varying helicities, γ. The arrows depict the in plane spin component. Figures from [4] (a,b) and [5] (c).

or skyrmions. Such domains result from the competition between DMI and either the dipole or exchange interaction that favor alignment or antialignment of spins. DMI can occur in bulk crystalline materials or at an interface, resulting in slightly different behavior.

1.2 Skyrmions

Skyrmions are topologically protected quasiparticles in the form of stable vortices found in certain magnetic materials. They are typically very small, on the order of tens or hundreds of nanometers, and robust due to their topological na-

ture. Skyrmions can be defined as having a nonzero integer value for the topological winding number, or skyrmion number, which in the two dimensional limit can be written as,

$$S = \frac{1}{4\pi} \int \mathbf{m} \cdot (\partial_x \mathbf{m} \times \partial_y \mathbf{m}) \mathrm{d}x\mathrm{d}y \tag{1.4}$$

where **m** is the normalized local magnetization [4]. This winding number is essentially a measure of how many times the spins wrap around a unit sphere and most commonly is 1 for a skyrmion and -1 for an antiskyrmion. A typical skyrmion consists of a core that is antiparallel to the surrounding film. Skyrmions are classified by their skyrmion number and their helicity, γ, which determines the behavior of the spins immediately surrounding the central core (Figure 1.1c). Bloch skyrmions have a helicity of $\gamma = \pm\pi/2$, and the spins wrap clockwise or counterclockwise in-plane around the central core (Figure 1.1b). Néel, or "hedgehog," skyrmions have a helicity of $\gamma = 0$ or π, and the surrounding spins pointing toward or away from the core (Figure 1.1a). The type of skyrmion encountered in a given material system depends on the specifics of the interactions involved. Bloch-type skyrmions are usually found in materials with bulk DMI, and Néel-type skyrmions are typically found in systems with interfacial DMI.

1.2.1 Skyrmions without DMI

Although contemporary research focuses on materials with strong DMI, the Dzyaloshinskii Moriya Interaction isn't necessary for the formation of skyrmions. In fact, some of the earliest work involving skyrmions in the 70s and 80s studied the appearance of chiral domain structures, or "magnetic bubbles," in materials with a competition between the long range dipole interaction

and perpendicular anisotropy [6]. The development of magnetic bubble memory was a topic of intense research at this time, although for various reasons, the technology was dropped in favor of higher density storage options. Examples of materials showing these properties include thin films of uniaxial garnet [7] and amorphous rare earth / transition metal alloys [8]. The dipole interaction favors an in plane magnetization, while the anisotropy favors the out of plane direction. At zero field, these materials have a periodic spin helix state, but when a field is applied perpendicular to the sample, the stripes pinch off into a periodic array of magnetic bubbles, or skyrmions. These skyrmions are quite large, typically on the micron scale, and tend to be Bloch-type, although Néel-type skyrmions and topologically trivial bubbles are also possible.

Another situation in which skyrmions can occur without DMI is in systems with frustrated [9] or four-spin exchange interactions [10]. These skyrmions are very small, on the order of the lattice constant for the material ($\sim$ 1 nm). In the complete absence of DMI, skyrmions and antiskyrmions are degenerate, and there also isn't a preferred helicity. DMI, while not necessary for the appearance of topological features, breaks the symmetry and favors skyrmions, rather than antiskyrmions, with a specific helicity. Because atomic scale precision is required for studying these systems, most of the work done to date has been simulation-based. However, in 2011, a square lattice of skyrmions was observed in a hexagonal Fe film of one-atomic-layer thickness on Ir(111) using STM at cryogenic temperatures (11 K) [10].

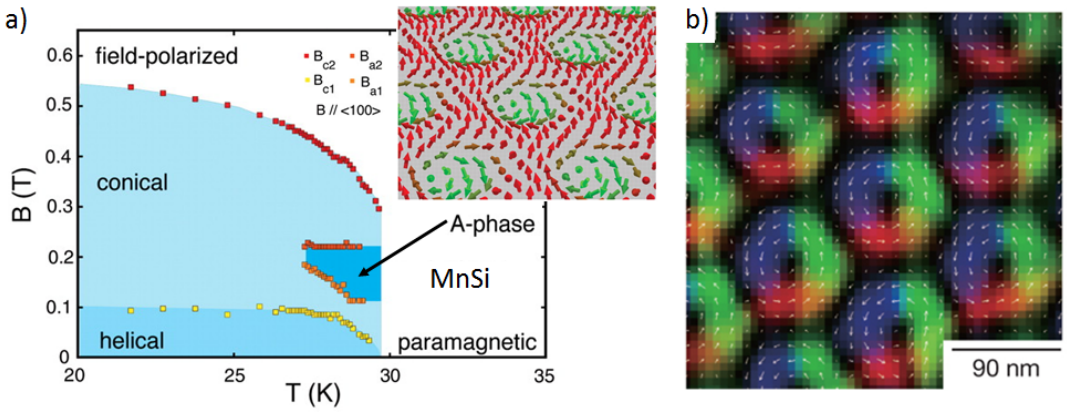

Figure 1.2: **(a)** Phase diagram for MnSi as a function of temperature and applied field. B_{s1}, B_{s2}, B_{a1}, and B_{a2} are the critical values of the field at the phase boundaries. The inset shows the calculated spin configuration for the skyrmion lattice A phase. Figure from Reference [11]. **(b)** Lorentz TEM imaged of the skyrmion lattice phase in FeGe. Figure from [12]

1.2.2 Bulk DMI - Noncentrosymmetric Magnets

Bulk DMI can occur in certain crystalline materials, frequently called noncentrosymmetric magnets because the unit cell does not have inversion symmetry. This broken inversion symmetry leads to spin-orbit coupling and DMI. At low temperatures, noncentrosymmetric magnets support a helical stripe phase for low fields and a skyrmion crystal phase for an intermediate field range. The skyrmion crystal phase, or A-phase, was first observed in MnSi in 2009 using neutron scattering [11], and was found to be a triangular array of Bloch skyrmions with a diameter of roughly 18 nm (Figure 1.2a) [13]. Similar states have been observed in other materials such as FeGe (Figure 1.2b) [14][12], $Fe_{1-x}Co_xSi$ [15], $Mn_{1-x}Fe_xGe$ [16], and even in insulating multiferroic materials like Cu_2OSeO_3 [17]. Triangular lattices of Néel skyrmions are also possible in

certain materials with uniaxial anisotropy and rhombohedral symmetry, such as GaV_4S_8 [18].

Research in this field is ongoing, with new and different materials being studied each year. However, despite their interesting properties, noncentrosymmetric magnets are not ideal for magnetic memory applications. A room temperature skyrmion lattice has not yet been discovered, with the highest temperature occurrence being FeGe at 278 K [14]. It is difficult, if not impossible, to isolate and manipulate individual skyrmions in the lattice. Lastly, these lattices exist in a relatively narrow (nonzero) field and temperature window. For these reasons, systems with interfacial DMI are now being studied as a possibility for high density storage and race track memory. Such materials are the primary focus of this work.

1.2.3 Interfacial DMI

Skyrmions and chiral spin textures have been observed in multilayers with interfacial DMI, the most common example of which is the interface between a heavy (5*d*) metal (HM) with strong spin-orbit coupling and a ferromagnet (FM) with perpendicular magnetic anisotropy (PMA). The inherent inversion symmetry breaking of the interface, combined with spin orbit coupling from the heavy metal, leads to DMI.

Although not fully understood at the time, the first observation of chiral spin textures induced by interfacial DMI was in 2002, when Kubetzka, *et al.* imaged stripe domains in two monolayers of Fe on W(110) using spin polarized STM [20]. Several years later, first principle calculations established that

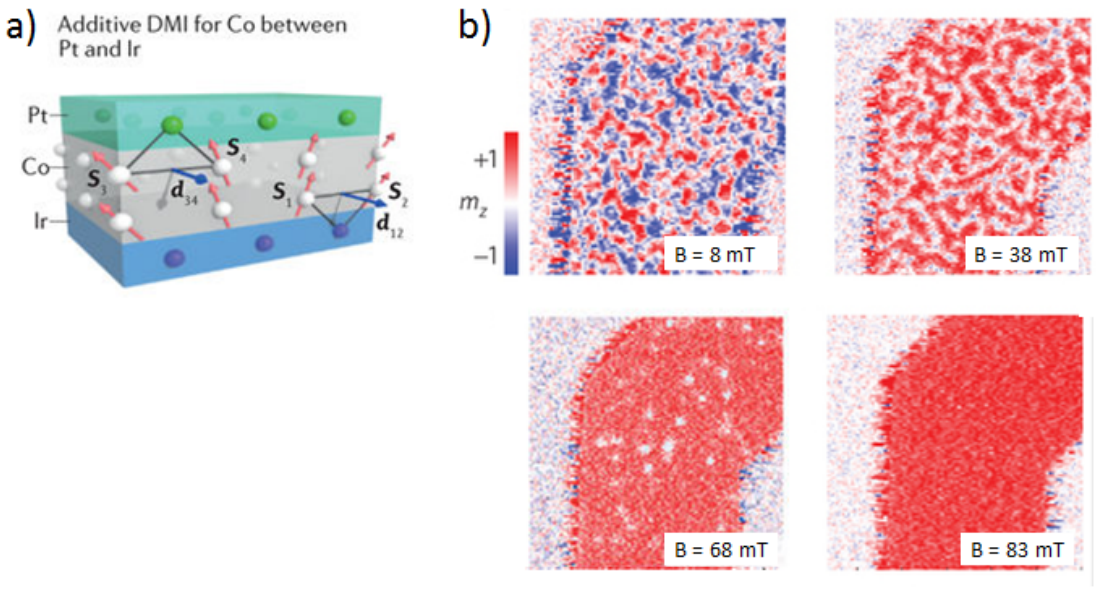

Figure 1.3: **(a)** Schematic showing DMI enhancement in Ir/Co/Pt trilayers. The Ir/Co and Pt/Co interfaces have DMI with opposite sign [19]. **(b)** $1.5 \times 1.5\mu m^2$ STXM image of the out-of-plane magnetization of a $[Ir/Co/Pt]_{10}$ multilayer at various out-of-plane applied fields [19].

these domains are a result of DMI at the interface [21]. Since then, chiral domain structures have been observed in a variety of HM/FM interfaces, many at room temperature. Interfacial DMI has also been observed in interfaces between ferromagnets and oxides, such as MgO or TaO_x [22], or even interfaces with graphene [23]. Many of these films can be deposited using magnetron sputtering, which is relatively easy and accessible for spintronics applications.

To further enhance the DMI and stabilize skyrmions, multilayers with many repetitions of HM/FM/HM are frequently used. This increases the magnetic volume and makes skyrmions more robust against thermal instabilities [4]. If the ferromagnetic layer is sandwiched between two layers of the same metal, for example Co/Pt multilayers, contributions from opposing interfaces will cancel,

greatly reducing the effective DMI, which is not ideal. However, if the ferromagnetic layer is sandwiched between two heavy metals with opposing signs for the DMI, for example Pt/Co/Ir [19], then the effective DMI will be much higher (Figure 1.3a) [24] [22]. For similar reasons, HM/FM/oxide trilayers, for example Pt/Co/MgO [25] or Pt/CoFeB/TaO_x [26], are also of interest.

Room temperature magnetic skyrmions have been observed in a variety of multilayers of this type, typically at nonzero fields slightly below saturation. Skyrmions are generally Néel-type and can be anywhere from 30 nm to 1 μm in size, depending on the materials used. Only two multilayers have been found to have sub-100 nm skyrmions - Pt(10)/Co(0.6)/Pt(1)$[$Ir(1)/Co(0.6)/Pt(1)$]_{10}$/Pt(3) (30 nm) (Figure 1.3b) [19] and $[$Ir(10)/Fe(x)/Co(y)/Pt(10)$]_{20}$ (40 nm) [27]. However, for magnetic memory applications, a skyrmion size of less than 10 nm is required. Related to this is the question of whether micron sized skyrmions in these materials are actually compact skyrmions or if they're chiral or skyrmionic bubbles, that is a domain with a reversed magnetization, surrounded by a Néel wall, that has a topological number of approximately 1 [4]. Compact skyrmions and skyrmionic bubbles are similar in that they are both topologically nontrivial, stable, and have similar current-induced motion, but compact skyrmions have a diameter close to the domain wall width, as calculated from the DMI and other material parameters. It has been shown that in materials with strong DMI, there can be multiple energy minima corresponding to not only compact skyrmions, but also skyrmionic bubbles with larger diameter. For application purposes, it would be beneficial to find a way to favor smaller compact skyrmions over bubbles.

Another issue is that in materials with interfacial DMI, a nonzero field is re-

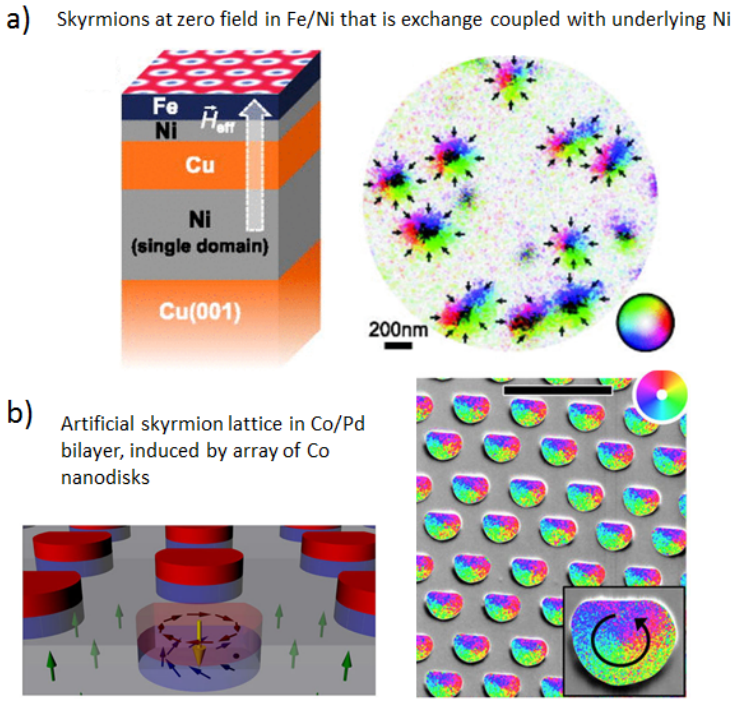

Figure 1.4: **(a)** Skyrmions stabilized at zero field in a Fe/Ni bilayer using interlayer exchange coupling with an underlying Ni layer. Image on the right is obtained using spin polarized low-energy electron microscopy (SPLEEM) [28]. **(b)** Artificial skyrmion lattice created in Co/Pd bilayer at zero field using patterned Co nanodisks. Image on the right is obtained using scanning electron microscopy with polarization analysis (SEMPA). The scale bar is 2 μm [29].

quired to stabilize skyrmions. So far two ways have been found to get around this, both of them using an additional magnetic layer. In [28], a bulk PMA ferromagnetic layer with a nonmagnetic spacer was deposited under an Fe/Ni bilayer. The interlayer exchange coupling was tuned by varying the spacer thickness to favor skyrmions at zero applied field (Figure 1.4a). Another group was able to produce an artificial skyrmion lattice at zero field by patterning an array of cobalt nanodisks on top of a Co/Pd bilayer [29]. The local field from the disks, combined with irradiation of the underlying film to make it magnetically softer, induced skyrmions in the Co/Pd bilayer (Figure 1.4b). Interlayer

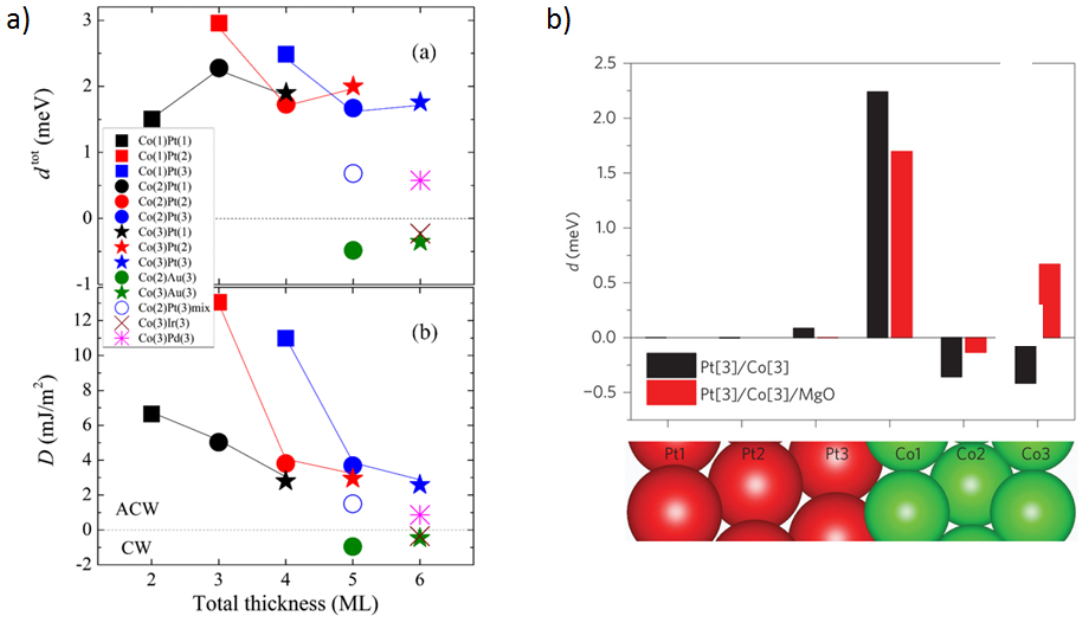

Figure 1.5: **(a)** Calculated total DMI coefficient d^{tot} and micromagnetic DMI D for a variety of Co/HM bilayers. Colors/lines correspond to fixed Pt thickness [31]. **(b)** Calculated layer-resolved microscopic DMI for Pt[3ML]/Co[3ML] and Pt[3ML]/Co[3 ML]/MgO [25].

exchange coupling has also been predicted theoretically to have a similar effect in other materials as well [30]. We are likely to see more work in this area in the coming years.

1.2.4 DMI in Co/Pt bilayers

In this thesis, we focus on skyrmion creation in Co/Pt bilayers, which have not been studied in as much detail experimentally as multilayers with many repetitions or trilayers. First principle calculations demonstrate that the interfacial DMI should be large enough to support chiral domains and skyrmions. The

DMI is expected to decrease with increasing cobalt thickness, but it is relatively unaffected by platinum thickness (Figure 1.5a) [31]. Skyrmions have also been observed in sputtered Ta(3)/Pt(3)/Co(0.51)/MgOx/Ta(1) films using photoemission electron microscopy combined with X-ray magnetic circular dichroism (XMCD-PEEM). *Ab initio* calculations for these films have shown that the Co/Pt interface has a large DMI, even in the absence of MgO (Figure 1.5b) [25] [22].

1.3 Experimental Techniques for Creating Isolated Skyrmions

For technological applications, being able to controllably create, manipulate, and delete magnetic skyrmions is critical. A few different techniques have been studied to create skyrmions, although each has setbacks, and many more have been proposed. Manipulation of skyrmions in systems with interfacial DMI can be done using spin orbit torque from the heavy metal layer. Deleting skyrmions is tricky, and less work has been done in this area so far.

1.3.1 Writing and Deleting Skyrmions using an STM tip

The first instance of skyrmions being controllably created and destroyed experimentally was in 2013 by Romming, *et al.*, using a spin polarized scanning tunneling microscope (SP-STM) tip on PdFe on Ir(111) [32]. SP-STM is a specialized form of STM that used a magnetic tip to obtain magnetic contrast at ultra high resolution. At low temperatures (8 K), PdFe on Ir(111) shows stripe domains at zero field, and then at intermediate fields below saturation, both skyrmions and stripes can exist. When the STM tip is held in a stationary position and a

large current is applied, a skyrmion is created (Figure 1.6). In a similar way, skyrmions can be deleted. The mechanism behind this behavior was shown to be a combination of both spin transfer torque and nonthermal excitations caused by the energy of the injected electrons. The reason spin transfer torque comes into play makes sense if the tip/vacuum/sample system is thought of as a magnetic tunnel junction. The current becomes spin polarized by the tip and thus either parallel or antiparallel alignment will be favored, depending on the sign of the current. This is a very similar concept to the work done in this thesis, except I use a nanopillar to inject a spin polarized current rather than an STM tip.

A similar effect was observed using a nonmagnetic STM tip on epitaxial Fe on Ir(111) [33]. That is, skyrmions were able to be controllably written and deleted using the local electric field generated by a tungsten tip. The sign of the electric field determines whether creation or annihilation is favored, which rules out thermal effects. Instead, they propose that local distortion of the lattice slightly alters the magnetic properties of the film. In any case, this work provides further evidence that spin transfer torque isn't the only mechanism behind skyrmion manipulation using an STM tip.

1.3.2 Creating Skyrmions Using a Geometric Constriction

A second method that has been explored experimentally is to use a geometrical constriction to create skymion bubbles. The first group to study this effect was Jiang, *et al.* in 2015 in a Ta/CoFeB/TaO_x trilayer [26]. As mentioned earlier, when a current is applied through a HM/FM/oxide trilayer, the spin Hall effect

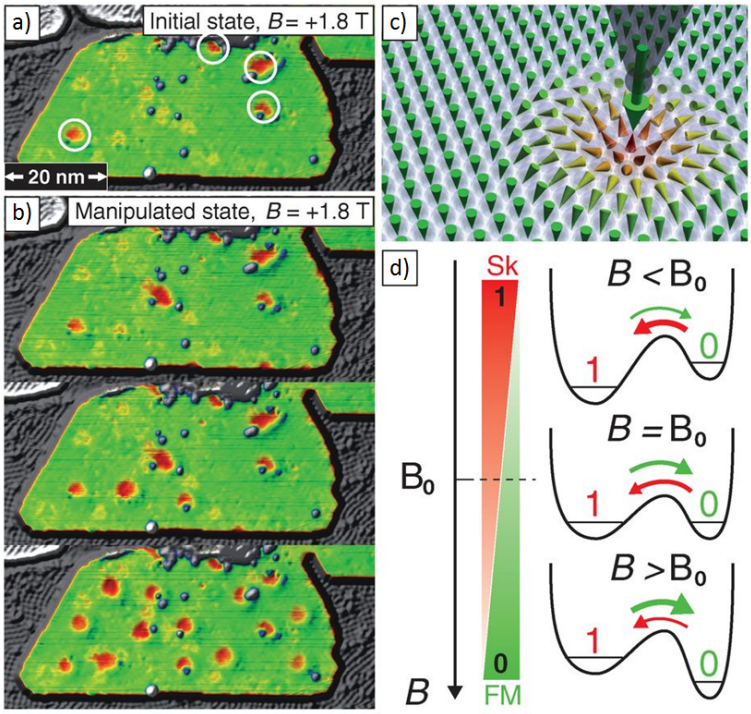

Figure 1.6: Writing and deleting skyrmions using an SP-STM tip. **(a)** SP-STM image showing the initial state before manipulation. **(b)** Successive creation of skyrmions by injecting a large spin polarized current using the STM tip. **(c)** Schematic of skyrmion creation. **(d)** Diagram of field dependent potential for skyrmions (S_k) and the ferromagnetic state. At B_0 the states are degenerate. [32]

in the heavy metal layer results in a transverse spin current into the ferromagnetic layer, which then causes a spin orbit torque on domains in the ferromagnet. Depending on the sign of the spin Hall angle, chiral Néel walls will move either in the positive or negative current direction. Domain walls parallel to the current remain stationary. In this way, stripe domains and skyrmions can be easily moved with an in-plane current.

Now, if the film is patterned into a constriction in one area, inhomogeneous current flow will result at the ends of the constriction. If the current was originally only flowing in the x direction, there will now also be a component in the

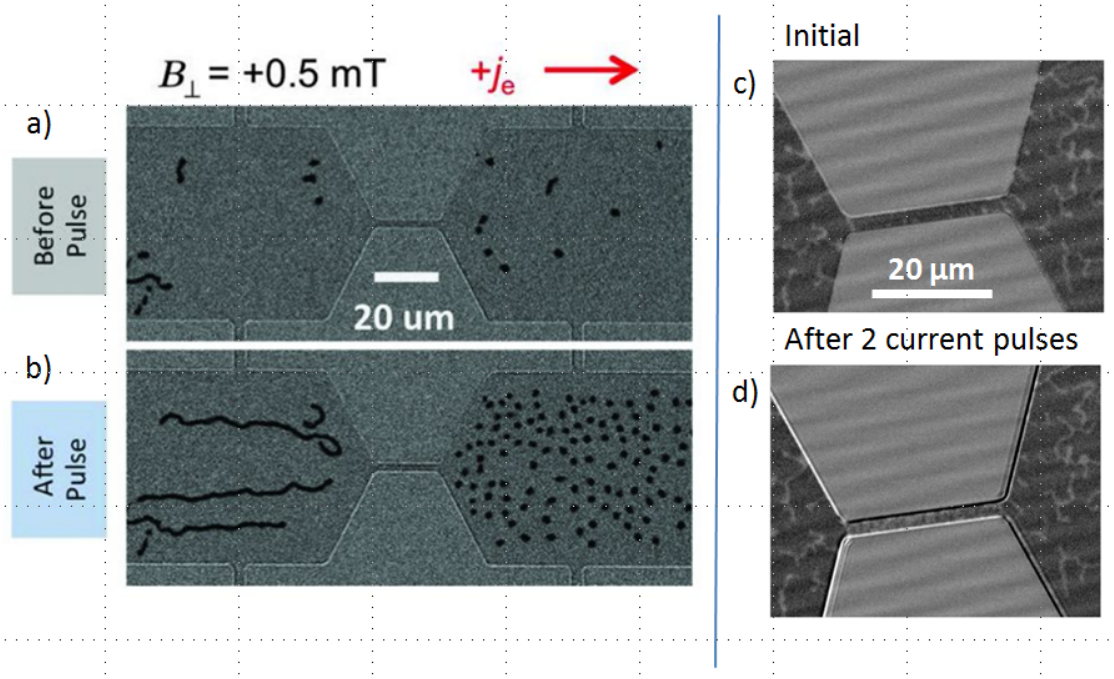

Figure 1.7: Widefield MOKE images showing skyrmion creation using a geometric constriction. **(a)** and **(b)** MOKE images of Ta/CoFeB/TaO_x film before and after applying a current pulse of $J_e = +5 \times 10^5$ A/cm^2 [26]. **(c)** and **(d)** MOKE images of our Co/Pt bilayers before and after applying two 15 ns current pulses of $J_e = 3.5 \times 10^7$ A/cm^2 (image by Alison Rugar).

y direction near the constriction. When a domain exits the constriction, the spin orbit torque will expand the end of the domain in both the x and y directions, increasing it's radius until at some point, the growing "surface tension" from the exchange and anisotropy fields will cause it to pinch off into a skyrmion bubble (Figure 1.7a-b).

We attempted to replicate this experiment in our Co/Pt films.[1] However, we ran into several problems. First, because the domains are much smaller in Co/Pt films, imaging was a challenge (see section 2.2 for details). Second, when

[1]Project lead by my undergraduate researcher, Alison Rugar. See her honors thesis for more information [53].

we did manage to image our samples, instead of skyrmion nucleation at the end of the constriction, we observed domains nucleating inside the constriction, but not moving with the current (Figure 1.7c-d). We used current densities much larger than Jiang, *et al.* [26], so we believe that too much current might have been shunting through the tantalum underlayer as well as the Cu/Pt cap. It is also possible that the 3 μm constriction might have been too wide, considering the stripe domains are around 200 nm wide. Making a smaller constriction would likely require electron beam lithography. Because of time constraints, this project was abandoned in favor of building a widefield MOKE setup at Cornell, since having such a setup available would have helped diagnose the above problem quicker. However, with the correct geometries we do believe it should be possible to create skyrmions in Co/Pt bilayers using a constriction.

Compared to STM, creating skyrmions with a constriction is much more practical for applications, since it can be done in ambient conditions. Also, expensive, specialized equipment isn't necessary. However, the skyrmions created are quite large, and are believed to be skyrmion bubbles rather than compact skyrmions. Although single skyrmion creation and motion has been demonstrated using a geometrical constriction [34] [35], it is not controllable to the extent that a skyrmion can be created in an exact location. Lastly, the devices are quite large. A more compact geometry would be better suited for applications. Creating skyrmions with a spin valve nanopillar, which is the topic of this thesis, is advantageous because it is both small in size and location specific. While the fabrication is more challenging, pillars can be made very small, with the potential to create compact skyrmions, and, as discussed in the next section, the pillar serves a secondary function of reading out skyrmions. It also may be possible to delete skyrmions with this configuration.

1.4 Spin Valves

In this work, we attempt to create and detect skyrmions using a spin valve, which is a structure consisting of two magnetic layers, a fixed and a free layer, separated by a thin nonmagnetic spacer layer. Spin transfer torque is the main mechanism by which we hope to create chiral domains in the free layer, and giant magnetoresistance is what is measured to monitor the state of the free layer. In this section, I will discuss the qualitative basics of both of these concepts.

Usually a charge current is made up of electrons with spins oriented in random directions. However, when a current passes through a ferromagnetic material, electrons with spins oriented parallel[2] to the magnetization will have a higher transmission amplitude than spins of opposite sign, and the current will become spin polarized. That is, the average spin moment of the electrons will be oriented in a particular direction. Then, if the spin polarized current enters another ferromagnet, some of the spin angular momentum will be transferred to the magnet, and if the current and polarization are large enough, the moment of the magnet can start to rotate toward the toward the direction of spin polarization. This effect is called spin transfer torque [36] [37].

As already stated, a spin valve consists of two magnetic layers, a fixed layer and a free layer (Figure 1.8). The purpose of the fixed layer is to polarize the current, so it must have a relatively large magnetic volume and a high coercive field, such that it's magnetization stays effectively fixed. The free layer is much softer and switches depending on the direction of the current. Let's first assume that the fixed layer is oriented to the right, as in Figure 1.8, and the free layer is

[2]We assume all ferromagnets are positive polarizers in this discussion, i.e. they transmit majority-spin electrons.

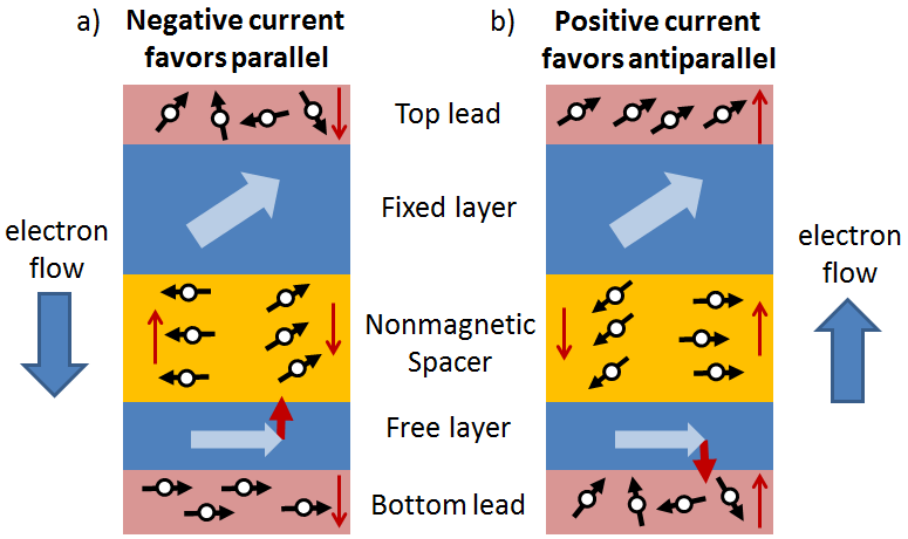

Figure 1.8: Spin transfer torque in a spin valve. **(a)** When the current is negative, polarized electrons from the fixed layer cause the free layer to rotate in the direction of the fixed layer (parallel alignment). **(b)** When the current is positive, electrons reflected from the fixed layer will cause the free layer to rotate away from the fixed layer (antiparallel alignment).

oriented at a slight angle to that. If a negative current is applied, electrons will flow from the fixed layer to the free layer. The current will be polarized in the direction of the fixed layer and, as a result, apply a spin transfer torque such that the free layer moment will turn in the direction of the fixed layer moment. Thus parallel alignment will be favored (Figure 1.8a). If a positive current is applied, electrons will flow from the free layer to the fixed layer. Initially they will be polarized in the direction of the free layer and cause a torque on the fixed layer, although we are assuming this effect is negligible. More importantly, electrons with spin oriented antiparallel to the fixed layer will be reflected from the interface, since parallel electrons are transmitted. This reflected spin current then causes the free layer moment to rotate away from the fixed layer, destabilizing parallel alignment, and, if the current is large enough, favor antiparallel align-

ment of the two layers (Figure 1.8b) [38] [39].

A particularly useful aspect of spin valves, however, is that because the alignment of the two layers can be controlled with a current, so can the resistance. When magnetic layers separated by a metallic spacer are oriented parallel to each other, the resistance is relatively low, and when they are oriented antiparallel, the resistance is much higher. The resistance change between parallel and antiparallel states can be as high as a few tens of percent [38] for spin valves, and as high as several hundreds percent for tunnel junctions. In spin values, this is due to an effect called Giant Magnetoresistance (GMR), "giant" referring to the fact that it's usually much larger than anisotropic magnetoresistance [40] [41] [42]. An easy way to understand GMR is to think about spin polarizations, similar to our discussion of spin transfer torques. Current passing through the first magnetic layer will become polarized in that direction. Then, when the polarized electrons encounter the second magnetic layer, the transmission amplitude will depend on the second layer's orientation. If the second layer is parallel to the first, most of the electrons will be transmitted, resulting in a lower resistance. If the second layer is antiparallel, many of the electrons will be scattered, and the resistance is higher. If the second layer is somewhere in between parallel and antiparallel, the stack will have an intermediate resistance.

We study spin valve like devices as a possible technique to create static or dynamic skyrmions. The fixed layer is a perpendicularly oriented multilayer patterned into a pillar, and the free layer is an extended Co/Pt bilayer film. A local spin transfer torque in the portion of the free layer immediately under the pillar can be used to affect the magnetization in that region. The pillar resistance

is measured to monitor the state of the free layer in the vicinity of the pillar. In the next two sections, we will cover the design and fabrication of these devices.

CHAPTER 2

MATERIALS - GROWTH AND CHARACTERIZATION

The cobalt platinum interface has a very large DMI [31], which makes these films a good choice for studying topological dynamics as well as stable skyrmions. Here, I summarize the various factors that must be considered when growing these films and then discuss options for imaging the chiral domain structure.

2.1 Sputtering PMA Co/Pt Films

Sputtering has proven to be a convenient and effective technique to grow films with interfacial DMI. Because they are predominately interfacial effects, perpendicular magnetic anisotropy (PMA) and DMI are very sensitive to film quality and smoothness. A low base pressure, less than $\sim 3 \times 10^{-9}$ Torr, is critical, as well as long presputter times, on the order of 10-20 minutes for each material, before growth. Additionally, to attain the lowest deposition rate possible, we use low power, roughly 20 W, and low pressure, roughly 2 mTorr. A minimum 3 nm thick tantalum smoothing layer is also necessary for optimal film quality. Our spin valve devices consist of a bilayer film (free layer) in which we hope to create static or dynamic skyrmions, a 5 nm copper spacer, and last, a harder multilayer film (fixed layer / polarizer), to be patterned into a pillar. Films are grown using DC magnetron sputtering and characterized using a combination of vibrating sample magnetometry (VSM) and magnetic force microscopy (MFM).

2.1.1 Co/Pt Bilayers - Free Layer

The first step toward growing bulk films for our spin valve devices is to develop a recipe for a cobalt/platinum bilayer with perpendicular anisotropy. This will be the film in which we hope to create static or dynamic skyrmions. Additionally Co/Pt bilayers are an interesting topic of study because, while there has been a lot of work done with Co/Pt multilayers in the literature, not much has been done with bilayers. Here, I will outline the various growth parameters and how they affect the PMA and domain structure of the film. All films described here follow the recipe Ta(3)/Pt(x)/Co(y)/Cu(5)/Pt(5), starting from the bottom and with thicknesses in nanometers.

Cobalt Thickness

Changing the cobalt thickness affects the perpendicular anisotropy of the film (Figure 2.1a-c). We observe that as the cobalt thickness is increased, the PMA, or "squareness" of the hysteresis curve, gets weaker, until at a particular transition thickness, the film becomes in-plane. This is because if the cobalt is too thick, the bulk behavior will dominate over interfacial behavior. The value of the transition thickness varies slightly depending on chamber quality, but it is typically around 1.7 nm of cobalt. A second effect that was observed is that for very thin cobalt films, around 0.35 nm or less, the PMA appears to decrease. A possible reason for this is that the cobalt is no longer continuous at such small thicknesses. These trends are in agreement with previous room temperature observations in the literature [43] [44].

We imaged the domain structure of our films using MFM (Figure 2.1d-f).

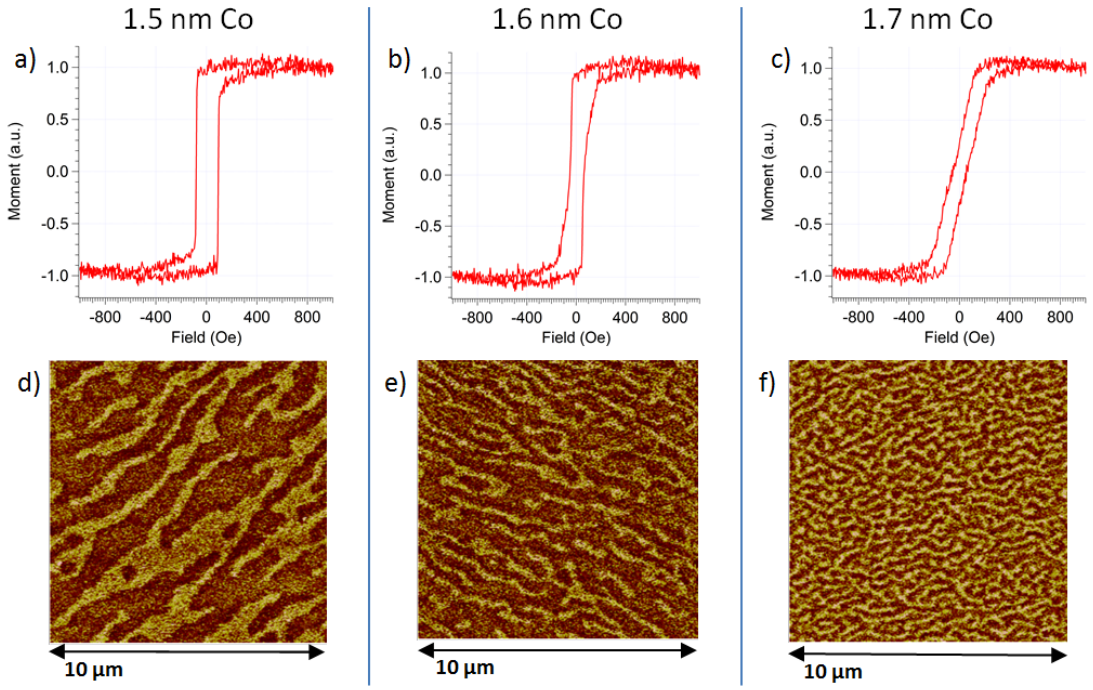

Figure 2.1: **(a-c)** Magnetometry data (VSM) and **(d-f)** MFM images showing the effect of cobalt thickness on perpendicular anisotropy and as-grown domain structure for bilayers, Ta(3 nm)/Pt(5)/Co(x)/Pt(10). The film becomes in plane above the transition thickness of 1.7 nm Co. All except the domain structure in **(f)** are destroyed by saturation. The magnetic field is perpendicular to the film.

Films with a cobalt thickness close to, but smaller than, the transition thickness have much weaker PMA and thus favor the formation of chiral stripe domains. The virgin (as-grown) domain structure is helical for cobalt thicknesses up to 3Å less than the transition thickness. Because the PMA increases relative to the DMI as the film gets thinner, the stripes get larger with decreasing thickness. With the exception of cobalt thicknesses very close to the transition (Figure 2.1f), this domain structure goes away once the film is saturated, and the film becomes monodomain at low fields on the length scales of our experiment.

Platinum Thickness

The platinum thickness also has an effect on the PMA, except in this case, there is a transition thickness below which the PMA is destroyed. The transition is typically around 2 nm of platinum, and at thicknesses significantly above this, the PMA appears to be unaffected (Figure 2.2a). Although this is not a limit we reached with our test samples, we suspect that at very large platinum thicknesses, the PMA might be weakened due to interfacial roughness. Similar to the cobalt transition, as the thickness of platinum decreases, the virgin stripe domains get smaller until the film becomes in plane (Figure 2.2b-d). Again, the virgin domain structure is destroyed by saturation, except when the platinum thickness is very close to the transition.

2.1.2 Co/Pt Multilayers - Fixed Layer

Once we have a working bilayer recipe, the next step is to develop a Co/Pt multilayer recipe to be used as the fixed layer, or polarizer, in our spin valve devices. The multilayer should have a high coercive field relative to the bilayer. It should also have a sharp hysteresis loop (strong PMA). That is, it should be approximately monodomain at low fields on the length scale of a nanopillar (100 nm). It should also have as many repetitions as possible and thick cobalt layers (ideally comparable to the spin diffusion length $\sim$ 34 Å) to maximize current polarization and the resulting spin transfer torque. When testing multilayer recipes, it is best to deposit the entire stack, including the underlying Co/Pt bilayer and copper spacer. The slight increase in roughness from underlying layers can alter characteristics of the multilayer. The results below are in good agreement with

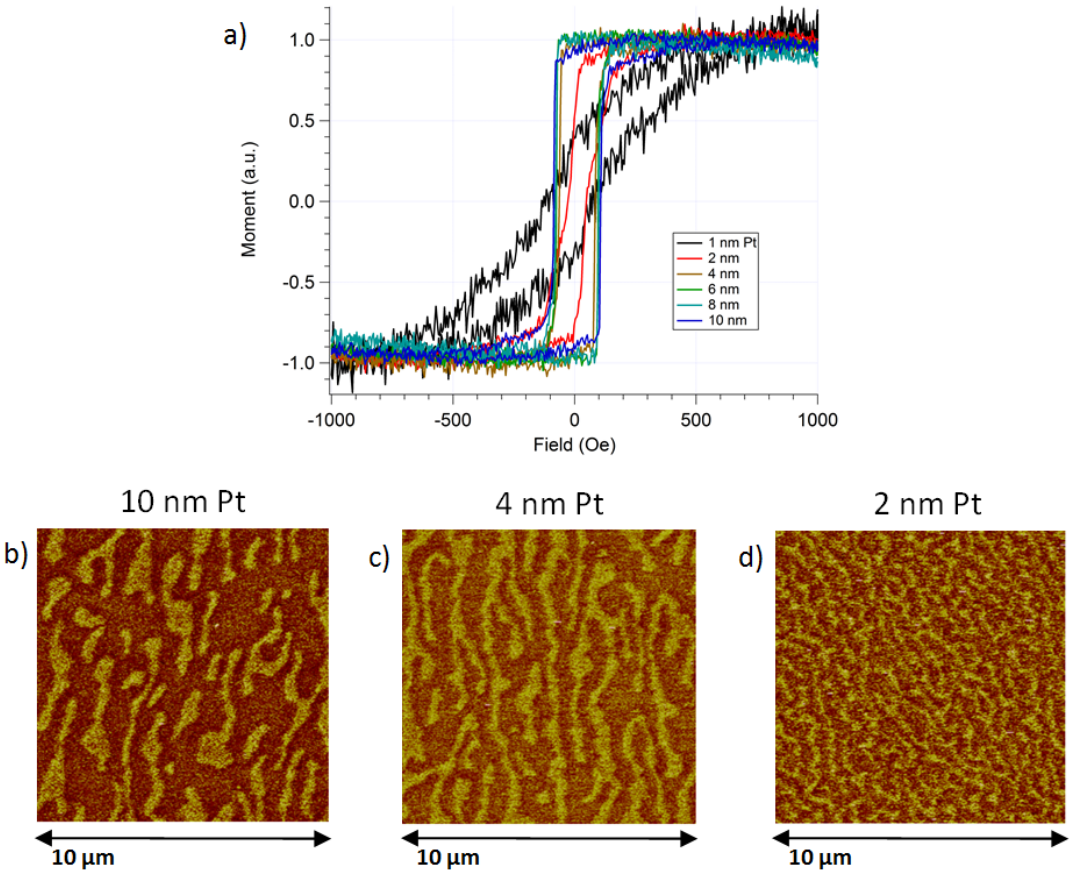

Figure 2.2: **a)** Magnetometry data (VSM) showing the effects of changing the platinum thickness in bilayers, Ta(3 nm)/Pt(x)/Co(1.4)/Pt(10). The magnetic field is perpendicular to the film. **(b-d)** MFM images showing the decrease in as-grown stripe domain size with decreasing Pt thickness. All except the domain structure in **(d)** are destroyed by saturation.

previous studies [45] [46].

Cobalt Thickness

We find that both the coercive field and PMA of the Co/Pt multilayers is strongly dependent on cobalt thickness (Figure 2.3a). If the cobalt is too thin, the multilayer has very weak PMA and the coercive field approaches that of the

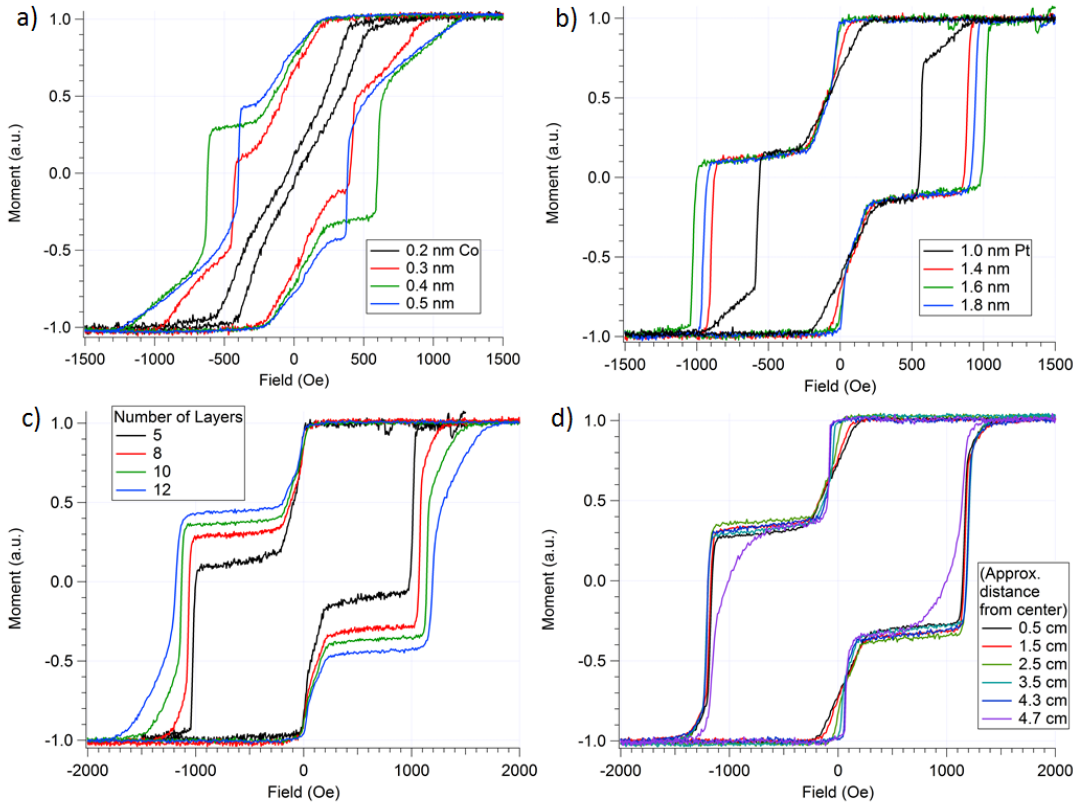

Figure 2.3: Optimizing various parameters for the Co/Pt fixed layer. The low field switching event corresponds to the bilayer. **a)** Varying the cobalt thickness for a fixed platinum thickness (1.0 nm) and fixed number of repetitions (5). **b)** Varying the platinum thickness for a fixed cobalt thickness (0.4 nm) and fixed number of repetitions (5). **c)** Varying the number of repetitions of Pt(1.6)/Co(0.4). **d)** Film variation as a function of distance from the center of the wafer. The applied field is out of plane.

bilayer. If the cobalt is too thick, we see a similar trend. The optimum cobalt thickness is an intermediate value, typically around 0.4 nm, but it varies depending on the chamber quality. This optimum cobalt thickness doesn't seem to change much with the platinum thickness.

Platinum Thickness

The platinum thickness dependence follows a similar pattern as the cobalt thickness dependence. That is, there is an optimum platinum thickness above and below which the coercive field is lower. We believe this happens because changing the thickness of the platinum layers is effectively tuning the coupling of the cobalt layers. If the platinum is too thin, the cobalt layers are too close together and start to pull each other in plane, weakening the PMA. If the platinum is too thick, each cobalt layer starts to act as an independent magnet. We find that the optimum platinum thickness is around 1.6 nm for our Co/Pt multilayers (Figure 2.3b).

Layer Repetitions

When the number of Co/Pt repetitions is increased, we see an increase in the coercive field. However there is a trade off, since the PMA also gets weaker as the number of layer repetitions is increased. The hysteresis curve loses it's "squareness" and becomes more sloped. This is believed to be due to the increased roughness with added layers, since PMA is an interfacial effect. Secondly, as more layers are added, there is an increased risk of human error, since films are deposited manually. We thus chose an intermediate value of 8 repetitions, which gives a reasonably high coercivity, while still keeping the switching relatively sharp.

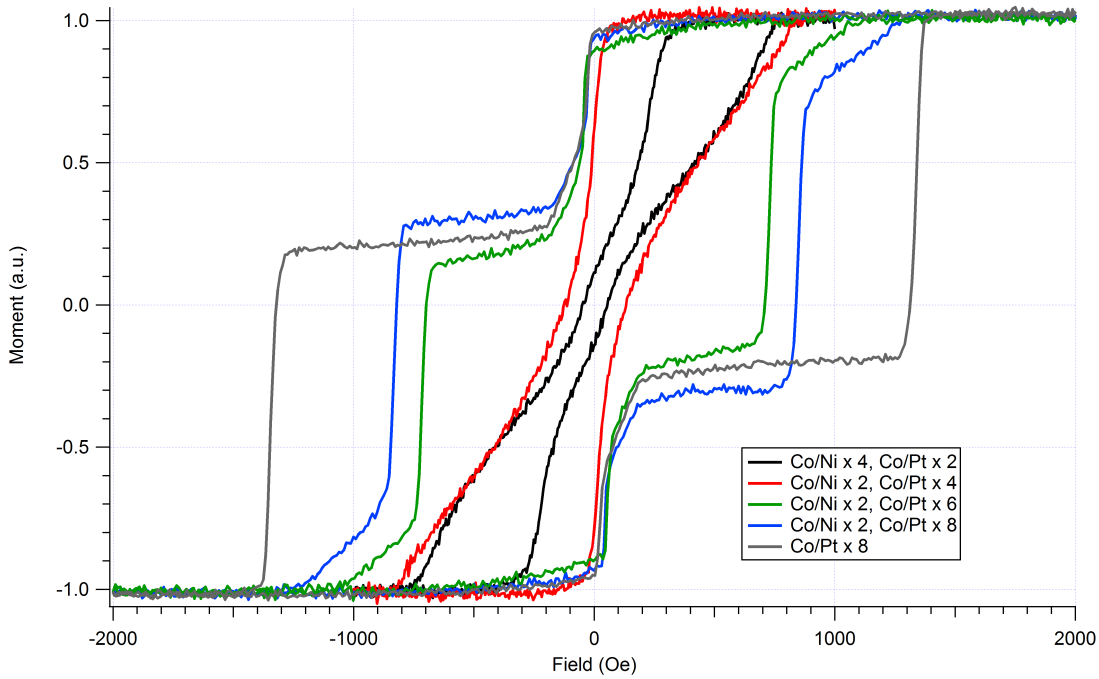

Figure 2.4: Comparison of $[Co(0.3)/Ni(0.35)]_n/[Co(0.3)/Pt(1.0)]_m$ multilayers with a different numbers of repetitions. The underlying bilayer is constant, Ta(3)/Pt(5)/Co(1.6)/Cu(5).

2.1.3 Co/Ni/Co/Pt Multilayers

Because large currents have the potential to destroy devices, it is beneficial to maximize the current polarization caused by the fixed layer. However, nonmagnetic layers, particularly platinum, decrease the polarization due to high spin-orbit scattering.

One way to increase the polarization is to add a Co/Cu/Co polarizer underneath the Co/Pt multilayer [47] [48] [49], but we had limited success depositing films of this type. Adding the polarizer significantly reduced the coercive field and also the PMA, and when the films were patterned into devices, frequently the polarizer would become in plane, likely due to sample heating during fab-

rication.

A second way to increase current polarization is to add a Co/Ni multilayer underneath the Co/Pt. Co/Ni has a higher magnetic volume and so polarization is significantly increased. Additionally, Co/Ni multilayers are reported to have a higher spin transfer torque efficiency and giant magnetoresistance [50]. The Co/Pt layers are kept because the Co/Pt interface has higher PMA and thus increases the coercive field of the entire stack.

The presence of Co/Ni in the multilayer lowers the coercive field and PMA appreciably, so the number of Co/Ni layers must be kept small. We found two repetitions of Co/Ni is optimal, with the cobalt and nickel thicknesses being similar to each other, around 0.3 nm. For the Co/Pt portion of the multilayer, we observed similar trends as before but with significantly lower coercive fields than the purely Co/Pt multilayers (Figure 2.4).

Unfortunately, Co/Ni/Co/Pt multilayers are more sensitive to the nanofabrication process, so we noticed a large decrease in pillar quality and yield when using these multilayers instead of the purely Co/Pt ones. Co/Ni/Co/Pt multilayers are also more sensitive to film nonuniformities discussed in the next section. Because of yield problems and time constraints, we switched to only Co/Pt multilayers for the later part of this work.

2.1.4 Other Factors Affecting Film Quality

So far, we've only discussed different variations of the recipe - layer thicknesses and number of repetitions. However, even if the same recipe is followed each

time, there are a number of other factors that may cause variation, sometimes to the point that the film no longer PMA.

First, it is worth reiterating that the chamber quality is critical to depositing good PMA films. The best indicator of chamber quality is base pressure. If the base pressure isn't low enough (as said before, $\sim 3 \times 10^{-9}$ Torr is a good guideline), then gettering (presputtering a reactive material such as titanium or aluminum for a very long time) is one potential solution. If that doesn't work, then a chamber or platen bake is in order. Presputtering each target is also a must, to remove any impurities that may be on the surface from prior depositions. I typically presputter each target for 20 minutes before sample insertion, then 5 minutes each before the actual deposition.

We've also noticed variation in PMA depending on distance from the center of the wafer (Figure 2.3d). This is likely due to the less-than-ideal sample rotation speed of our system. The center of the wafer has thicker, better quality films, and then the film thickness tapers off toward the edges. The bilayer is affected more than the multilayer, and it becomes more PMA toward the edges of the wafer. All deposition rates are calibrated for the center of the sample holder, so this makes sense that the film in the center corresponds to the expected parameters.

Lastly, a factor that is more difficult to account for is human error. Because our sputter system is controlled manually and the timing is on the order of seconds, a small delay in closing one of the shutters, for example, could slightly alter the film. Then if you add that slight uncertainty in time up over 15-20 layers, it's obvious why there might be variation in quality between depositions. This problem could be completely eliminated through automation of the sputter

system.

2.2 Imaging the Chiral Domain Structure of Co/Pt Films

Imaging stripe domains in the absence of field is fairly simple using a variety of techniques. However, a major challenge has been imaging in a perpendicular field and imaging complete devices. Here, I'll discuss our various attempts at imaging the domain structure.

2.2.1 MFM

Magnetic force microscopy (MFM) is a scanning probe technique that is essentially atomic force microscopy (AFM) with a magnetic tip. MFM is useful because it can be done quickly and easily in ambient conditions and because it has fairly good resolution, which, depending on the tip, can be as low as 20 nm. MFM is also nondestructive and doesn't require any special surface preparation.

One of the most commonly used MFM techniques is called lift mode and is a variation of tapping mode for standard AFM. In tapping mode, the cantilever/tip is vibrated close to its resonance frequency. Any force, F, on the tip will cause a slight change in the effective spring constant, $k_{eff} = k - \partial F/\partial z$, which will then shift the resonance frequency. If the tip is kept at a constant frequency, the shift can be seen as a change in vibration amplitude or phase. MFM lift mode scans each line twice (Figure 2.5). The first scan is used to obtain the topography and is done very close to the sample. For the second pass, the tip is lifted a certain height and follows the topographic contour. Only longer range

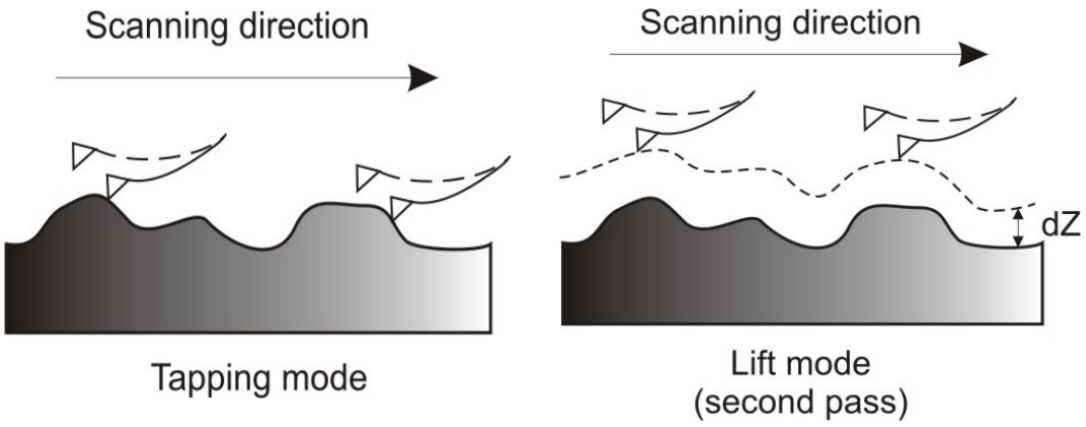

Figure 2.5: Basic principle of MFM lift mode operation [51]. The first scan (left) is used to obtain the topographical contour. The second scan at a height Δh records magnetic information.

interactions affect the tip, and magnetic contrast can be obtained [51] [52].

A few example MFM images of Co/Pt bilayers at zero field have already been provided in previous sections (Figures 2.1d-f and 2.2b-d). Because the films are very soft and the stray field from the magnetic probe tends to interfere with the domain structure, a low moment tip (MESP-LM) and a relatively large lift height (50-75 nm) must be used. Even so, we still see some domain manipulation by the tip during the initial topographical scan.

None of the AFM tools available to us have the capability to apply an out of plane field while imaging, and although commercial setups are available, to add such a capability to an existing tool would be very expensive. One solution that we explored was to instead apply a local magnetic field using a current loop patterned directly onto the sample (Figure 2.6a). For a loop of radius R and wire diameter d the magnetic field in the center for a given current I will be,

$$B \approx \frac{\mu_0 I}{2w} \ln\left(1 + \frac{w}{R}\right). \tag{2.1}$$

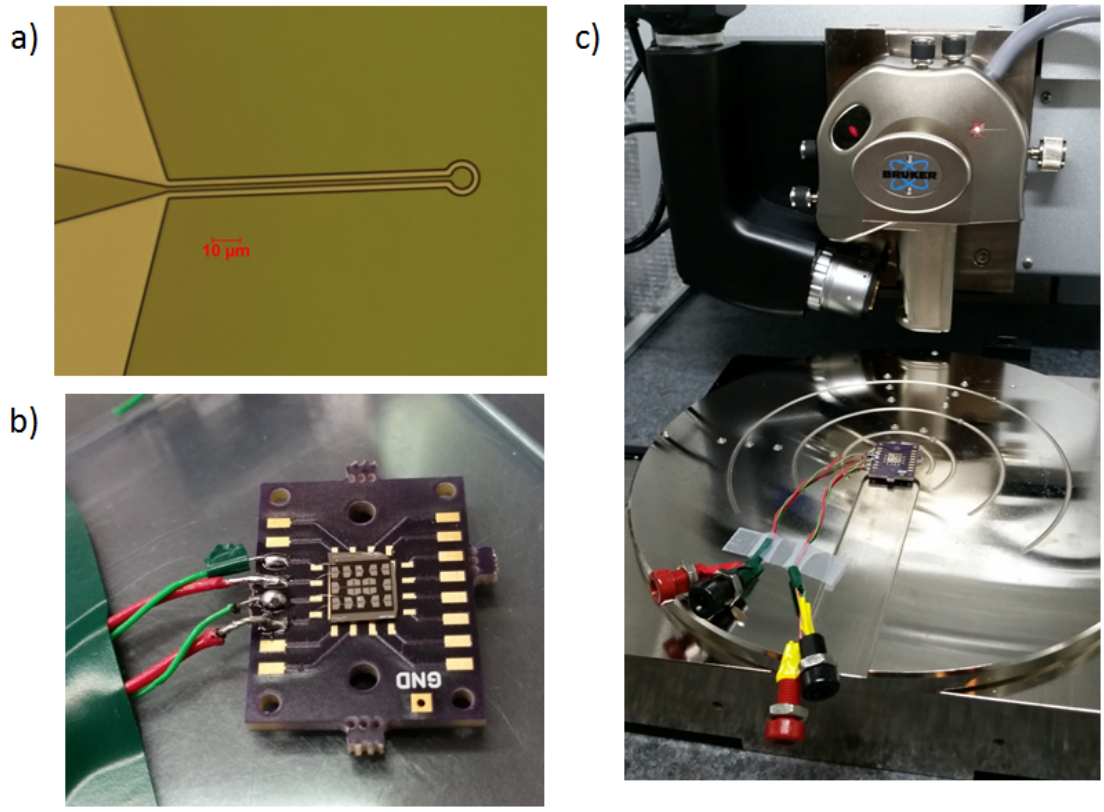

Figure 2.6: Attempting to apply a local magnetic field in an MFM setup. **a)** Device geometry. Imaging is done in the center of the current loop. **b)** Close-up of wire bonded sample. **c)** Photo of the entire setup. The banana plugs connect to an external current source.

This approximation does not take into consideration the thickness of the wire, the fact that the loop has a gap, or the fact that the film and wires are not entirely in the same plane. Devices were consistently able to withstand up to 100 mA for a 1 μm wide wire, which gives a field of roughly 12 mT in the center of a loop with 4 μm radius. This is comparable to the switching field for the bilayer, which is typically ~ 20 mT.

Originally the devices were fabricated in one step using liftoff. However, even with a 10 nm thick SiO_2 layer under the leads, most of the devices were

shorting through the film. We then added an additional lithography step where the film was ion milled into isolated dots in the center of the current loop. Once fabrication was complete the devices were wire bonded and mounted inside the AFM chamber (Figure 2.6b-c). Cables were run out of the AFM to a Yokogawa DC current source, which was grounded to the sample stage.

Unfortunately, despite our efforts, this technique did not work. There were two main problems. First, the film was very rough after fabrication, most likely from residual resist. Because the MFM signal is fairly weak, smoothness is important for getting a good image. A second more important problem, was that, when the current was sourced, the image was severely blurred and distorted. Even if we were able to solve the roughness problem, it is unlikely we would be able to resolve domains with the distortion. We would expect a perpendicular magnetic field to apply a constant force to the tip, which should just express itself as an offset, but the field in the center of the loop is not completely uniform. There is also a chance that the varying potential between the tip and sample is causing additional distortion. We thus had to turn to other options for imaging our samples in a magnetic field.

2.2.2 MOKE[1]

When light reflects off the surface of a magnetic material, its polarization changes, depending on the direction of magnetization. This is called the Magneto Optical Kerr Effect (MOKE). MOKE microscopy is a useful and versatile technique for imaging the domain structure in magnetic materials. It is noninvasive, can be conducted in ambient conditions, and imaging in a field is possi-

[1]The majority of this work was done by Alison Rugar for her undergraduate thesis [53].

ble. MOKE can also be used for magnetometry measurements. A slightly more unique feature is that magnetic films can be imaged in real time. This makes it a very powerful technique for studying the creation of skyrmions in a device. For example, Jiang, *et al.* were able to make videos of the formation of skyrmion bubbles at the end of a constriction [26] (see Section 1.6.2). Another useful application is that the DMI of a film can be determined by measuring field induced domain wall motion using MOKE [54] [55]. However, one severe limitation of MOKE is its spatial resolution. It is challenging, but not impossible, to obtain resolutions below 1 μm, and the maximum reported resolution is around 200 nm [56].

Several existing scanning laser MOKE setups were available for use at Cornell, however none were able to resolve the domains in our Co/Pt films. We then had the opportunity to image devices and bulk films in a commercial widefield MOKE setup at IBM Almadan[2]. Using this setup, we successfully resolved stripe domains in the magnetically soft Co(1.7)/Pt(5) bilayer (magnetometry and MFM data in Figure 2.1c,f), and at nonzero fields below saturation, we observed isolated domains that could be skyrmions (Figure 2.7).

Because of our success with the microscope at IBM Almadan, Alison Rugar, as part of her senior undergraduate thesis work, proceeded to build a similar widefield MOKE setup that mounts on the projected field magnet probe station in our lab. Her setup currently has a resolution of roughly 1.7 μm and can image relatively large stripe domains in a Co/Gd alloy sample. Although improvements in the optics are necessary to resolve the much smaller domains in my Co/Pt films, magnetometry was possible and the data was in agreement

[2]Thank you to Chirag Garg, from the Max Planck Institute of Microstructure Physics, for assisting Alison with these measurements.

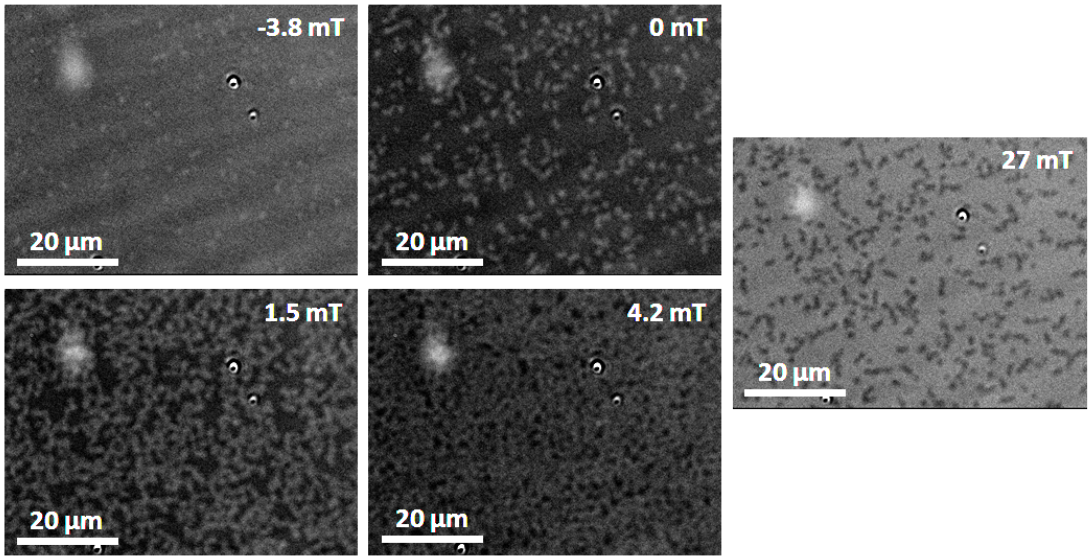

Figure 2.7: Widefield MOKE images of soft Co(1.7)/Pt(5) films showing the evolution of chiral domains with an applied perpendicular field. The film is initially saturated in the negative direction, which corresponds to the darker regions. Magnetic field values are approximate.

with VSM measurements [53].

2.2.3 Scanning SQUID[3]

Scanning SQUID microscopy is an imaging technique that uses a superconducting quantum interference device (SQUID) to locally sense the magnetic field. SQUID is one of the most sensitive magnetic field sensors known, and so, unlike MFM or MOKE, scanning SQUID can get decent magnetic contrast even through many layers. However, a downside to this technique is the resolution, which is proportional to the size of the probe. The probe is a nanopatterned current loop (Figure 2.8), so even using electron beam lithography, resolving

[3]Imaging work done by George Matthew Ferguson in the Katja Nowack group at Cornell.

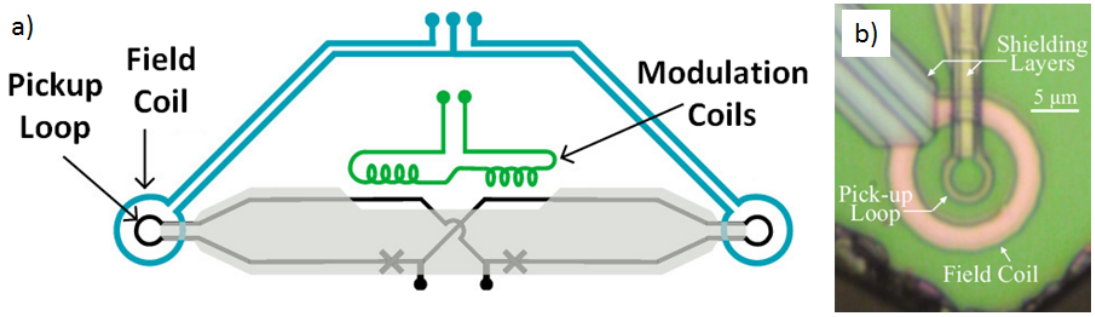

Figure 2.8: Scanning SQUID probe. **(a)** Device schematic. The probe has the capability to apply a local field using a current loop. The modulation coils and geometry are designed to maximize the sensitivity. **(b)** Close up of pickup loop in an actual device. Images from [57].

features much below a micron is challenging. Another problem is probe size is inversely proportional to sensitivity, so while a smaller probe might be able to resolve smaller features, it won't be as capable of imaging very weak fields [57]. Because it relies on superconductivity, scanning SQUID is a low temperature technique, typically performed at liquid helium temperatures (4.2 K).

The Nowack group at Cornell has been in the process of setting up a scanning SQUID microscope, and thus, I had the opportunity to try out the technique on some of my samples. The eventual goal was to be able to image full devices, because MFM and MOKE could not resolve the domain structure through the thick protective oxide layer and top contacts. The Nowack group's microscope uses a probe similar to the one in Figure 2.8, except it was not set up to do measurements in an applied field yet. Even though the resolution is nominally 1 μm, they were able to resolve what appeared to be stripe domains in my soft Co(1.65)/Pt(10) films (Figure 2.9a-b).

Stripe domains in one of my spin valve devices were also observed (Figure

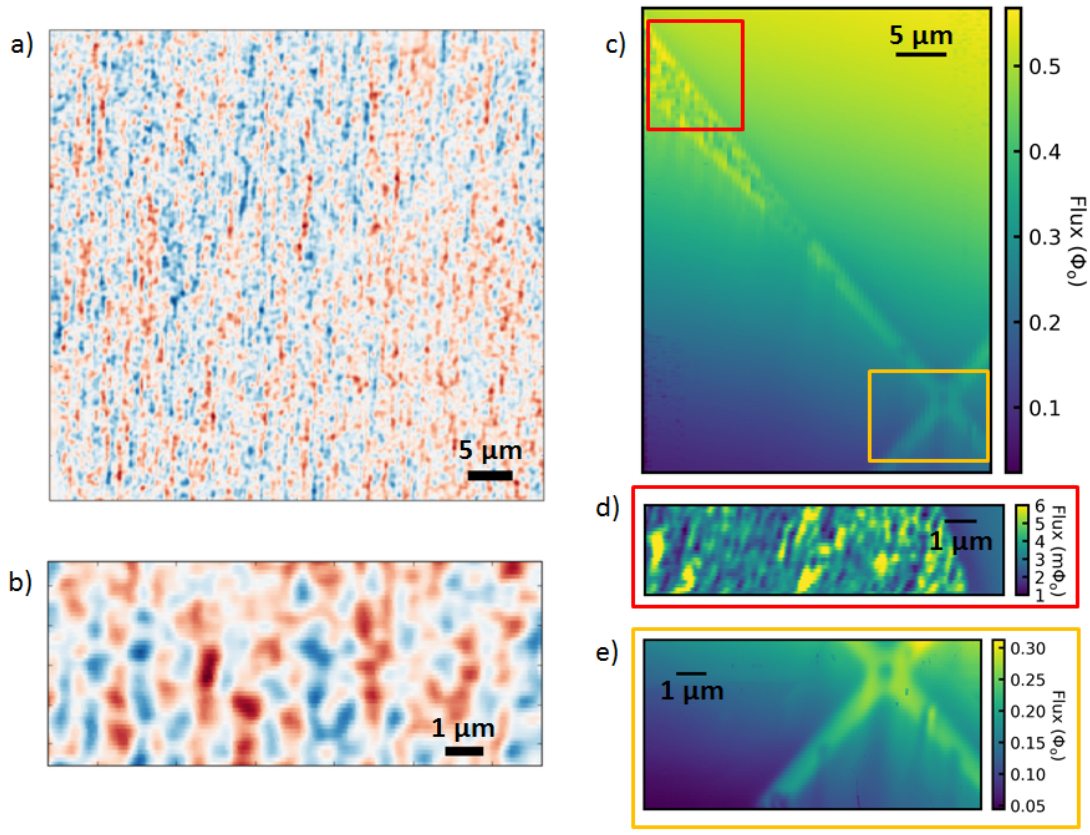

Figure 2.9: Scanning SQUID images of **(a-b)** Co(1.65)/Pt(10) bulk films with stripe domains and **(c-e)** a spin valve device. **(d)** and **(e)** are zoomed in images of the red and yellow boxes in **(c)**, respectively. (Sample temperature ~ 8 K.)

2.9c-e), although interestingly the center near the pillar appears monodomain. Whether this is because the resolution limit has been reached or because it is actually monodomain requires more analysis, which is underway and likely to be finished after this thesis is presented. Regardless, the fact that stripe domains in devices can be imaged using this technique and that the geometry above is essentially invisible is very promising. Additionally, the setup will have applied field capabilities fairly soon. Potential experiments with these materials are currently being explored.

2.2.4 Lorentz TEM[4]

While most other magnetic imaging techniques, such as MOKE and scanning SQUID, are limited by spatial resolution, Lorentz Transmission Electron Microscopy (L-TEM) has a resolution down to about 5 nm with excellent magnetic contrast. It is also possible to image in a magnetic field. The downsides are that sample preparation takes more time and equipment costs can be fairly expensive.

Until recently, L-TEM was used to image only Bloch skyrmions because it was believed that Néel domain walls were invisible to this technique. Contrast is formed by the deflection of the electron beam by an in-plane magnetic field, which either increases or decreases the signal in a particular region. If the beam is normal to the sample, this means that electrons are deflected along the domain wall and do not get imaged. A way of saying this mathematically is that the contrast is proportional to the curl of the magnetization along the beam propagation direction. For Néel skyrmions, the curl is entirely in the sample plane, so for an orthogonal beam, this gives zero contrast. However, it was discovered that if the sample is tilted relative to the beam, contrast can be obtained because there is now a portion of the curl along the beam propagation axis [58].

We have attempted to image our Co/Pt bilayers using L-TEM. However, this is an ongoing project that will likely be finished after this thesis is submitted. The films need to be deposited on silicon nitride membranes, and we encountered a problem with the tantalum adhesion layer beading up rather than forming a continuous layer. Once the samples are made with either a thicker tantalum layer or a different adhesion layer, I expect we will be able to success-

[4]Imaging work done by Kayla Nguyen in the David Muller group at Cornell.

fully image the domain structure as a function of field.

CHAPTER 3

METHODS - EXPERIMENTAL SETUP AND DEVICE FABRICATION

The next step after developing and characterizing a Co/Pt film recipe is to fabricate it into devices. The geometry shown in Figure 3.1 was used for both projects discussed in this thesis. We start with films of the type Ta(3)/(Co/Pt bilayer)/(Copper spacer)/(fixed layer)/Pt(10). The bottom leads of the device consist of the Co/Pt bilayer and copper spacer patterned into a cross shape. The fixed layer is patterned into a nanopillar in the center of the cross. The area immediately surrounding the pillar is covered in a protective oxide layer, and then top and bottom contacts are made such that current can be applied through the pillar into the bilayer underneath. In this chapter, I will outline the basic measurement setup and fabrication process for my spin-valve like devices.

3.1 Measurement Setup

The resistance of our devices is measured using a standard four point lock-in technique, with an audio frequency sense current of $\sim 100\,\mu$A. A projected field magnet is used to apply an external field perpendicular to the sample plane. Giant magnetoresistance (GMR) scans are used to characterize devices. Good devices show two clear switching events corresponding to the bilayer and the nanopillar, with the pillar being at a much higher field than the bilayer. Good devices also don't show significant pillar degradation. Pillars whose quality has been affected by the fabrication process have a lower coercive field than the bulk multilayer film, and they have a slightly higher resistance, usually above 20 Ω, whereas the best pillars have a resistance between 8-12 Ω. The distribution

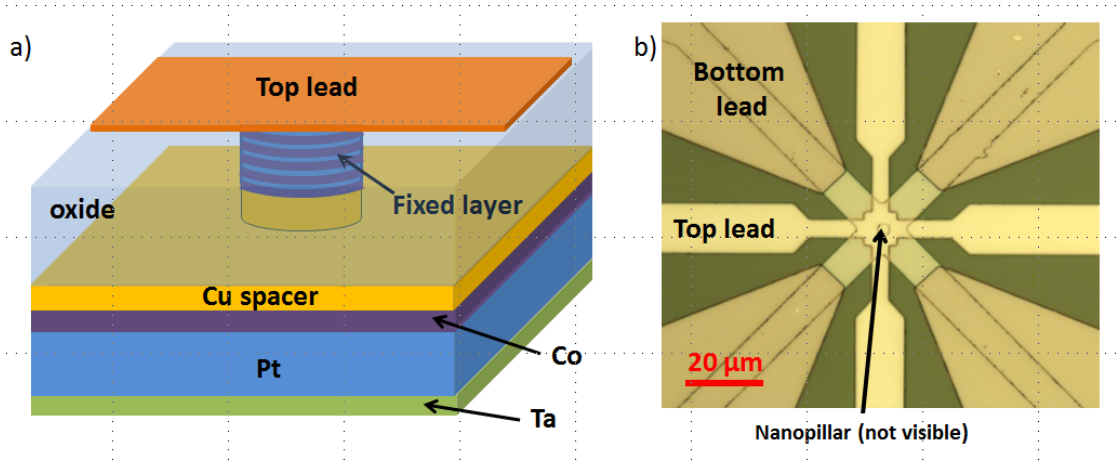

Figure 3.1: Spin valve device design. **a)** Cartoon showing a side view of a device. Features are not to scale. **b)** Optical microscopy image of a finished device with a 100 nm diameter pillar. The square in the center is a hole through the oxide layer so the top leads may contact the pillar. The pillar is too small to see.

of pillar quality on a sample is random, and, other than the fabrication details mentioned later in this chapter, we have not noticed a pattern. The average pillar yield is around 10%, assuming nothing goes wrong during fabrication, so it is important to make a large number of devices at once.

The AC lock-in signal is added to a DC current (we typically use up to 7 mA) using an audio transformer. We include a low pass filter in the circuit to reduce noise introduced by the transformer (Figure 3.2). Current sourced through the nanopillar into the bilayer becomes polarized by the pillar. This polarized current should then exert a spin transfer torque on the bilayer and nominally either excite skyrmion dynamics or create a static domain in the region immediately under the pillar. We measure the pillar resistance (GMR) both as a function of current at fixed field and field at fixed current to develop a phase diagram for the devices being studied.

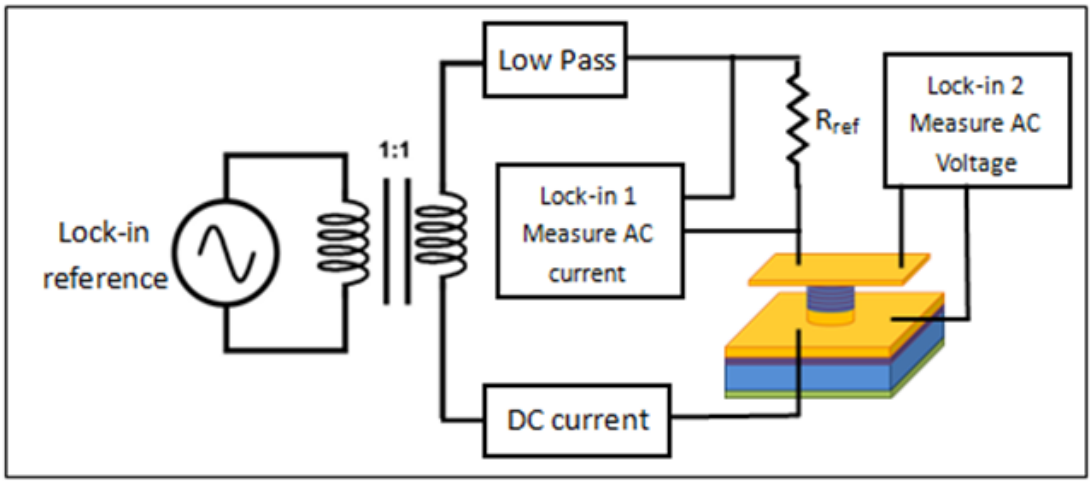

Figure 3.2: Schematic of the measurement setup used for measuring DC current and field dependence.

An additional feature of our device design is that, because the bottom leads are patterned into a cross shape, we can independently monitor the state of the bulk bilayer using the anomalous Hall effect (AHE). The anomalous Hall effect is an additional contribution to the Hall voltage observed in ferromagnetic materials that directly depends on the magnetization. In other words, when a current is applied through the film, a voltage can be measured transverse to the current that changes when the magnetization of the film changes direction. This allows us to separate behavior local to the pillar from bulk behavior. We make devices with a variety of Hall cross widths, which further helps to separate out bulk effects.

In certain situations, the AHE appears in the four point GMR measurements (Figure 3.3a). If the voltage probe is on a lead perpendicular to the current lead, we observe a small contribution from the AHE. This contribution is distinguishable from the GMR because it does not depend on the orientation of the pillar. This means it is asymmetric with respect to the sign of the field, whereas

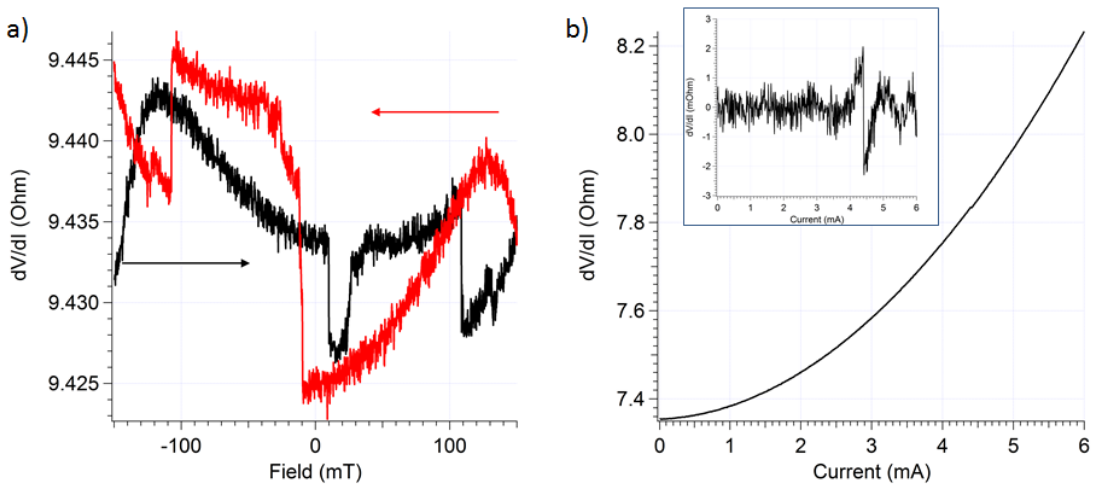

Figure 3.3: Commonly encountered background in the GMR signal. **(a)** Example of a GMR measurement with a very large AHE signal. The AHE is antisymmetric with respect to field, whereas the fixed and free layer switching events are symmetric. Periodic background from probe motion is also visible. **(b)** Large parabolic background in a DC current scan from Joule heating almost completely obscures the switching event. Inset - the switch is clearly visible after subtracting out a polynomial fit.

switching related to the pillar will be symmetric, assuming the field scan is wide enough to switch both the fixed and free layers. Another situation in which the AHE may appear in the GMR signal is if the pillar is slightly off center. In this case, the AHE contribution will be present regardless of which lead is used to measure the voltage, but it can still be distinguished from GMR by the fact that it is always asymmetric with field. This background can still be somewhat confusing, particularly for minor loop scans, so I try to avoid it by finding devices that have a centered pillar and by placing the voltage probe on a lead directly opposite the current probe.

We typically see a small hysteretic background on the order of 0.01 Ω due to probe motion with the applied field (Figure 3.3a). Wire bonding gets rid of this

background, but because of low device yield and the risk of destroying devices, we prefer to use probes for most of our measurements. The background is easily distinguished from magnetic switching because it changes with scan rate, step size, and the width of the field scan. In the absence of this background, the signal would be flat, except for magnetic switching events.

There is also a large parabolic background from Joule heating with applied DC current. This background is fit with a high order polynomial and subtracted from DC current scans (Figure 3.3b). Joule heating can also affect field scans, particularly if measurements have been running for a long time on one device. We sometimes see repeated scans having a resistance slightly offset from one another, but the switching fields and change in resistance do not change. Because we are mainly interested in changes in resistance rather than absolute resistance, subtracting the background or offsetting the data, as I do in some of my analysis, is acceptable.

3.2 Device Fabrication

In this section, I will discuss in detail the fabrication of the spin-valve-like devices shown in Figure 3.1. This is a challenging five step lithography process, one step of which involves electron beam lithography. The specifics will likely vary depending on what tools are used, but this will hopefully provide useful guidelines for fabricating devices with similar geometries in the future. We start with bulk films deposited on a high resistivity silicon substrate, which is suitable for measuring high frequency dynamics, should they exist. For more information on bulk film deposition, please refer to the previous chapter.

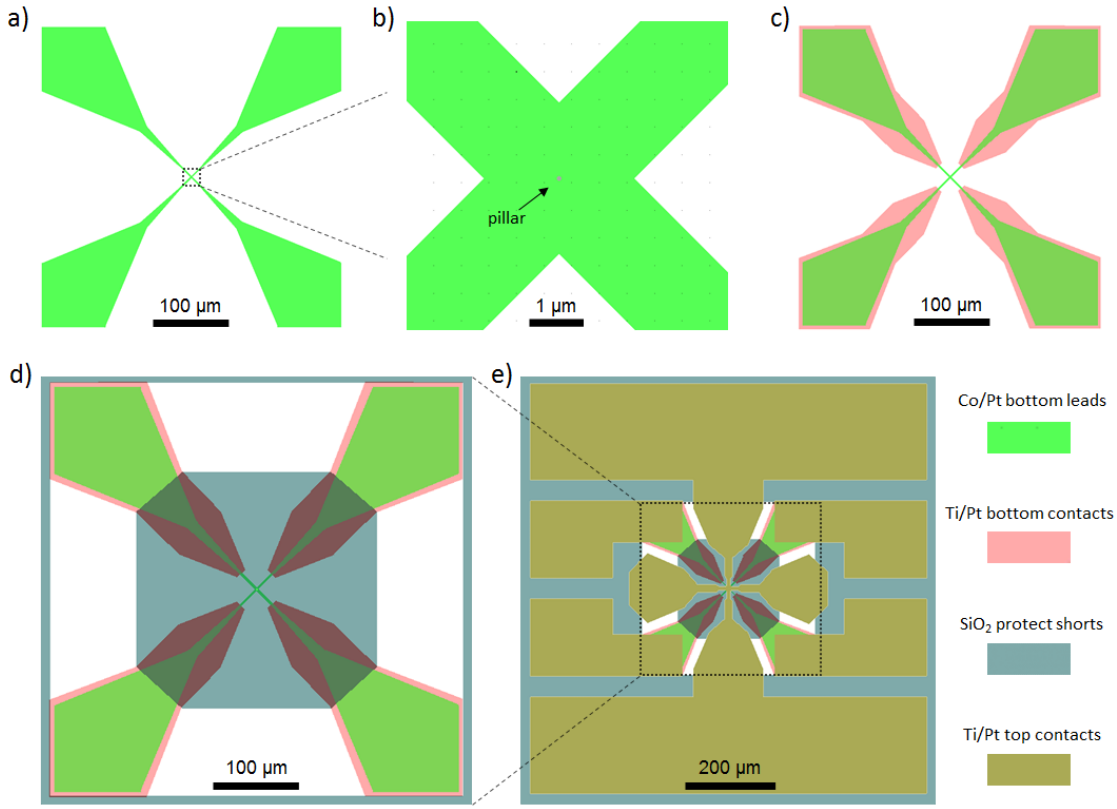

Figure 3.4: Overview of nanofabrication process for devices with 2 μm wide leads. **(a)** Etch bulk Co/Pt film. **(b)** Etch nanopillar and deposit protective oxide. **(c)** Etch through oxide and deposit Ti/Pt bottom contacts. **(d)** Deposit more protective oxide around pillar. **(e)** Deposit top contacts.

Most of the processing is done using tools in the Cornell Nanoscale Science and Technology Facility (CNF). Photolithography is done using the 5X g-line stepper, and unless otherwise noted, an LOR/Shipley bilayer is used. Exact recipes are included in Appendix B.

3.2.1 Step 1 - Etch Bottom Leads

The first step is fairly simple - unaligned photolithography followed by ion milling using the setup in the Buhrman lab (Figure 3.4a). The bulk film is etched into Hall crosses, and alignment marks for both ebeam and photolithography are added on the edges of the die. LOR is not necessary for this step, although it does make resist removal easier. Heating in the ion mill tends to crosslink Shipley resist, making it difficult to remove. It is absolutely critical to ensure all resist is gone after stripping, since any left over will be etched into the film in the second step. Sonication or heating the stripper (1165 or PG remover) to 100-120°C can help. It is also a good idea to intermittently close the shutter during ion milling (I use 10 seconds open / 30 seconds closed) to keep the sample from getting too hot. The Buhrman setup has a program to handle this, which also makes the timed etch in step 2 easier. Timing this first etch isn't necessary as long as the multilayer is etched down to the substrate.

3.2.2 Step 2 - Nanopillars

Next, the nanopillars are created (Figure 3.4b). This is by far the trickiest, most expensive, most time consuming, and most prone to failure step, so extreme care must be taken.

The first part of this step is aligned electron beam lithography using the JEOL 6300 tool in CNF. We use a PMMA/HSQ bilayer (see Appendix B for details). HSQ is a negative resist, which means exposed parts remain after development, and the purpose of the PMMA is to assist with resist removal. The resist does not adhere very well to most substrates, so developing is a bit tricky. It is best

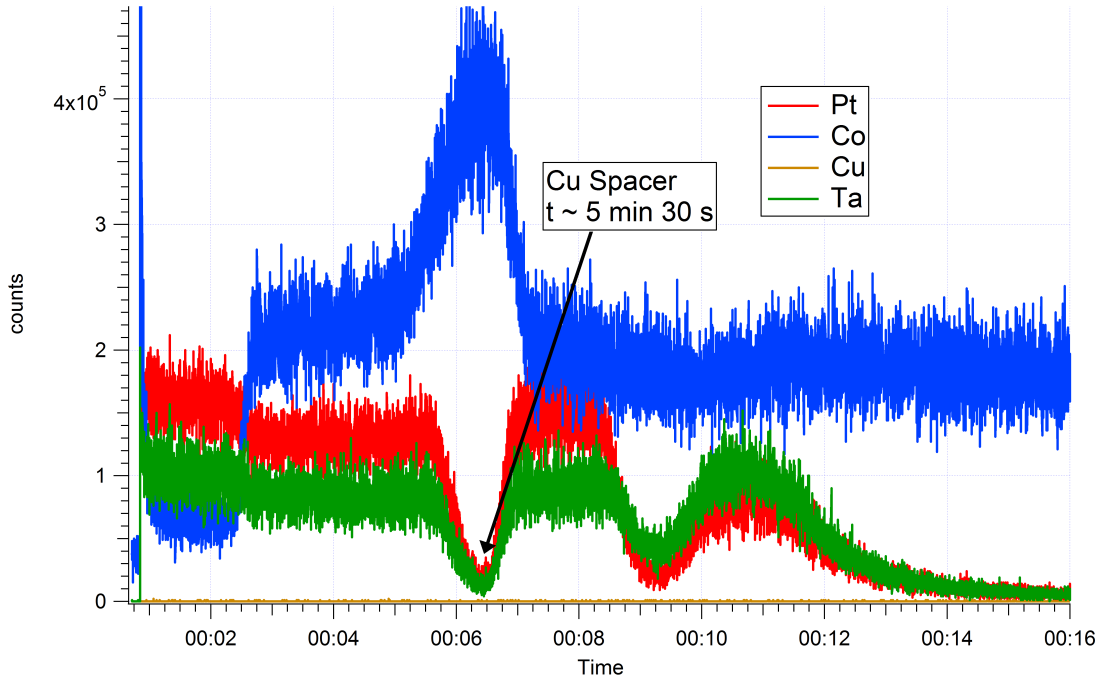

Figure 3.5: Mass spectrometer data used to calibrate the ion mill etch time for creating nanopillars.

to not move the sample around while it's in the developer, to rinse by dipping into DI water, and then mostly blow dry the sample from the back. Even when these precautions are taken, we still see a small number of pillars displaced or removed. After using developer, a gentle oxygen plasma clean is used to remove PMMA in regions not under the patterned HSQ.

Once the resist is patterned, the next step is to ion mill the pillars. The etch is done at a 150° angle to prevent fencing. As already mentioned, this is a timed etch, since we need to etch down to about halfway through the copper spacer. End point detection is not used because the signal is too weak for patterned samples. Instead, we etch a sacrificial bulk film at the desired angle, and use a mass spectrometer to record which elements are released at which times during

the etch (Figure 3.5). The copper signal is not very reliable, so we look for a dip in the platinum signal or a large peak in the cobalt signal, which corresponds to the spacer layer. The reason cobalt has a peak there is because its atomic mass is very similar to copper. Platinum and tantalum also usually look similar for the same reason. Once ion milling is complete, before venting the system, we deposit about 4 nm of aluminum *in situ* using the attached sputter gun. The aluminum should oxidize almost immediately when exposed to air, and its purpose is to protect the sides of the nanopillars while the samples are transported over to CNF.

The final part of this step is to deposit approximately 80 nm of silicon dioxide around the pillars using electron beam evaporation. The oxide is present to prevent shorting between the top and bottom leads and also to protect the sides of the pillar from oxidation. The thickness of silicon was chosen to be large enough to mushroom into the undercut around the pillar, but thin enough to be capable of liftoff. To prevent possible deterioration of the pillars, it is important to get them into the evaporation chamber as quickly as possible. Including walking time, the fastest I've been able to do this is about 15 minutes. Even though it takes longer, we have found that the evaporator in CNF has better yield than the one in Clark because the samples are further from the source, which means less shadowing that leads to shorting around the pillar.

Lastly, it is time to strip the resist and lift the silicon dioxide off the tops of the pillars. We soak the samples in PG Remover heated close to its flash point for at least 5 hours, and then sonicate for at least another 1.5 hours. Sometimes these steps need to be repeated if the pillars didn't lift off. Whether they lifted off can be quickly determined using an optical microscope (they look black if

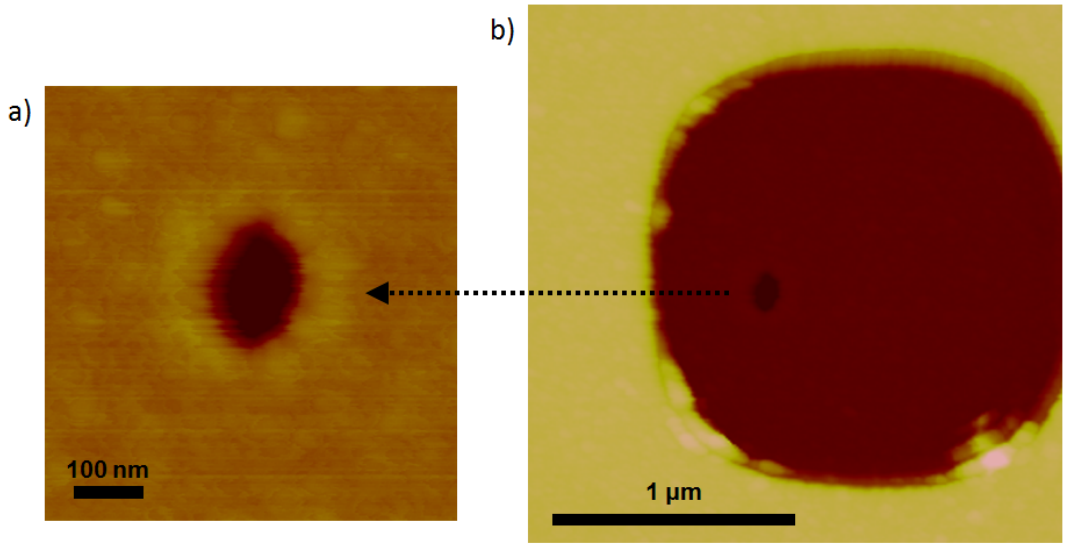

Figure 3.6: Atomic force microscopy images of a device with a good pillar. **(a)** After the second lithography step. The pillar will look like a hole in the protective oxide, which is much thicker. **(b)** After the fourth lithography step. The second layer of oxide makes up the larger 2 μm window.

the resist is still there), or for someone less familiar with what to look for, AFM can be used (Figure 3.6a). Using AFM, a good pillar will look like a hole with the correct dimensions, since the protective oxide is much thicker.

Because this is a very complex process with many aspects that can go wrong, I've included additional tips for troubleshooting in Appendix B.

3.2.3 Step 3 - Bottom Contacts

After verifying that all the pillars have lifted off properly, the next step is to etch through the SiO_2 and deposit contact pads for the bottom leads (Figure 3.4c). The pattern is made with photolithography, and then a CF_4 reactive ion etch

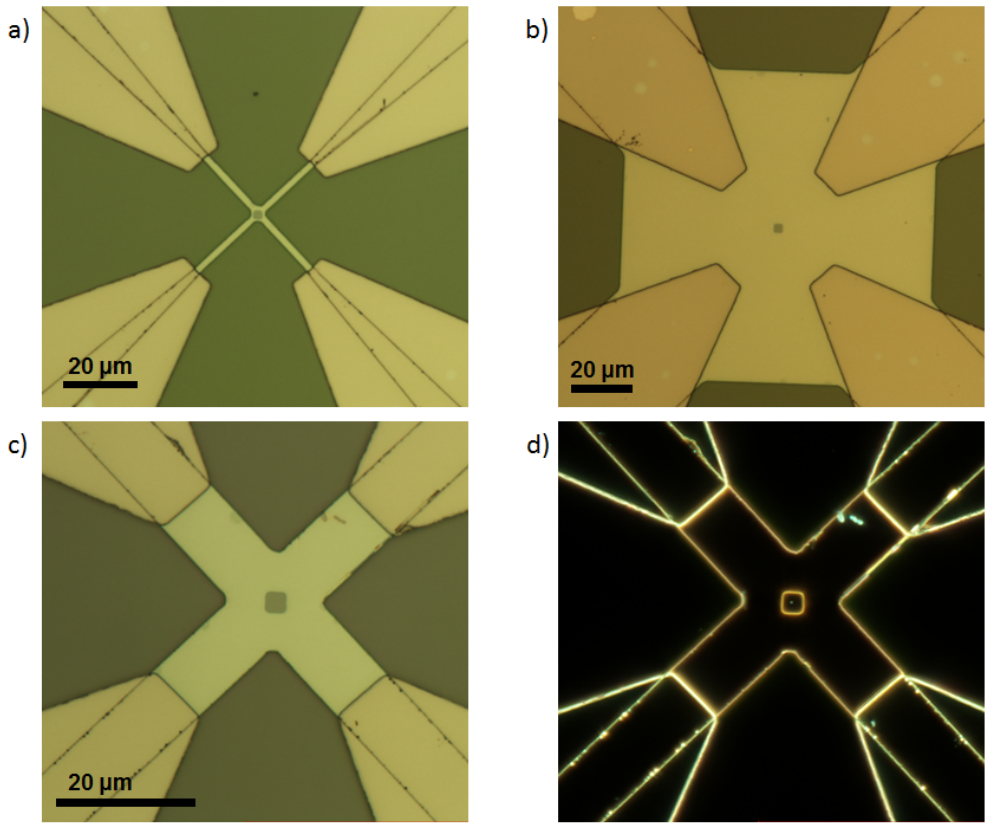

Figure 3.7: Optical microscopy images showing the extra protective oxide layer after the fourth lithography step, as well as the three different bottom lead sizes, **(a)** 2 μm, **(b)** 100 μm, and **(c)** 10 μm wide. **(d)** shows the dark field image of the same device as **(c)**. Note that the pillar is now visible.

process removes SiO_2 in the areas where we want to contact the bottom leads. We run a 2 minute argon clean process in the sputtering system and deposit Ti/Pt contact pads immediately after.

3.2.4 Step 4 - Protect Shorts

The 80 nm of SiO_2 that was deposited in step 2 isn't always enough to prevent the top and bottom leads from shorting where they overlap. To ensure that only the pillar is making contact with the top leads, we deposit an extra 70 nm of SiO_2 in the region surrounding the pillar (Figure 3.4d and Figure 3.7). A small window is lifted off in the center where the pillar is (Figure 3.6b). These windows are a bit difficult to align, since the 5X stepper has a slight shift and distortion of the pattern, but I have compensated for these discrepancies in the mask design. A shorter development time is needed because of the small size of some of the features. Liftoff is also a bit tricky. To ensure the windows are removed properly, the samples should be heated in stripper for several hours and then sonicated for at least 90 minutes.

3.2.5 Step 5 - Top Contacts

The last step is to make the top contacts. The geometry was designed to make Hall measurements easy to do with two point probes (Figure 3.4e). A second feature is that two of the top contact pads are extended such that the sample doesn't need to be rotated to try different measurement configurations. Since this step will cover the pillars, any remaining pillar imaging and characterization needs to be done first. I typically look at each individual device in an optical microscope and write down which ones are good and which ones are bad. It takes some practice to learn what a good pillar looks like, and it helps to look at them in both light and dark field at the highest magnification (Figure 3.7d). As said earlier, a pillar that hasn't lifted off looks black, and if no pillar

is visible, that usually means it was blown away during development in step 2. However, optical microscopy is only a way to rule out bad devices. Frequently a device may look perfect under a microscope, but there will be problems with its magnetic properties that can be only determined through magnetoresistance measurements.

Fabrication for this step is simple. Top contacts and an extension of the bottom contacts are made using photolithography and sputtering. Similar to step 3, a two minute argon clean process is run prior to depositing Ti/Pt contacts. After lift off, the devices are ready for measurement.

CHAPTER 4

ATTEMPTING TO EXCITE SKYRMION DYNAMICS IN HARD CO/PT BILAYERS

Hard Co/Pt bilayers, that is films with a thinner cobalt layer and sharp magnetic switching, have a strong DMI but also a much stronger PMA than films with a thicker Co layer. The strong PMA causes stripe domains and skyrmions to be virtually nonexistent. However, it has been predicted to be possible to excite topologically nontrivial dynamics in such films using spin transfer torque, and possibly static skyrmions if the DMI and current density are large enough. Topological or skyrmion dynamics could be useful as a microwave nano-oscillator or spin wave emitter, and, to date, not much work has been done experimentally to study these modes. In this project, we attempt to excite skyrmion dynamics in Co/Pt films using the device geometry and characterization techniques discussed in the previous chapters.

4.1 Background

This project was originally prompted by communication with Giovanni Finocchio, a theorist at the University of Messina in Italy. His group did micromagnetic simulations of Co/Pt devices with the spin valve geometry shown in Figure 4.1a [59], using parameters for the multilayer, Pt(5nm)/Co(0.6nm)/Cu (4nm)/CoPt(4nm), which is very similar to the multilayers I fabricated (see Chapter 2). A nanopillar, here with a diameter of 70 nm, acts as a local spin current injector into the Co/Pt bilayer underneath. They found that, depending on the current density through the pillar and the interfacial DMI constant, D,

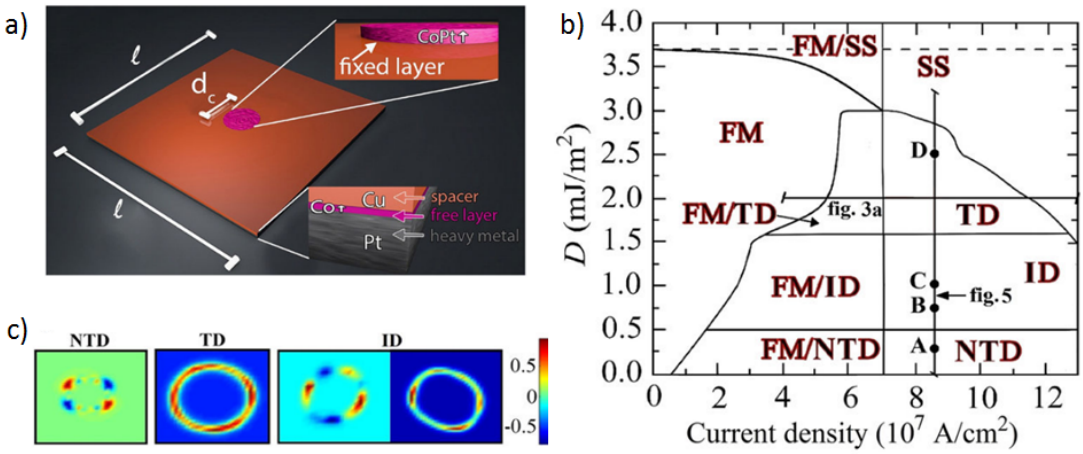

Figure 4.1: Micromagnetic simulations of **(a)** PMA Co/Pt spin valve devices. **(b)** Phase diagram of the magnetization ground state at zero field as a function of applied current density (negative) and interfacial DMI constant, D. Acronyms are as follows - FM: ferromagnetic, SS: static skyrmion, TD: topological droplet, NTD: non-topological droplet, ID: instanton droplet. **(c)** Spatial distribution of the topological density for the three types of dynamics. [59]

for the Co/Pt bilayer, a variety of different behaviors could occur (Figure 4.1b).

Nontopological droplets (NTD), which have a skyrmion number $S = 0$, occur for very low values of the DMI ($D \leq 0.5$ mJ/m^2). While topologically trivial, these phases can have an interesting distribution of the topological density (Figure 4.1c), which is the integrand for the skyrmion number (Equation 1.4). NTD dynamics are single mode and characterized by a 360° in-plane rotation of the domain wall spins. The DMI in our Co/Pt bilayers is too large to observe these modes.

Topological droplets (TD), or dynamical skyrmions, which have a skyrmion number of $S = 1$, occur for $1.6 < D \leq 3.0$mJ/m^2. At any given time, the TD is topologically nontrivial and looks like a skyrmion. Its diameter oscillates

with time (hence why it's called a "breathing mode") and the spins around the core rotate, switching the texture back and forth between a Néel and Bloch type skyrmion. TD's are single mode, and the frequency decreases with increasing current, until at a large enough current, a static skyrmion (SS) is formed. For the range of D where TD are supported, the static skyrmion is stabilized by the DC current and will go away at lower current densities. If $D \geq 3.7$ mJ/m^2 (dotted line in Figure 4.1b), however, the skyrmion, once created, will be stable even at zero current.

Instanton droplets (ID), dynamics which have a time domain variation of skyrmion number, are expected to occur at intermediate values of the DMI ($0.5< D \leq 1.6$mJ/m^2). Instanton droplets are characterized by an oscillation between a topological and nontopological droplet. These dynamical states are not single mode and, as a result, they generate incoherent spin waves. The Fourier spectra are noisy, which makes it easy to distinguish from TD and NTD states.

Because our hard Co/Pt bilayers do not exhibit any stripe domain structure at zero field, measuring the DMI is difficult. DMI is an interfacial effect in these materials, so we would expect it to be roughly the same magnitude as our thicker films, which do have observable domains at zero field. Comparing the domain size for our softer films to micromagnetic simulations, the DMI is between 1.0-2.0 mJ/m^2 (see the next chapter for a more thorough discussion of this), which means we should be able to observe either instanton or topological droplets.

These simulations were done for a pillar size of 70 nm; however, they found that the phase diagram is qualitatively similar for different pillar sizes. Favorable to our experiment, dynamics can be excited using a 100 nm diameter pillar

at lower current densities than a smaller pillar. If the pillar is too small (< 50 nm), then dynamics cannot be excited without the presence of an external out of plane field.

4.2 Mumax3 Simulations

The Finocchio group's results did not take into consideration the application of an external magnetic field, and they mostly focused on devices with a 70 nm pillar, while my devices use a 100 nm pillar. They also did not study the effects on softer Co/Pt bilayers. For these reasons, I decided to do some simulations on my own using an open-source GPU-based micromagnetics program called mumax3 [60] [61]. Mumax3 was chosen because it is both fast, offering speeds up to 100x that of CPU-based simulations, and relatively easy to use. It uses the finite difference approach, which divides the simulation up into a rectangular mesh and is efficient for thin film geometries without any curved surfaces. I use a mesh size of 4 x 4 x 1 nm^3, which is much smaller than the domain length scale. These simulations are 3D, i.e. there is more than one voxel in every direction.

From magnetometry data, we estimate the saturation magnetization to be 1.1 $\times 10^6$ A/m. By saturating the film in plane, we find the anisotropy field to be 1000 Oe, which we can then use to calculate the first order uniaxial anisotropy constant,

$$H_K = \frac{2(K_1 - \frac{1}{2}\mu_0 M_s^2)}{\mu_0 M_s} \rightarrow K_1 = \frac{1}{2}\mu_0(H_K M_s + M_s^2) \tag{4.1}$$

where M_s is the saturation magnetization and K_1 is the anisotropy constant. Using this equation we get, $K_1 = 8.6 \times 10^5$ J/m^3. These values are very similar to those used in Carpentieri, *et al.* [59].

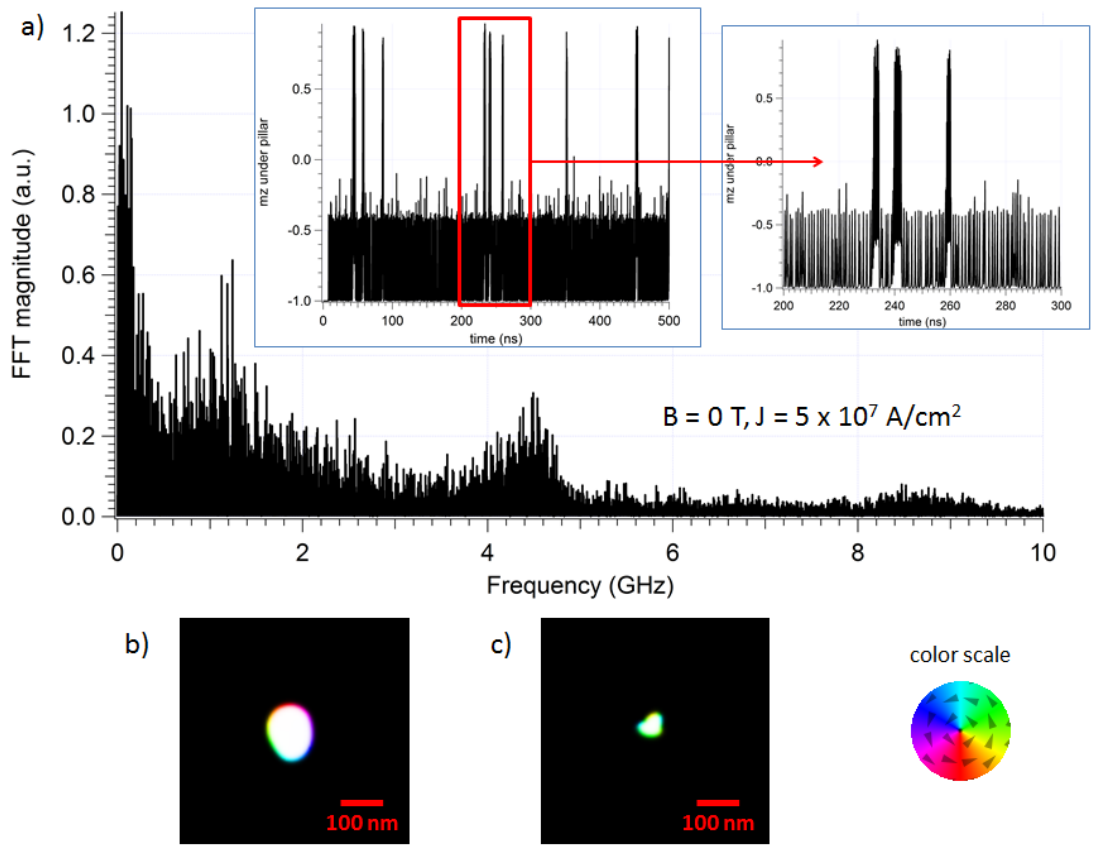

Figure 4.2: Example mumax simulations showing an instanton droplet in a device with 100 nm pillar and B = 0 T, J = 5 x 10^7 A/cm^2. The inset of **(a)** shows the time dependent z component of the bilayer moment under the pillar. **(a)** Taking the Fast Fourier Transform (FFT) of this data shows two broad peaks corresponding to the topological and nontopological components. **(b)** and **(c)** are snapshots of the magnetization showing topological and nontopological modes, respectively.

Our simulations are done for a 100 nm pillar, which is emulated by defining a circular region in the center of the film with a spin polarized current. Only the bilayer is simulated, meaning possible dynamics in the nanopillar are not taken into account. One limitation is that the simulations are done at zero temperature and don't take thermal effects into consideration. Such effects could potentially assist dynamics, which would lower the current density required experimen-

tally. We also do not know what the spin polarization is in our devices. Based on prior work done by the Buhrman group at Cornell, I would guess the polarization is 20% or less, but for simplicity's sake, I use $P = 1$ in most of my simulations. Of course this is a vast overestimate, meaning the actual current required will be quite a bit larger, but the qualitative behavior should be the same. The intent was to fine tune the simulations to estimate P once I had repeatable measurements to compare them to. Lastly, mumax3 does not include the Oersted field, but because it is mostly in-plane near the pillar, we do not expect it to have a strong effect on the qualitative behavior. More detailed simulations would have been done, should the experiment have progressed to the point of having consistent results.

For all calculations discussed here, the device is initialized in the antiparallel configuration, with the fixed layer in the $+z$ direction. Positive current densities correspond to current going in the $+z$ direction, which is equivalent to a negative current in our experiments and favors parallel alignment. Negative current densities in the simulation do not excite dynamics when the device is in the antiparallel state.

As expected, instanton droplets are created at zero field and moderate current densities. The example in Figure 4.2 shows dynamics for $J = 5 \times 10^7$ A/cm^2, which corresponds to a current of ~4 mA or larger in our devices. The frequency spectrum consists of two dominant modes - approximately 1.2 GHz corresponding to the nontopological component and 4.5 GHz for the topological component. The topology of a given mode is verified visually by looking at snapshots of the magnetization in time. The transition between topological and nontopological modes is irregular. The oscillation amplitude of the lower frequency

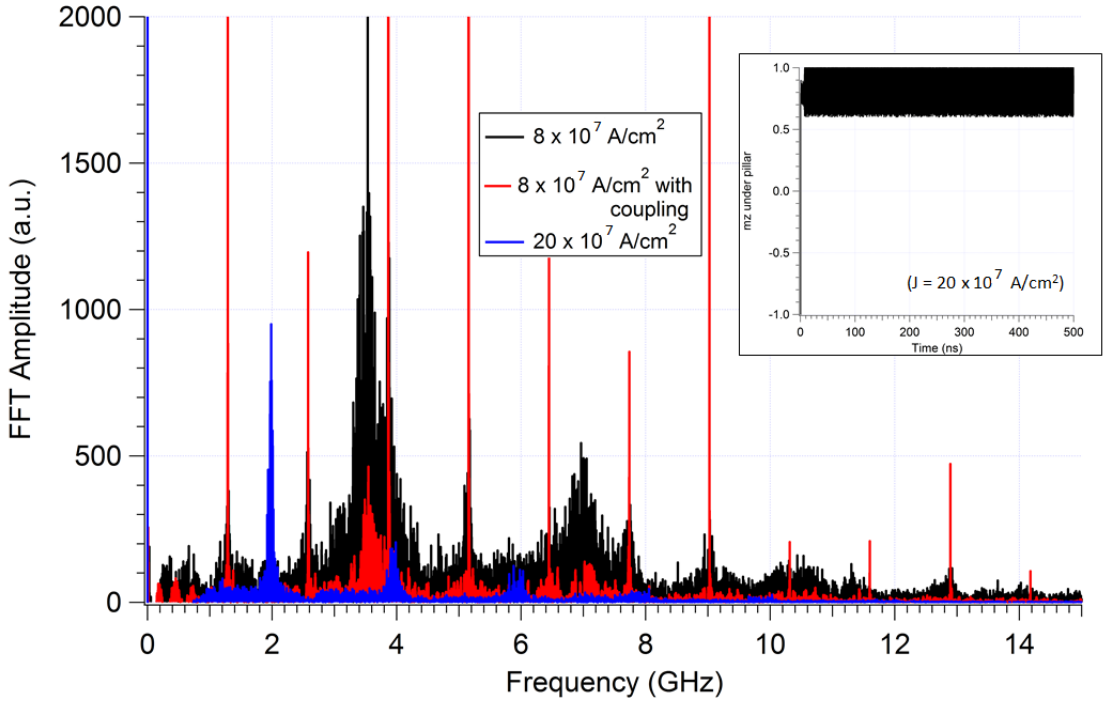

Figure 4.3: Mumax simulations showing dynamics at large currents. Coupling with the pillar (red) narrows the spectral peaks. Inset - m_z under the pillar for J = 20 x 10^7 A/cm^2. Note that the average moment is roughly parallel to the pillar.

mode is roughly 25% of the GMR, corresponding to a power of -41 dBm, which should be measurable using our setup (it should be able to resolve signal power down to ~ -110 dBm). In a GMR field or current scan, this mode should look like a small decrease in the resistance, since the average m_z is around -0.75.

When the current density is increased, the topological component starts to dominate, and its frequency decreases (Figure 4.3). The droplet's radius is on average larger, and the oscillation amplitude is much larger as well, giving a power of roughly -36 dBm. Then increasing the current density even further, the spectral peaks become sharper and the power decreases, consistent with predictions by Carpentieri, *et al.*. At large currents, the average z component of

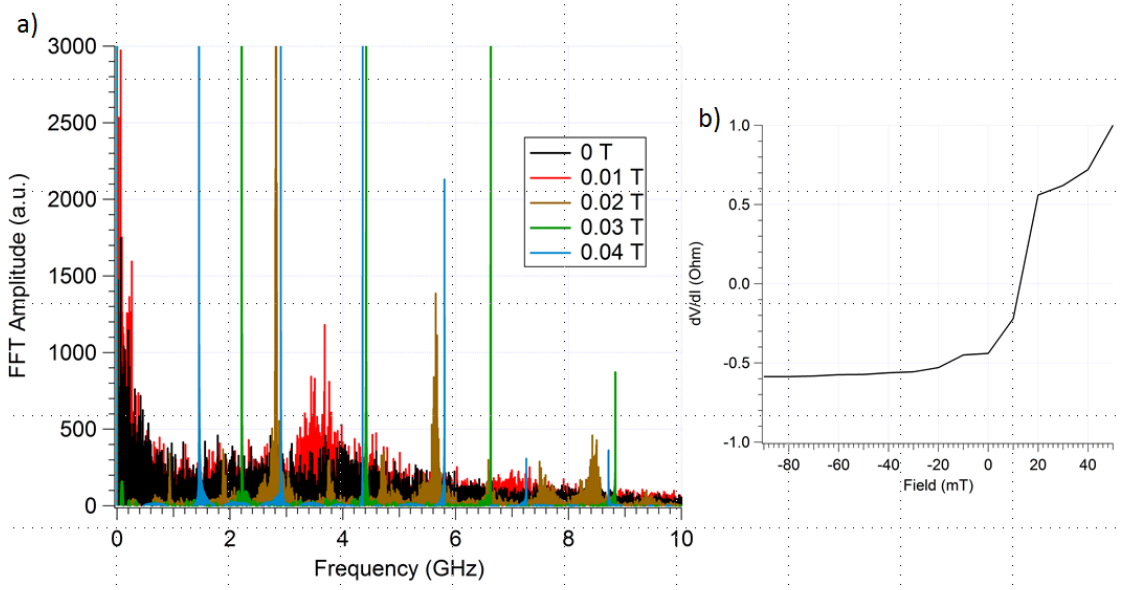

Figure 4.4: Mumax simulations showing dynamics for a current density of 5 x 10^7 A/cm^2 and an applied out of plane field. **(a)** The Fast Fourier Transform shows that the dynamics are enhanced by an applied out of plane field in the direction of the pillar. The dominant peak shifts to lower frequency as the field increases. **(b)** The average z component of the magnetization under the pillar shifts toward parallel alignment as the field increases, corresponding to a decrease in the GMR signal.

the moment under the pillar is partially parallel, which would correspond to an even larger decrease in the GMR signal.

As evidenced in our second project with the soft bilayer film, it is possible there may be some ferromagnetic coupling between the bilayer and the pillar. If we introduce a small coupling between the pillar and the bilayer by applying a nonzero field in the circular region while the rest of the film is at zero field, the peaks in the Fourier spectrum become narrower. The oscillation amplitude and dominant frequencies remain the same (Figure 4.3).

If we hold the current density constant and apply an out of plane field in

the direction of the pillar (+z), the spectral peaks narrow and shift to lower frequency, until, at a high enough field, the dynamics become single mode (Figure 4.4a). Looking at the magnetization, this corresponds to a shift from an instanton droplet to a topological droplet, which is an exciting result because it means that using an applied field, topological droplets are possible at a much lower current density and DMI than predicted by Carpentieri, *et al.* The applied field makes parallel alignment of the region under the pillar more favorable, while the extended layer is still reversed. As the field increases, the average z component of the magnetization under the pillar becomes increasingly parallel, which would correspond to a decrease in the GMR signal in our experiment (Figure 4.4b). The oscillation amplitude also increases to about 75% of the GMR for the topological droplet (~ -36 dBm). Increasing the field further, the entire film switches to the parallel orientation, at a field lower than the coercive field of the film. At negative fields (opposite to the pillar), we observe instanton droplets, with an amplitude that slowly decreases as the field magnitude increases. That makes sense, since a field in the direction of the pillar should enhance its effect, whereas a field in the opposite direction should weaken its effect. Lastly, I'd like to note that, since the coercive field in our simulation (~ 0.1 T) is much larger than observed experimentally (~ 20 mT), the field values required experimentally may be different, but we expect the qualitative behavior to agree. We observe topological droplets at fields less than 20 mT in our simulations, so this interesting behavior should be accessible experimentally. The large discrepancy in coercive field may be due to the fact that the simulations are done at T = 0 K.

4.3 Measurements

Samples were made with both Co/Pt and Co/Ni/Co/Pt fixed layers patterned into a 100 nm diameter pillar. Other pillar sizes were investigated, but smaller pillars had extremely low yield and the GMR was too weak for larger pillars. The samples with Co/Ni/Co/Pt proved to have more interesting results, probably due to the higher spin polarization, although these results were difficult to replicate. The following discussion will focus on devices with the recipe Ta(3)/Pt(5)/Co(0.6)/Cu(5)/[Co(0.3)/Ni(0.35)]x2/[Co(0.3)/Pt(1.0)]x5/Co(0.3)/Pt(10) (thicknesses in nm).

4.3.1 Giant Magnetoresistance Measurements

We first characterized our devices by measuring the four point differential resistance vs. out of plane applied field (see Chapter 3 for a detailed description of the setup). Measurements for a typical device are shown in Figure 4.5. Unless otherwise stated, all measurements covered in the following sections will be for this specific device. The GMR signal (Figure 4.5a) shows two switching events corresponding to the fixed and free layers. Magnetoresistance is usually 0.05-0.1% depending on multilayer recipe and device. The AHE signal confirms that the lower field switching corresponds to the Co/Pt bilayer. By comparing the GMR and AHE signals, we can isolate any behavior in the bilayer local to the pillar.

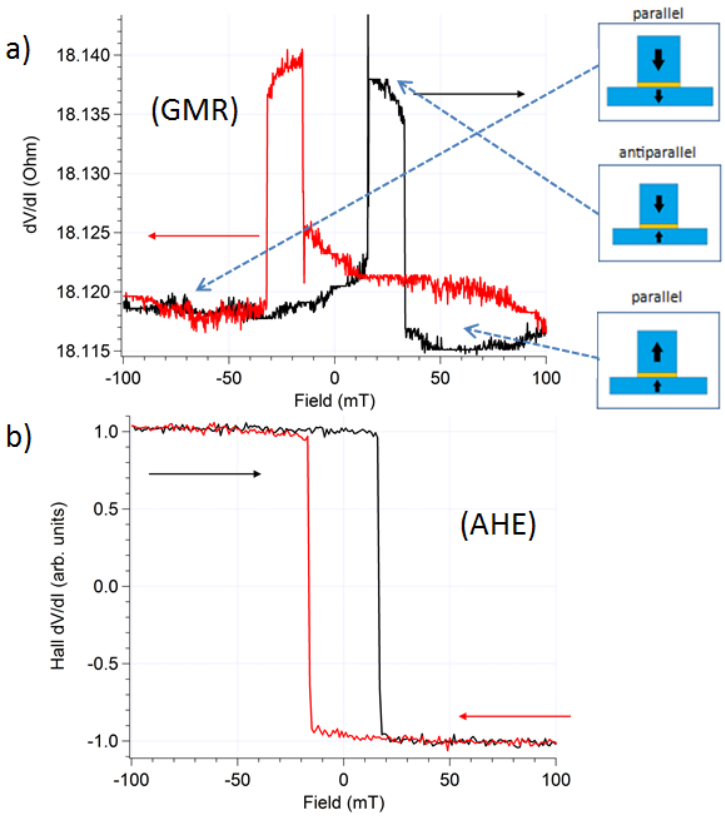

Figure 4.5: Measurements of the GMR **(a)** and AHE **(b)** for an example device. The GMR signal is used to characterize the pillar as well as isolate any effects in the bilayer local to the pillar. The AHE is used to monitor the behavior of the bulk bilayer.

4.3.2 Field Dependence at Constant DC Current

Next, we studied field scans as a function of constant DC current through the pillar. We observe a small dip in the resistance when the device is in the higher resistance antiparallel state, as shown in Figure 4.6. This feature appears for both positive and negative current, which indicates that it is likely thermally assisted (Figure 4.6a,b), and it doesn't appear in any of the AHE measurements, indicating that it is local to the pillar. However, there is also asymmetry with current sign, indicating that spin transfer torque plays a role, particularly at larger current values. As the DC current magnitude increases, the dip becomes

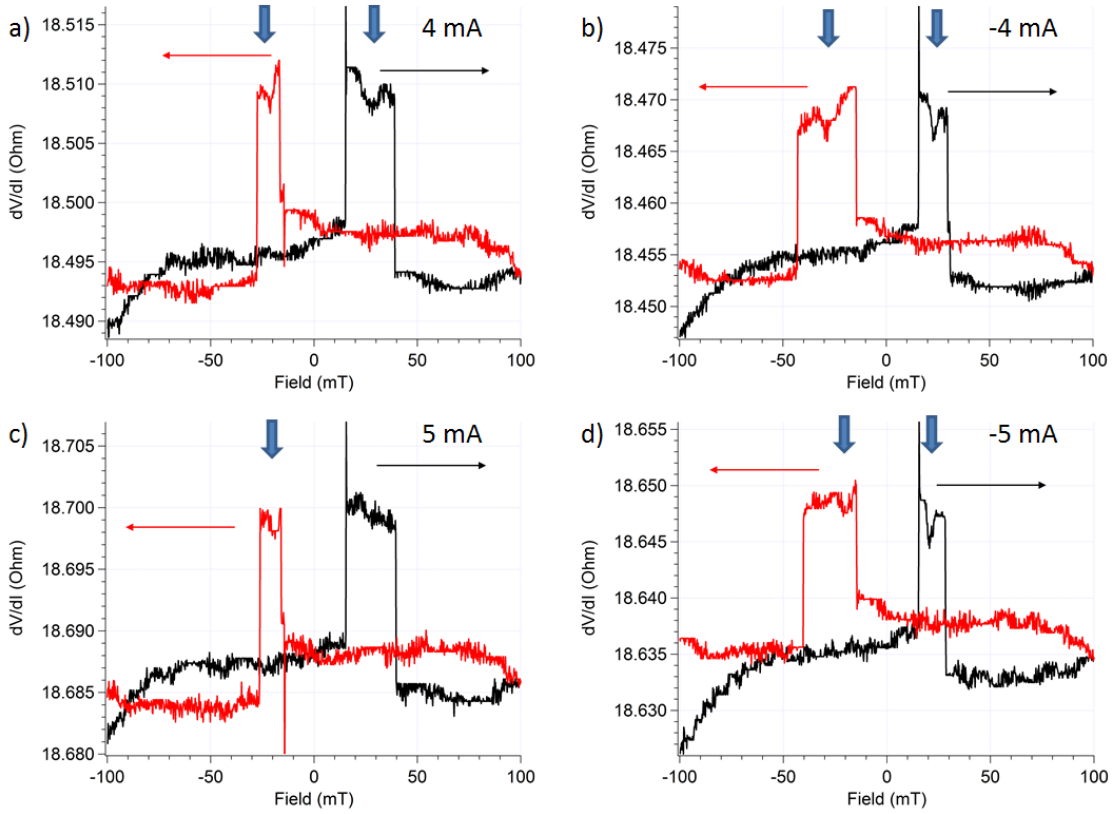

Figure 4.6: Pillar resistance vs. field measurements at fixed DC currents, 4 mA **(a)**, -4 mA **(b)**, 5 mA **(c)**, and -5 mA **(d)**. The resistance dip is marked by the large arrows.

more prominent at negative currents and goes away at positive current (Figure 4.6c,d). This makes sense, since a negative current will favor a lower resistance, partially parallel state, while a positive current will stabilize the antiparallel state.

When we look at the minor loop, holding the pillar fixed and switching the bilayer, it is apparent that the dip feature is non-hysteretic (Figure 4.7). This is a possible signature of dynamics, since a resonance is often reversible, whereas a change in the orientation of the magnetic is not. Minor loop scans allow for the device to be in the antiparallel state at lower fields. We thus see the feature

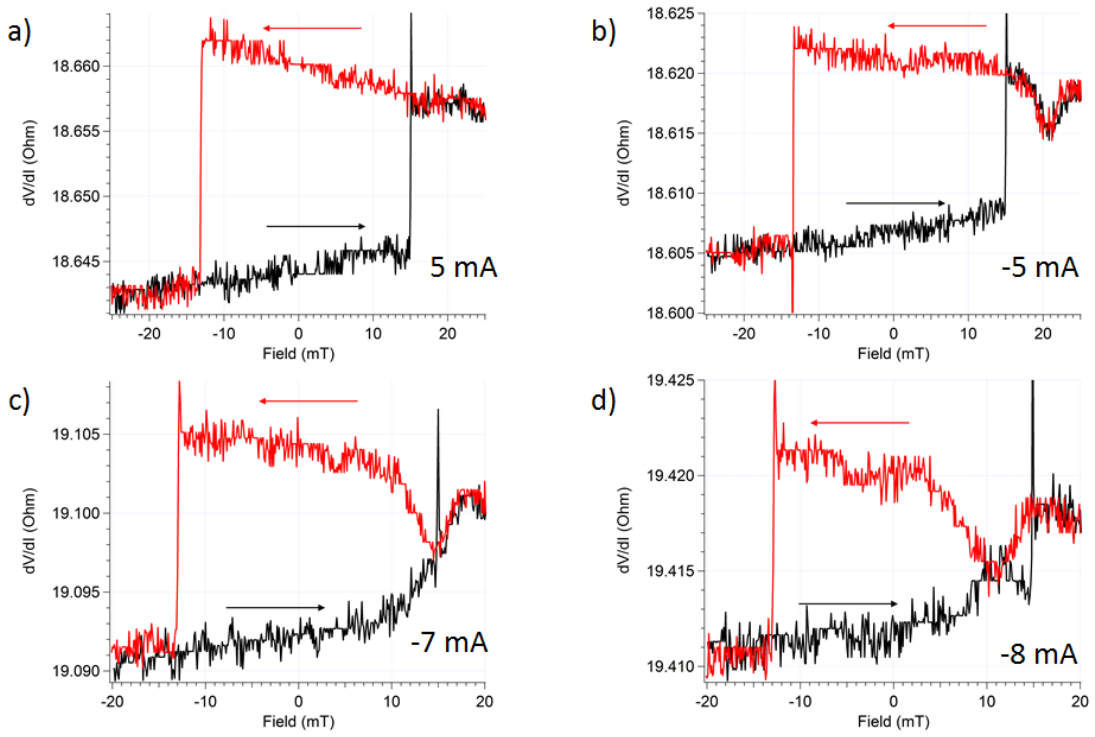

Figure 4.7: Minor loop field scans at fixed DC currents, 5 mA **(a)**, -5 mA **(b)**, -7 mA **(c)**, and -8 mA **(d)**.

move to lower fields as the negative current is increased (Figure 4.7b,c,d). The feature is not visible for positive currents above approximately 4 mA (Figure 4.7a,b).

The magnetic state of the pillar itself also seems to be affected by DC current. The switching field shifts either positive or negative, depending on the current sign. This result is puzzling, since we would expect if there were a torque on the pillar, its effect would be symmetric with field sign, but this is not the case. For the minor loop scans, we took this shift into consideration to ensure that the pillar is fixed at large currents. The bulk bilayer is not visibly affected by DC current.

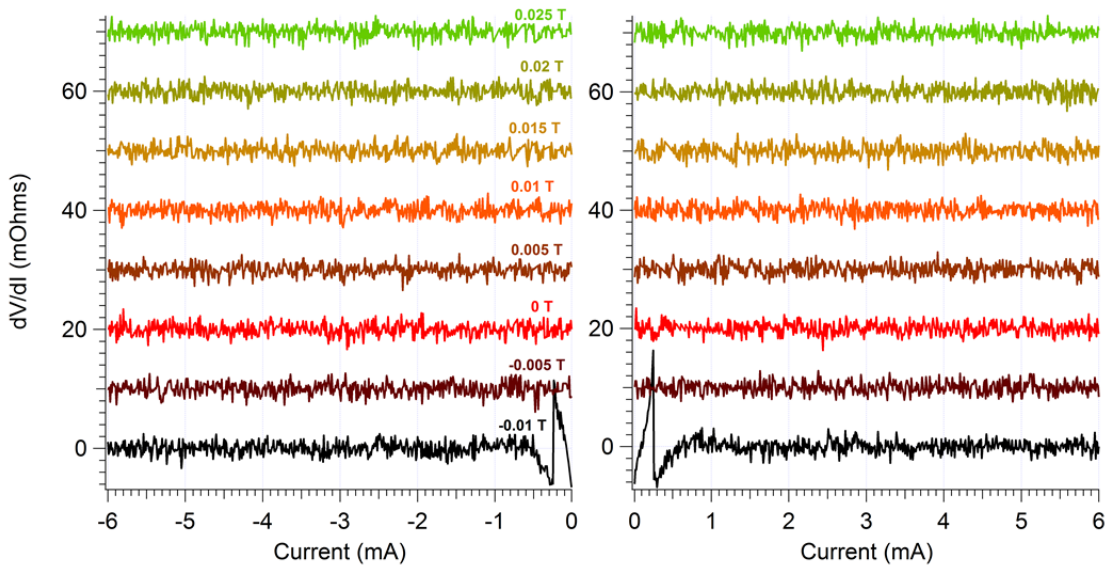

Figure 4.8: Background subtracted DC current scans showing thermal switching at -0.01 T. The device was initialized in the antiparallel state for each scan. No resistance dip feature is visible.

The measurements described above were done on devices made using an older fabrication recipe that had flaws which proved detrimental to pillar quality. More recently, we made higher quality devices from the same multilayer with the free layer patterned into different size leads, as shown in Figure 3.7. We saw the same dip feature in several of these devices with different bilayer dimensions, which confirms that the effect is local to the pillar, rather than a bulk effect.

4.3.3 DC Current Scans

We also performed current scans at fixed applied fields, initializing the device in the antiparallel state in between scans. However, we were unable to observe the resistance dip feature in these scans, and only thermal switching (symmetric

with current sign) was observed (Figure 4.8) at fields close to the switch down (-0.01 T). The large parabolic background from Joule heating made it difficult to resolve smaller features. It's possible a smooth feature could get subtracted out with the background.

4.3.4 Frequency Measurements

Since there was evidence that there may be dynamics at certain field and current ranges, we attempted to look for an emission signal using a spectrum analyzer. This setup was similar to the four point resistance measurements. A two prong probe was used to source current through the pillar, and a three prong (GSG) probe was connected to a wideband microwave amplifier (Minicircuits ZVA-183W+) and the spectrum analyzer. The amplifier has an average gain of 27 dB for frequencies up to 18 GHz, giving a maximum resolution of around -110 dBm. If the resistance dip is a resonance, it will have a power of between -80 and -90 dBm, but the amplifier would increase it to a more measurable magnitude of -53 to -63 dBm. We checked field and current values where the resistance dip was observed, however no peaks were visible in the frequency spectrum with or without the amplifier.

Since we do believe that there should be dynamics in our devices, the most likely reason for not observing anything is an unfortunate lack of foresight on our part. Initially, regular silicon wafers were chosen because they were readily available and relatively inexpensive. However, their resistivity is fairly low, and as a result, they have a very high loss. It is likely that almost all of the microwave signal was getting attenuated by the substrate. We tried reproducing our results

on high resistivity silicon, but we had trouble replicating the recipe because of changes in the sputter chamber. New Co/Pt samples were grown, but, as already mentioned, they were less interesting than the films with Co/Ni/Co/Pt.

4.3.5 Devices with Co/Pt Fixed Layer

Because Co/Ni/Co/Pt multilayers were difficult to fabricate in our sputter system, we also studied films with a Co/Pt polarizer. We were able to produce devices which had a pillar coercive field of 100 mT or higher. GMR was slightly larger than the Co/Ni/Co/Pt devices, around 0.08-0.15%. However, we did not observe any interesting features or effects, other than regular spin valve behavior and thermal switching, even at large DC currents. The spin polarization probably wasn't large enough to excite dynamics.

4.4 Discussion

In this project, we attempted to excite skyrmion dynamics in a hard Co/Pt bilayer using spin transfer torque from a nanopillar. In devices with a Co/Ni/Co/Pt fixed layer, we did observe an interesting effect that could be dynamics, but unfortunately we could not measure any frequency signal to prove it. While our simulations do predict dynamics that would correspond to a resistance decrease with applied field, other aspects of our signal do not agree with predictions. For example, it should not be possible to excite dynamics with both positive and negative current. However, because we don't know whether we have actually excited dynamics and we don't know the corresponding fre-

quencies, it is difficult to accurately model our devices.

While our results were inconclusive, they indicate that given more time and perhaps some improvements to our sputter deposition system, it may be possible to observe topologically nontrivial dynamics in such systems. A high spin polarization is necessary, so more work must be done to make the Co/Ni/Co/Pt recipe more uniform and repeatable. My work has hopefully provided the tools, techniques, and fabrication processes necessary for the next generation of students to continue the search for skyrmion dynamics in systems with interfacial DMI. Secondly, techniques developed in this project proved useful for my more successful work with softer Co/Pt bilayers, which will be the subject of the next chapter.

CHAPTER 5

DOMAIN MANIPULATION IN SOFT CO/PT BILAYERS

Previous experimental work has shown that soft magnetic films that host chiral stripe domains at zero field as a result of interfacial DMI can support isolated skyrmions at a nonzero out of plane field below saturation. As the field increases, the stripe domains pinch off and shrink into skyrmions. The question then arises of whether we can control the nucleation location of skyrmions in these films, and perhaps even write and delete them. A PMA nanopillar with a thin nonmagnetic spacer layer has two traits favorable to achieving these goals. First, interlayer coupling between the pillar and the film underneath may cause local alignment to be favored. Second, with the application of a current, the pillar can be used to locally exert a spin transfer torque on the film underneath. GMR can be used to monitor the state of the film local to the pillar, while the AHE tells us the status of the bulk film.

In this project, we use the spin valve device geometry discussed in the previous chapters to study the effects of a nanopillar on a soft Co/Pt bilayer.

5.1 Background

While still a relatively new concept, the possibility of creating skyrmions using a local spin transfer torque has been studied a few times before. The idea for this project was sparked partially by the work of Romming, *et al.*, discussed in Section 1.3.1, where an SP-STM tip was used to write and delete skyrmions [32]. The tip and sample essentially form a tunnel junction, with the tip being the

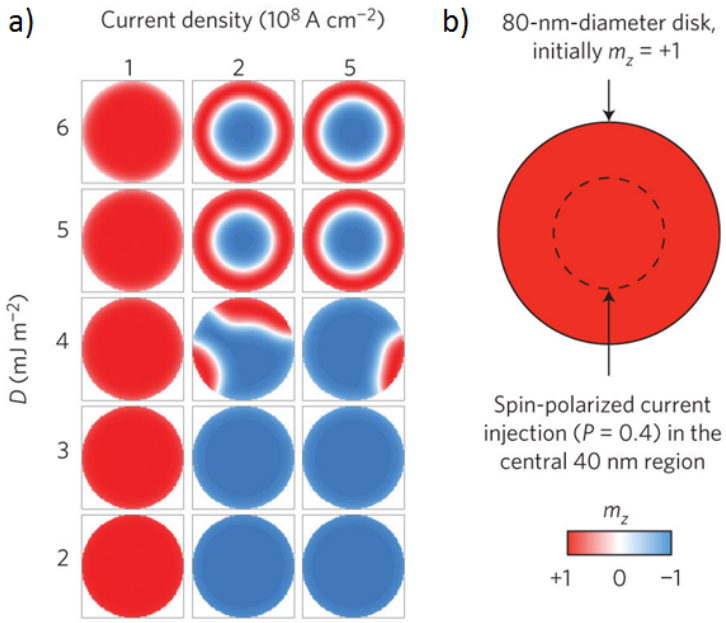

Figure 5.1: Micromagnetic simulations showing skyrmion creation using spin transfer torque. **(a)** Magnetization state after current with polarization 0.4 was pulsed for 2 ns for different values of DMI and current density. The initial state was in the $+z$ direction (red). **(b)** Device geometry. Figure from [62].

polarizer or fixed layer. It makes sense, then, that it should be possible to create skyrmions using the device equivalent of that experiment, i.e. nanopatterned tunnel junctions or spin valves. Spin valves were chosen for this project due to their relative ease in fabrication compared to a perpendicular tunnel junction, and, while the spin polarization and magnetoresistance tend to be significantly larger in MTJs, it would be difficult to get a high enough current density because of the large resistance of the barrier.

Micromagnetic simulations by Sampaio, *et al.* further explored the feasibility of this idea [62]. Using measured parameters for 0.4 nm cobalt on platinum, they simulated an 80 nm diameter disk with spin polarized current injected into a 40 nm circular region in the center (Figure 5.1b). They showed for certain current

densities and DMI values, a skyrmion could be created in the disk (Figure 5.1a). The current density and DMI required could be reduced by applying a small perpendicular field or decreasing the PMA. Similar simulations were done by Kang, *et al.* on a configuration consisting of a 20 nm pillar on top of an 80 nm square of Co/Pt [63]. They found that a slightly higher current density was required for skyrmion creation, but this is likely due to the smaller pillar size. Our Co/Pt films are much softer than the ones simulated, and our extended bulk geometry might make it more difficult to switch the entire film, perhaps making skyrmions favorable over switching the entire bilayer.

A second mechanism that wasn't originally considered at the start of this project is coupling between the free and fixed layers. Exchange coupling between two ferromagnetic layers separated by a thin nonmagnetic spacer has been studied in detail in conventional spin valves and MTJs [64]. Coupling can be either ferromagnetic or antiferromagnetic, depending on the thickness of the spacer and the specific materials used, and usually oscillates between the two as the spacer thickness increases. This was one of the main predictions of the Ruderman-Kittel-Kasuya-Yosida (RKKY) theory, and research in this area lead to the discovery of GMR [40] [41]. IEC will usually cause a shift of the minor loop, which can be used to determine the magnitude and type of coupling (ferromagnetic or antiferromagnetic).

Magnetostatic coupling is also common in spin valve multilayers. The local dipole field of the fixed layer can affect the free layer. A second effect is the so-called "orange peel" coupling, first described by Néel [65]. This type of coupling results from correlated roughness of the two spacer-ferromagnet interfaces, and it decays exponentially with spacer thickness. Orange peel coupling has been

shown to be present in sputtered PMA Co/Pt spin valves and is ferromagnetic for weak anisotropy, but antiferromagnetic for strong anisotropy, assuming the roughness of both interfaces is in-phase [66].

Interlayer coupling has been shown experimentally to affect chiral films such that skyrmions are favored at lower fields [28]. Furthermore, if the second ferromagnetic film is patterned into an array of nanopillars, an artificial skyrmion lattice can be created [29]. We expect the pillar in our device geometry to have a similar effect.

5.2 Mumax3 Simulations

Using the same techniques discussed in the previous chapter (Section 4.2), we simulated the effects of coupling with the pillar and applying a spin polarized current in soft Co/Pt films.

5.2.1 Estimating the DMI

From magnetometry data, we calculated the saturation magnetization for Co(1.65)/Pt(10) films to be $M_s = 1.3 \times 10^6$ A/m, which is close to the bulk value for Co, 1.42 $\times 10^6$ A/m and comparable to values for similar films in the literature [43] [44]. Calculating the first order uniaxial anisotropy constant, K_1 for a perpendicular film is nontrivial, especially if stripe domains are involved. A common way to calculate K_1 is to find the anisotropy field, that is the field at which the film can be saturated perpendicular to the anisotropy direction, us-

ing magnetometry. The anisotropy field can be written as,

$$H_K = \frac{2(K_1 - \frac{1}{2}\mu_0 M_s^2)}{\mu_0 M_s} = \frac{2K_{eff}}{\mu_0 M_s} \tag{5.1}$$

where M_s is the saturation magnetization and K_{eff} is the effective anisotropy. Solving for K_1 we get,

$$K_1 = \frac{1}{2}\mu_0(H_K M_s + M_s^2). \tag{5.2}$$

The anisotropy field is approximately 1000 Oe, which gives $K_1 \approx 1.1 \times 10^6$ J/m^3. However, this value is too large. Simulations at a variety of DMI values demonstrated that the film would have a uniform magnetization at zero field after saturation, whereas for the films in our experiment, stripe domains are always present in the absence of applied field. There are other ways to estimate K_1. For example, the effective anisotropy can be calculated from the area between the parallel and perpendicular hysteresis curves [67], giving $K_1 \approx 1.2 \times 10^6$ J/m^3. However, both of these estimates are too large to give stripe domains in our simulations.

The reason for this discrepancy is that the above theory assumes that the film is uniformly magnetized, when in fact our films have stripes at zero field. It has been shown that the presence of stripe domains reduces the magnetostatic energy contribution, which is normally $\frac{1}{2}\mu_0 M_s^2$ for a uniform film [68] [69]. This means that,

$$K_1 < K_{eff} + \frac{1}{2}\alpha(t)\mu_0 M_s^2. \tag{5.3}$$

Since my estimate of K_{eff} is still valid, that gives an upper bound for the anisotropy constant of $K_1 \approx 1.2 \times 10^6$ J/m^3. The change in the magnetostatic energy from the existence of domains is nontrivial and has a complicated dependence on domain size and film thickness [68], so instead I chose to test a range of reasonable values for the DMI and K_1. I looked for a combination that

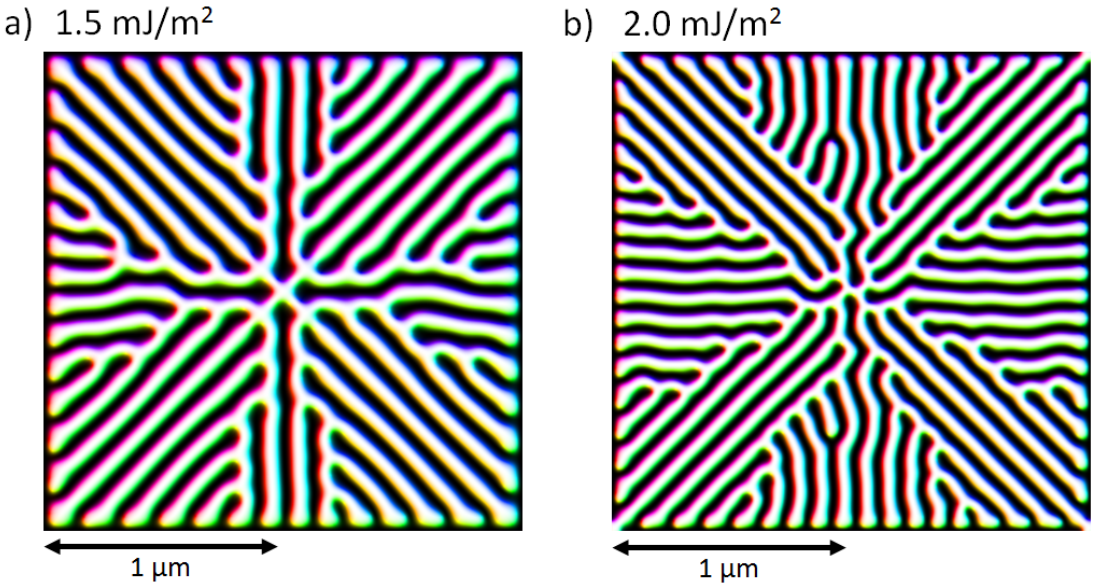

Figure 5.2: Mumax3 simulations at T = 0 K for films with $K_1 = 1.00 \times 10^6$ J/m^3 and $M_s = 1.3 \times 10^6$ A/m for different values of interfacial DMI, **(a)** 1.5 mJ/m^2 and **(b)** 2.0 mJ/m^2. As expected, domain size decreases with increasing DMI. Symmetry is due to boundary conditions.

gives a domain size close to what was experimentally observed (~ 100 nm using MFM).

Simulations of the domain structure after out of plane saturation reveal that stripes exist only for a very narrow range of values for the anisotropy constant, $K_1 = 1.00 \pm 0.05 \times 10^6$ J/m^3 (Figure 5.2). For larger K_1, the film is uniform, and smaller K_1 results in an in plane domain structure. The range of DMI values that support stripes is much larger. The widest stripes are at $D_{ind} = 1.5$ mJ/m^2. For DMI constants less than this, we get in plane solutions, regardless of K_1, and, as expected, as the DMI increases, the stripes get smaller. $D_{ind} = 1.5$ mJ/m^2 is in agreement with previously measured and calculated values for the Co/Pt interface [31] [70].

The largest simulated stripes are still smaller than what was observed in MFM (compare Figure 5.2a to Figure 2.1f). Since we have observed that the MFM tip moves domains around and the tip has a finite radius of 25-35 nm, the stripes are likely broadened in the resulting image. A better measure of the domain width would be a noninvasive technique such as Lorentz TEM. Secondly, the simulations are done at T=0 K, and the domains could potentially be much larger at room temperature [71]. Another issue is that the simulations do not take into consideration factors such as grain size and interfacial roughness.

5.2.2 Device Simulations

Next, we simulate the hysteresis loop for devices with a coupling field in the pillar region. The pillar is slightly off center to eliminate effects from stripe domain symmetry as in Figure 5.2, and for all simulations discussed here, the pillar magnetization is fixed in the $+z$ direction. With no applied current, the moment vs field hysteresis loop of the film under the pillar shifts toward negative fields, making parallel alignment more favorable at low fields, whereas the bulk film is unaffected (Figure 5.3a,b). Under the pillar, the transition from parallel to antiparallel is gradual, and above the apparent coercive field of the bulk, this corresponds to a Néel skyrmion that shrinks in diameter as the magnitude of the field increases (Figure 5.3c). The skyrmion persists for slightly longer than skyrmions occurring in the rest of the film. The switch from antiparallel to parallel is much sharper and occurs roughly where stripe domains start to form in the film. The sharp transition is followed by a gradual slope to full parallel alignment, as the stripe domains expand with increasing field. If the coupling field is less than the coercive field, we do not see a skyrmion persisting under

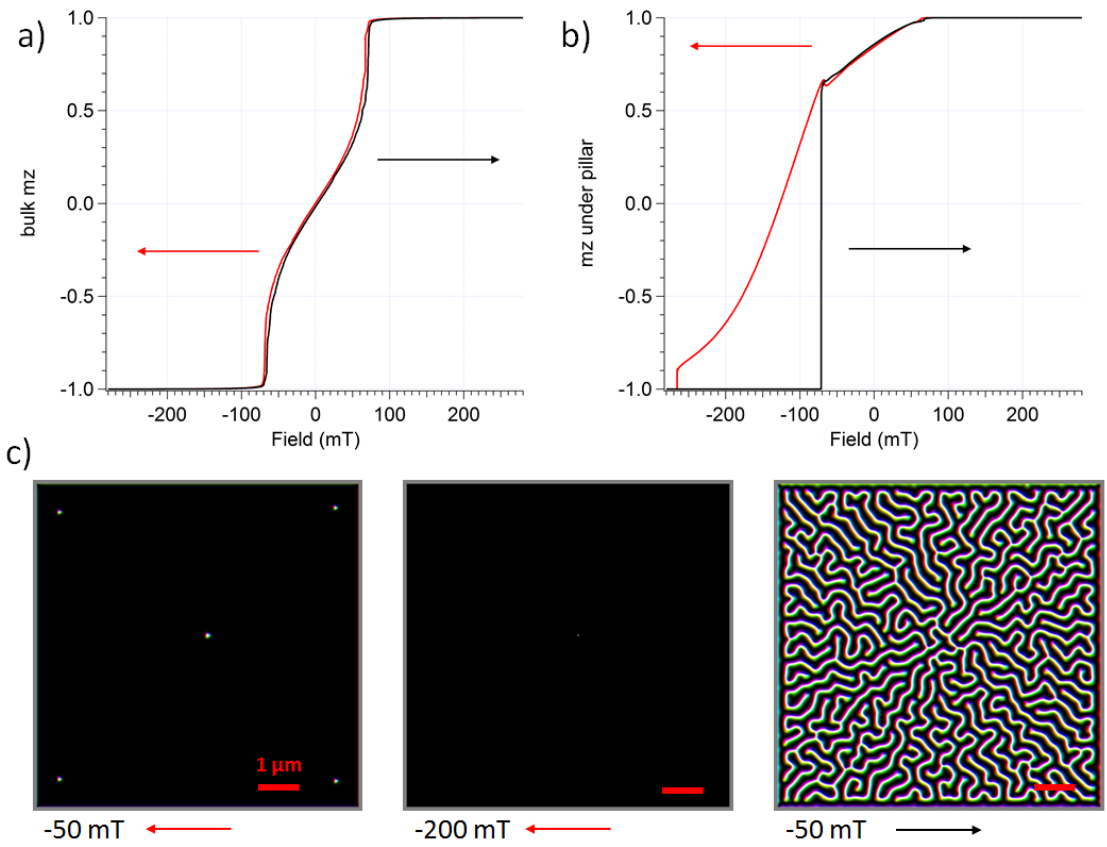

Figure 5.3: Simulations of a nanopillar device with no applied current through the pillar. The pillar has a magnetization in the $+z$ direction, is 100 nm in diameter, and is slightly off center, with 50 mT ferromagnetic coupling to the film underneath. The **(a)** bulk film and **(b)** film under the pillar behave independently of each other. **(c)** Snapshots of the film domain structure at various points in the hysteresis curve. White corresponds to moment oriented in the $+z$ direction, and the arrows indicate the direction of field change. A Néel skyrmion is immediately under the pillar for decreasing fields.

the pillar with decreasing field. As we will show in the next section, these simulations qualitatively agree with our observations.

However, unlike our observations, when we apply a current through the pillar in our simulations, it only affects the switch from parallel to antiparallel.

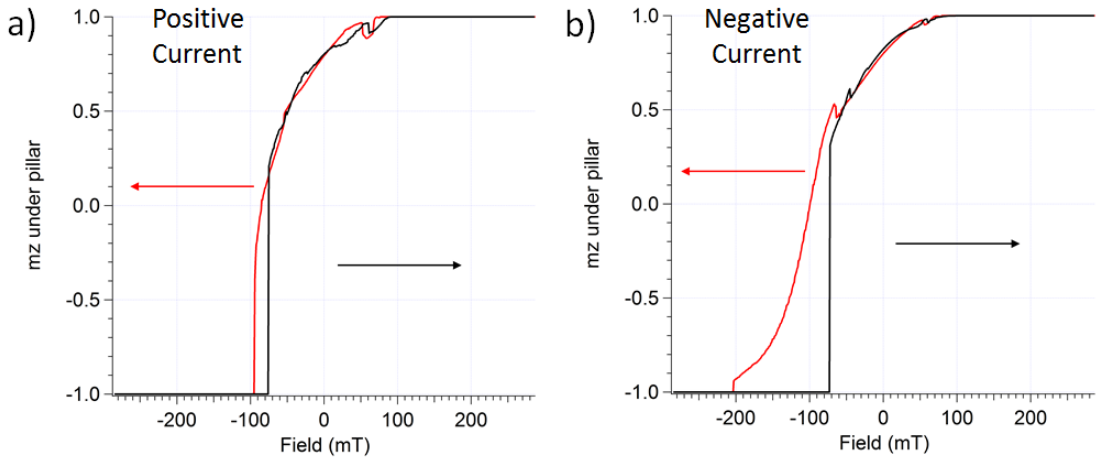

Figure 5.4: Simulations of a nanopillar device with $J = \pm 5 \times 10^7$ A/cm^2 and a coupling field of 30 mT. **(a)** Positive current prevents a Néel skyrmion from forming under the pillar, while **(b)** negative current stabilizes the skyrmion. The switch from antiparallel to parallel and the behavior of the bulk film are unaffected.

When electrons flow from the bilayer to the pillar (positive current), antiparallel alignment is favored, and a skyrmion does not persist under the pillar (Figure 5.4a). On the other hand, a negative current stabilizes the skyrmion (Figure 5.4b), which is parallel to the pillar. Our measurements show the opposite - the switch from antiparallel to parallel is strongly affected by current, while the switch to the higher resistance state is not. Further work is required to determine why we are not accurately modeling the behavior of our devices in this case. The most likely reason is that simulations do not take thermal effects into account, and we've shown that thermally assisted switching is an important effect in our devices. Secondly, these simulations are done at T = 0 K, while our measurements are done at room temperature.

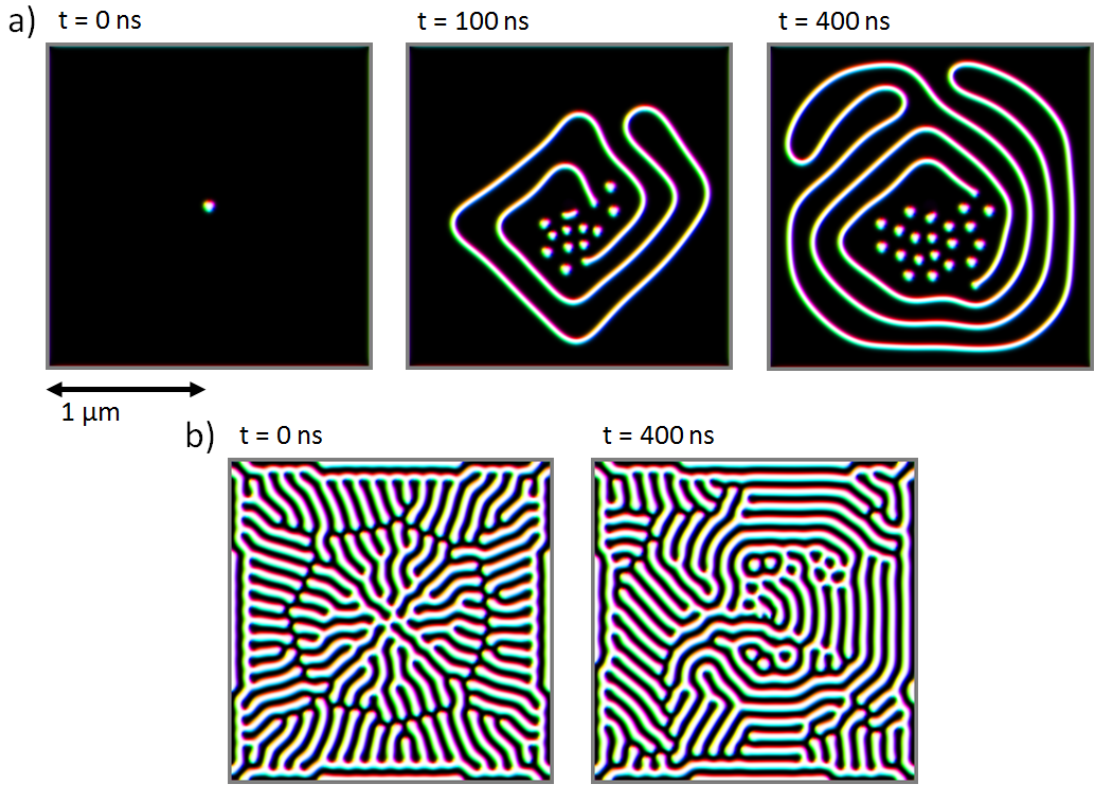

Figure 5.5: Simulations of devices with an in plane polarizer at **(a)** -0.1 T and **(b)** 0 T. Here, D_{ind} = 2.0 mJ/m^2 and $J = 1.5 \times 10^7$ A/cm^2. The 100 nm pillar is oriented in the $+x$ direction in the center of the film. Skyrmion creation is observed at fields for which domains exist in the vicinity of the pillar.

5.2.3 In Plane Polarizer

We also simulated devices with an in-plane polarizer (Figure 5.5). With the application of moderate current densities, out of plane domains under the pillar are pushed away by the in plane polarized current and sometimes pinch off to form skyrmions. This effect occurs at any field where the film has domains in the vicinity of the pillar, since skyrmions only seem to form from existing domains. This is an interesting idea for an experiment and may prove to be an easy way to create clusters of skyrmions using our device geometry. However,

the GMR signal associated with skyrmion creation using this method is erratic and does not have a distinct signature, which means imaging is necessary.

5.3 Measurements

Spin valve devices were fabricated with a Co/Pt polarizer patterned into a 100 nm diameter pillar. The free layer is a soft PMA Co(1.65)/Pt(10) film that exhibits stripe domains at zero field before and after saturation (similar to the film in Figure 2.1c,f). The complete recipe, starting at the bottom, is Ta(3)/Pt(10)/Co(1.65)/Cu(5)/[Co(0.4)/Pt(1.6)]$_8$/Co(0.4)/Pt(10), with thicknesses in nanometers. Magnetometry data for the bulk film before fabrication is shown in Figure 5.6a. Three different Hall cross widths were used for the free layer - 2 μm, 20 μm, and 100 μm. Any effects in the vicinity of the pillar should not be affected by the width of the Hall cross.

5.3.1 Giant Magnetoresistance

Pillar quality was characterized using four-point GMR measurements as previously described (Figure 5.6b). Because of film nonuniformities across the wafer (see Section 2.1.4 and Figure 2.3d), we noticed significant device variation depending on its location on the wafer. The best devices with the most interesting properties were in the center of the wafer. This is where the cobalt is the thickest in the bilayer, meaning it has stripe domains at low fields, and the multilayer recipe is as expected. Close to the edge of the wafer, the bilayer is much harder, has a sharper switch, and does not seem to be affected by the pillar. For most

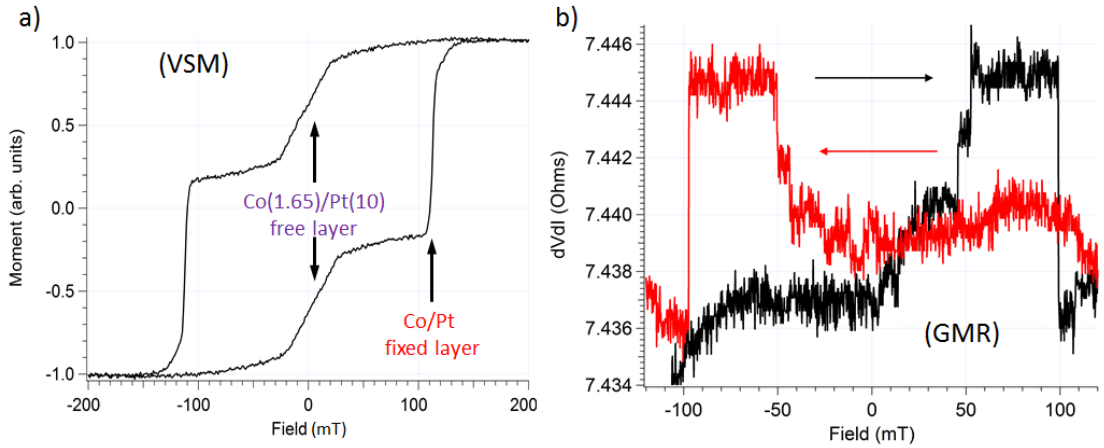

Figure 5.6: **(a)** Magnetometry data for the bulk film before device fabrication. Sample taken from the center of the wafer. **(b)** Typical GMR data for a device (2 μm Hall cross width) with a high quality pillar. Note that the coercive fields have not changed much from the bulk film.

of this discussion, unless otherwise noted, we will focus on devices from the center of the wafer.

The GMR is roughly the same, regardless of location on the wafer. Using the four point resistance, we get a GMR of 0.09-0.15%. Since the pillar dimensions and recipe are the same for all devices, the variation is due to differences in the series resistance, and the true pillar GMR is much larger. This is supported by the fact that ΔR is not affected by device resistance. Using known resistivity values, the pillar resistance should be around 0.3 Ω. This gives a GMR of approximately 3%.

The AHE signal for the same device as in Figure 5.6 confirms that the lower field switching event corresponds to the bilayer (Figure 5.7a). However, interestingly, the bilayer switching in the GMR signal occurs at a higher field. This effect becomes even more striking when we look at the minor loop (Figure 5.7b).

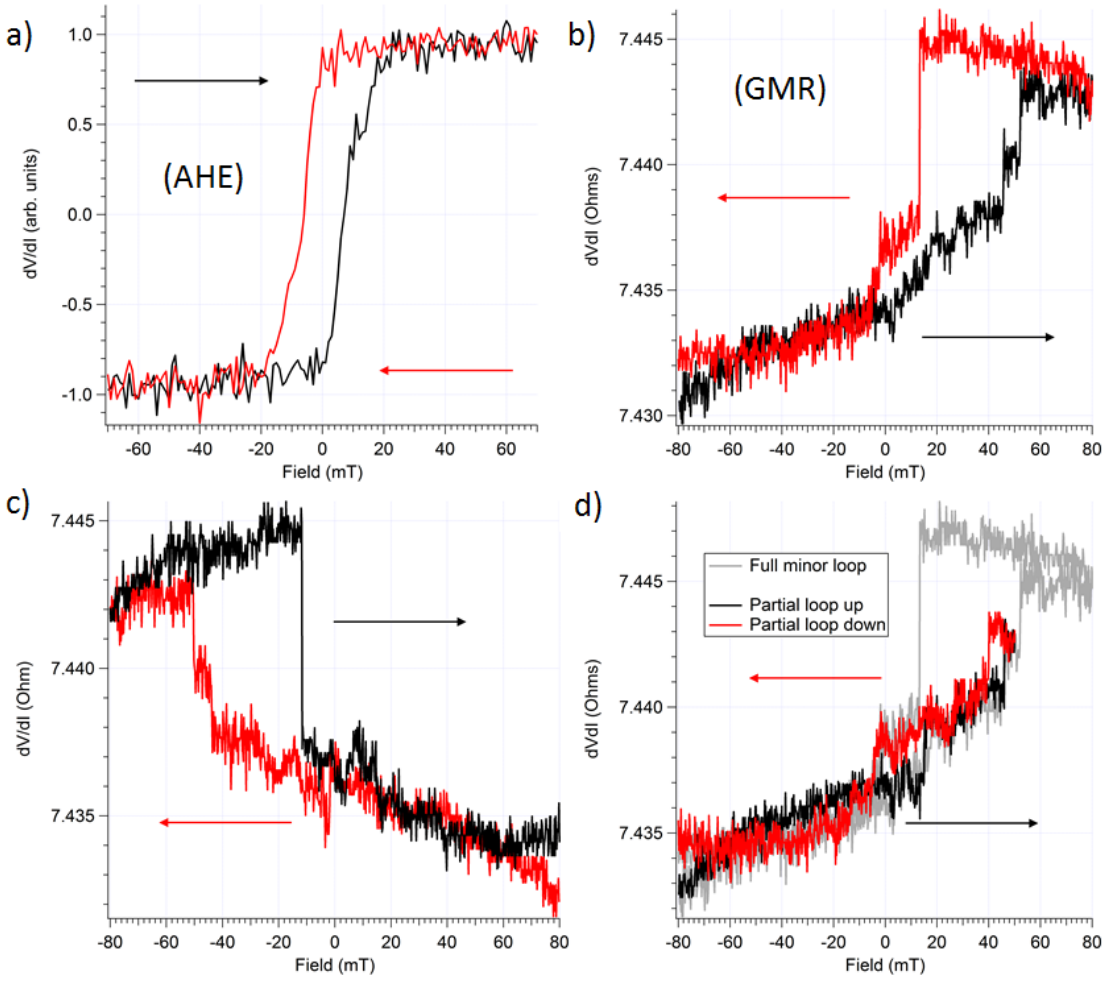

Figure 5.7: **(a)** AHE data showing switching of the bulk Co/Pt bilayer. **(b)** The GMR minor loop with the fixed layer saturated in negative field direction shows that the bilayer under the pillar is switching at a much higher field than the bulk. **(c)** GMR minor loop with the fixed layer saturated in the positive field direction. **(d)** A smaller field loop shows that the slope is repeatable and reversible. The full loop (grey) is offset by 0.002 Ω.

The hysteresis curve, rather than being centered around zero field, is shifted, making the lower resistance state more favorable at lower fields. The most likely cause of this shift is ferromagnetic coupling with the pillar. We confirm this by measuring the reverse minor loop (Figure 5.7c). Rather than holding the fixed

layer in the negative field direction, we keep it in the positive field direction. When this is done, the hysteresis loop is offset toward negative fields, again making parallel alignment more favorable at low fields.

If we do a smaller field loop which saturates the bulk film but not the region under the pillar, the GMR signal becomes nonhysteretic, but has a repeatable slope (Figure 5.7d). The slope in the resistance in this case is a real effect and not related to probe motion, which is hysteretic. This indicates that the size of the domain under the pillar can be controlled with field. More interestingly, however, the AHE signal for the smaller loop still looks the same as Figure 5.7a, meaning the bulk film is now oriented opposite to the region under the pillar. Using the external field, we can create a domain under the pillar and control its size.

5.3.2 Field Dependence at Constant Current

When we apply a constant DC current through the pillar, we see a second effect in addition to the offset from interlayer coupling. Looking at the GMR minor loop, the switch from antiparallel to parallel is shifted depending on the sign of the DC current (Figure 5.8). Switching that is asymmetric with current sign is usually a signature of spin transfer torque. Positive current corresponds to electrons flowing from the bilayer to the pillar, meaning antiparallel alignment should be more favorable. Negative current favors parallel alignment. Spin transfer torque seems to only affect the switch from antiparallel to parallel. While we haven't determined the exact reason, one possibility is that coupling with the pillar might be a much stronger effect than the spin transfer torque.

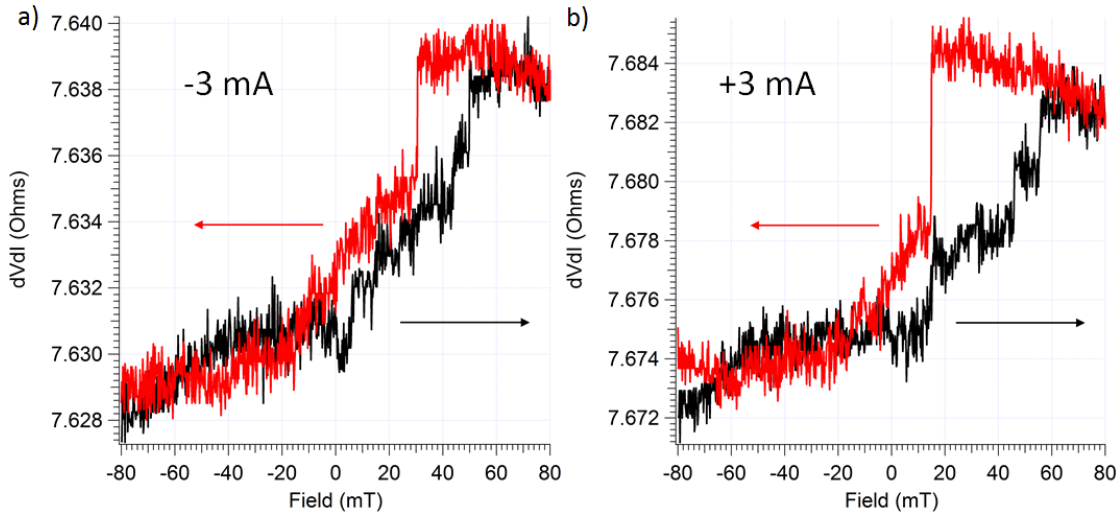

Figure 5.8: GMR minor loop data at a constant DC current of **(a)** -3 mA and **(b)** +3 mA. The difference in the antiparallel to parallel switching field is caused by spin transfer torque.

Switching to the antiparallel state would require counteracting the interlayer coupling, whereas switching to parallel is assisted by coupling. One way to test this hypothesis would be to use a fixed layer with higher spin polarization, which would increase the magnitude of spin transfer torque relative to the coupling.

The AHE signal looks roughly the same, regardless of DC current. The bulk bilayer switching field does not change, indicating that the effects of spin transfer torque are local to the pillar, as expected. This also indicates that there are combinations of field and current for which the region under the pillar may be reversed with respect to the bulk. Such an isolated domain could very likely be a skyrmion. As was the case with GMR measurements in the absence of DC current, the slope in the parallel state is repeatable and nonhysteretic for small field loops (similar to Figure 5.7d), so an isolated domain can again be created by looping the field.

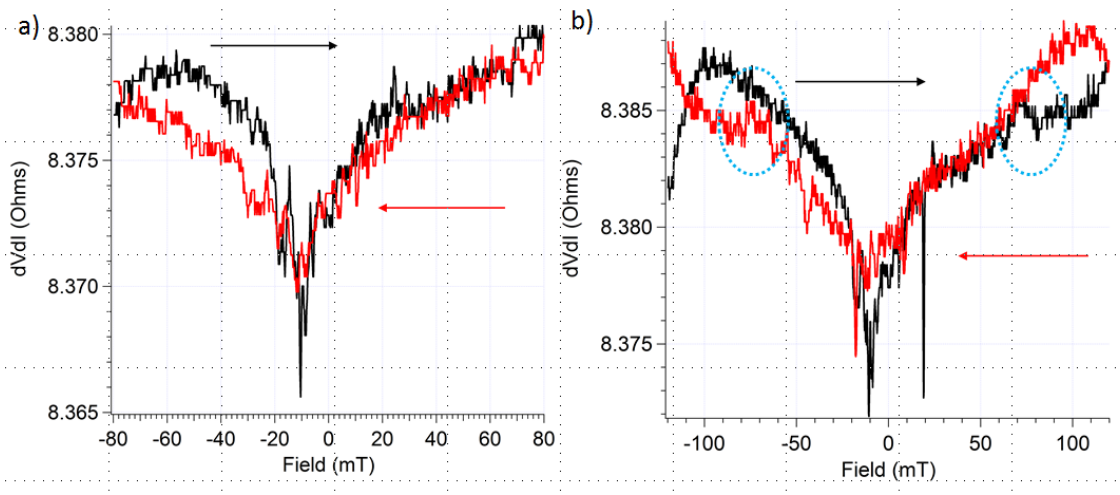

Figure 5.9: GMR **(a)** minor and **(b)** major loops with an applied DC current of 6.5 mA. The behavior of the bilayer under the pillar becomes mostly non-hysteretic and the magnitude of the pillar switching (marked by the two circles in **b**) is greatly reduced.

At large current magnitudes, typically between ± 5-7 mA, depending on the device, the well-defined switching behavior disappears. The minor loop scan becomes almost flat with a non-hysteretic decrease in the center (Figure 5.9a). Looking at the major loop, we can see that the pillar switching is still hysteretic, but the GMR is greatly reduced (Figure 5.9b). For the example in the figure, the switching magnitude is about 20% of what it is at zero DC current. Another interesting point is that this behavior occurs at both positive and negative current. Because we've already observed that the parallel state is thermally favorable as a result of coupling with the pillar, perhaps at large current magnitudes the region under the pillar is partially parallel for the entire scan. Alternatively, there may be some sort of dynamics in the bilayer or the pillar, but we were unable to observe an emission signal with a spectrum analyzer. The devices studied in this project were fabricated on high resistivity silicon, but it's still possible the signal is too small, since ΔR is on the order of 5 mΩ. Whether we have dynamics

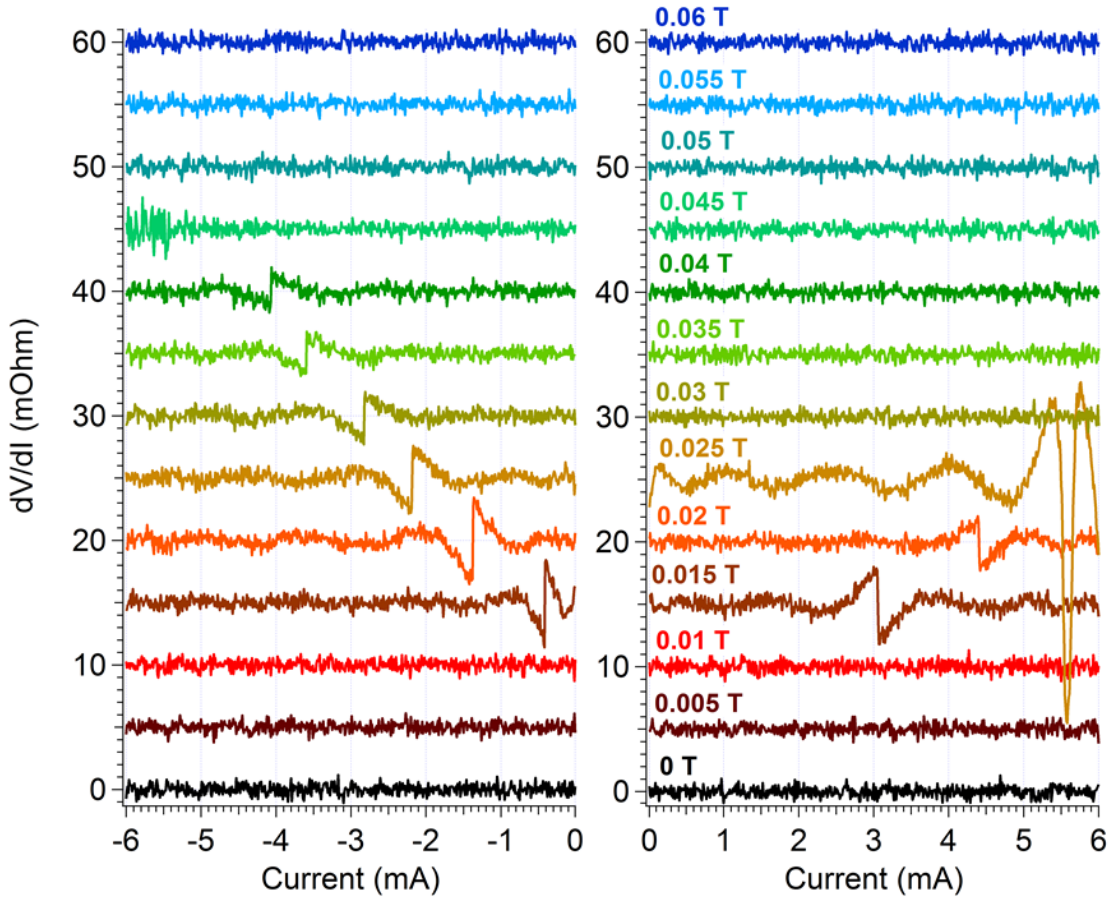

Figure 5.10: DC current scans (background subtracted) at constant field. The bilayer is initialized to be antiparallel to the pillar between scans. For negative currents, switching due to spin transfer torque is observed. Higher current magnitudes are required to switch at positive current, and this switching is likely thermal. The large dip at positive currents is repeatable.

or some sort of stable domain under the pillar requires further investigation.

5.3.3 DC Current Dependence

DC current scans were performed at constant field. Two sets of measurements were done, with the bilayer initialized in either the parallel or antiparallel state.

When the bilayer under the pillar is initially in the parallel state, we only see occasional thermal switching of the pillar or bilayer at fields close to its coercive field. However, when the bilayer under the pillar is initially in the antiparallel state, we observe spin transfer torque induced switching that is not symmetric with current sign (Figure 5.10). These switching events do not appear in the AHE signal. Again, negative current has a strong preference for the parallel configuration, so we see the bilayer switching down at lower fields than for positive current. Switching at positive currents is likely thermal in nature. None of these switching events can be reversed with current alone. That is, hysteretic switching with current is not observed. This is in agreement with our previous observations that it is easier to switch from the antiparallel to the parallel state using spin transfer torque.

The large dip in Figure 5.10 is repeatable for this particular device and also appears in field scans around that particular current (~ 5.5 mA). We've observed similar features at large current magnitudes in other devices, but the specifics tend to vary. These features were investigated with a spectrum analyzer, but no emission signal was observed.

5.3.4 Phase Diagram

Putting together all the data from the previous two sections, we can make a DC current vs field phase diagram (Figure 5.11). The dotted lines indicate where the bulk bilayer is done switching up (black) or down (red), according to the AHE. This switch is gradual and starts around zero field.

Now, let's focus on the GMR data, marked by the solid lines in the phase

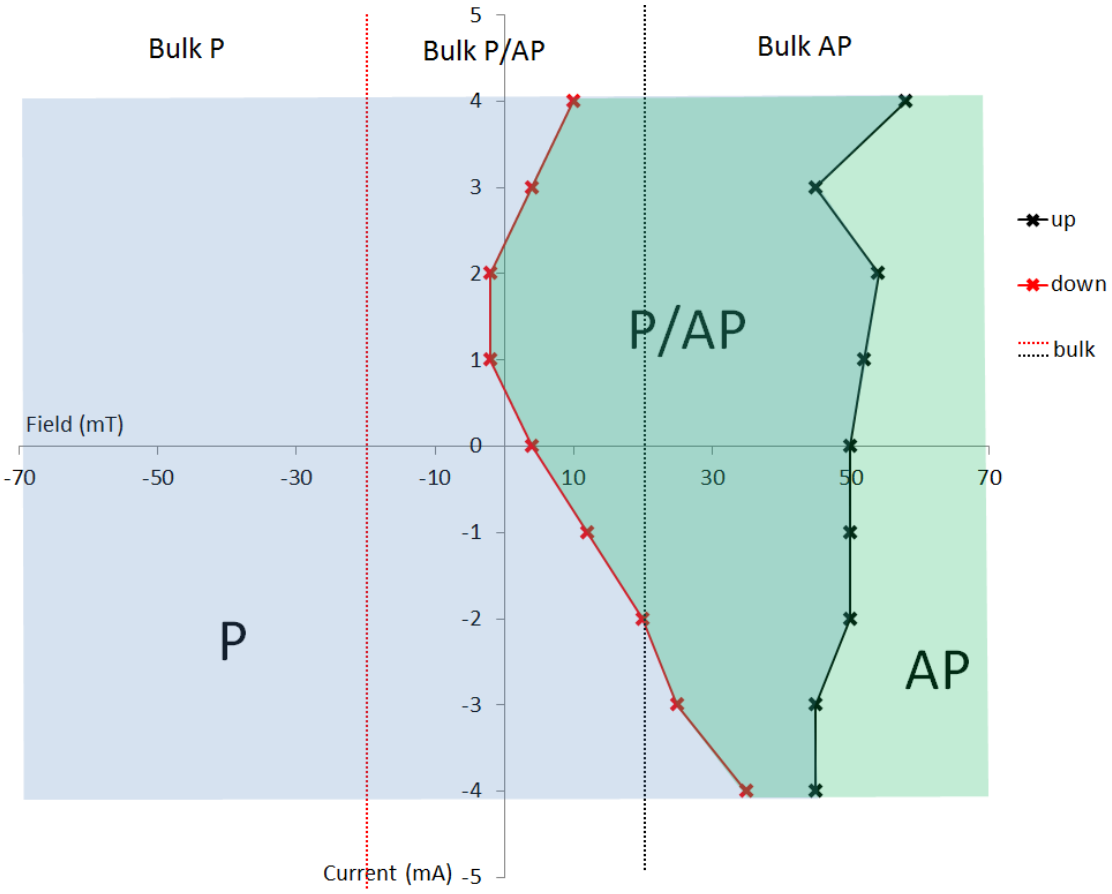

Figure 5.11: DC current vs field phase diagram for example device (2 μm wide Hall cross).

diagram. The bilayer under the pillar also switches gradually to the antiparallel state (see Figure 5.8, for example). Because the signal is small, it is difficult to tell exactly what field this transition starts at, but is around zero field for all currents shown. The solid black line in Figure 5.11 marks where the bilayer under the pillar is finished switching up, and this seems to be mostly unaffected by applied current, which makes sense if our hypothesis about coupling with the pillar being the dominant effect is true. The switch down from antiparallel to parallel, however, is relatively abrupt, sometimes followed by a gradual slope to completely parallel. The solid red line in Figure 5.11 marks the position of

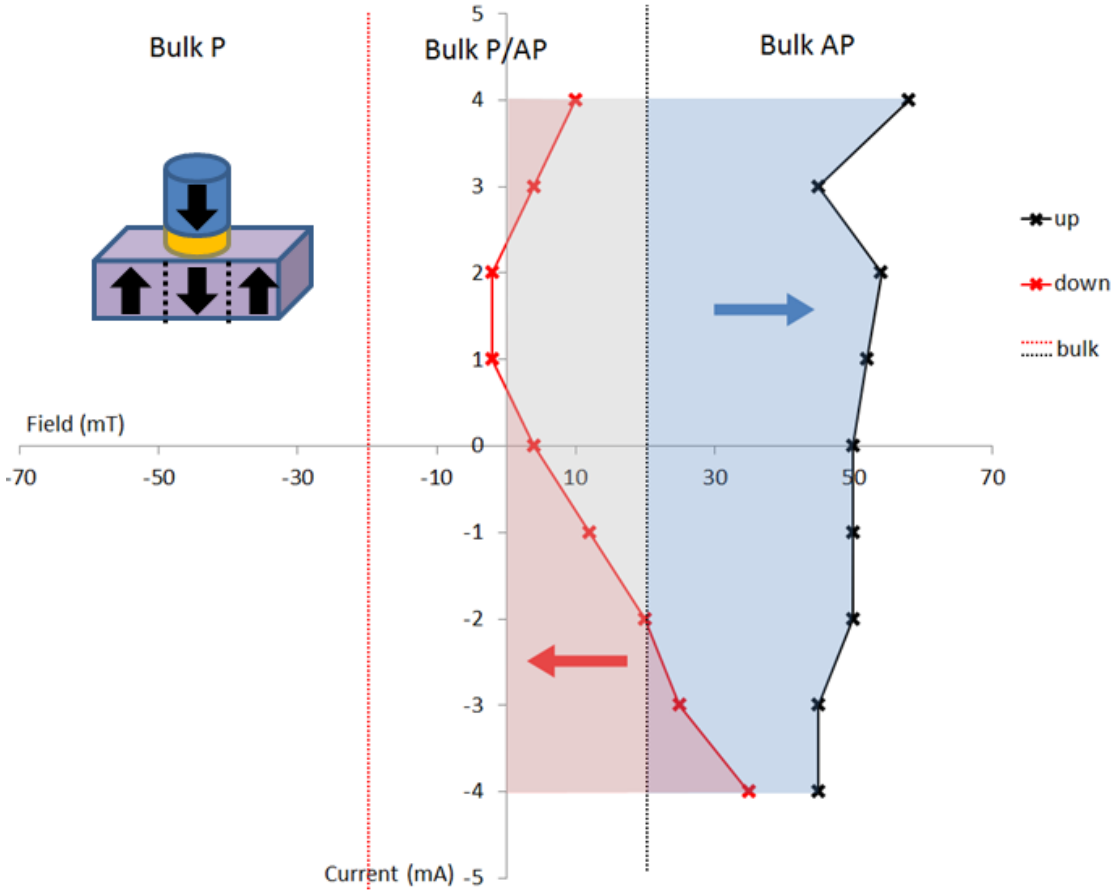

Figure 5.12: DC current vs field phase diagram for example device (2 μm wide Hall cross) recolored to show regions where an isolated domain may exist under the pillar (cartoon in inset). The grey area is reached by saturating the bulk, but not the region under the pillar and then ramping the field back down.

the abrupt switch down. If we look at this boundary, there is a clear asymmetry with current sign due to spin transfer torque. At higher currents, the switching starts to be thermally assisted because of Joule heating, which explains why at higher positive currents the switch down also starts to shift to more positive fields.

It is clear that the bilayer under the pillar is acting independently of the

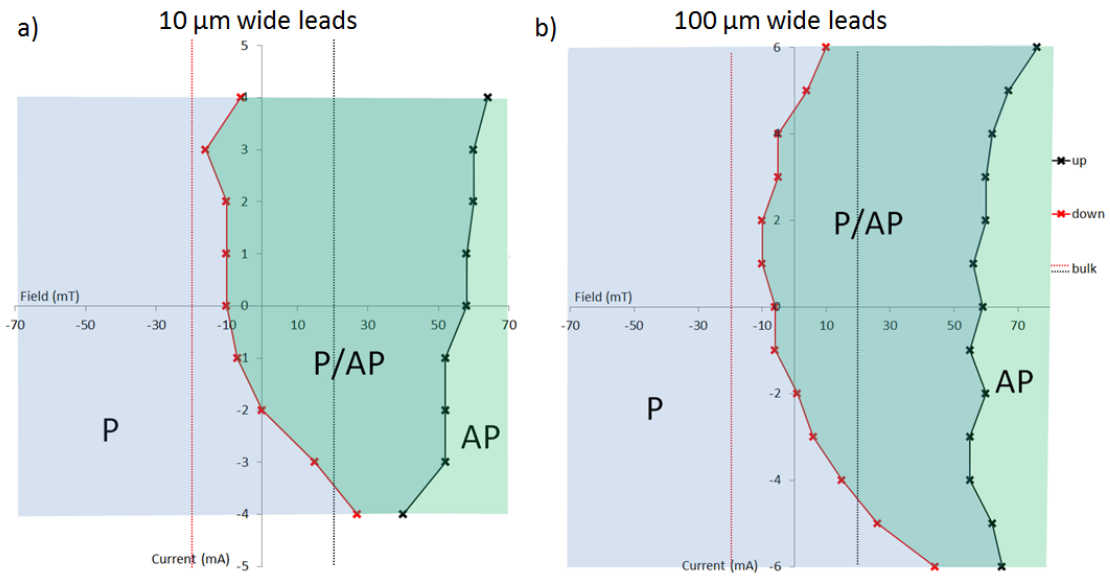

Figure 5.13: DC current vs field phase diagrams for devices with the free layer patterned into **(a)** 10 μm and **(b)** 100 μm wide leads. The behavior is qualitatively similar.

bulk, and there are regions where it is likely that an isolated domain, possibly a skyrmion, exists under the pillar. We recolor the phase diagram to make it clear where such a configuration may exist (Figure 5.12). In these regions, the bulk bilayer is almost completely in the antiparallel state, while the bilayer under the pillar is either partially or completely parallel to the fixed layer. Because the switch up is gradual, the gray region can be reached by doing a smaller field loop as in Figure 5.7d, which saturates the bulk bilayer, but not the area under the pillar. An isolated domain oriented opposite to the fixed layer is not possible in this system.

5.3.5 Size of the Bilayer

As already mentioned, we made devices with three different Hall cross widths. Changing the size of the bilayer while keeping the pillar size the same should have little effect on the behavior of the bilayer under the pillar, and indeed this is the case. So far, all results shown were for a device with 2 μm wide leads. Figure 5.11 shows the phase diagram for this device. For devices with a larger free layer, either 10 μm or 100 μm wide leads, the full GMR sweep (not shown) is roughly the same as in Figure 5.7b. Phase diagrams for two example devices of this type are shown in Figure 5.13. The behavior of all three sizes is qualitatively similar. The region under the pillar switches up at a much higher field than the bulk, 50-60 mT, due to interlayer coupling. The switch back down to parallel is affected by spin transfer torque, with some thermal assistance at higher current magnitudes.

There are also differences between bilayer size. In devices with wider leads, a larger current is required to get the same effect from spin transfer torque, and thermal effects seem less prominent, probably because the current is more spread out in the bilayer. It's possible these two effects are linked, because spin transfer torque induced switching can be thermally assisted, reducing the current required. Another possibility is that when the film is in the antiparallel state, it is more resistant to domain formation when the surrounding bulk is larger in size.

5.3.6 Platinum Thickness

We also made devices out of a film with a Co(1.7)/Pt(5) bilayer and the same Co/Pt fixed layer recipe. As already discussed, changing the platinum thickness from 10 nm to 5 nm in the bilayer does not seem to affect the properties of the film significantly. It is not surprising, then, that we observed qualitatively similar effects in these films. We observed a shift in the hysteresis curve from coupling with the pillar, and we also observed the effects of spin transfer torque. Unfortunately, due to unforeseen fabrication issues outside of our control, the device yield in the center of the wafer was poor. Doing a more thorough study of these films would require more time on the sputter system.

5.4 Discussion

In this project, we have demonstrated control of an isolated domain in a soft Co/Pt bilayer using a combination of spin transfer torque and applied magnetic field. While we have not proven for certain that the domain is a skyrmion or skyrmion bubble, the fact that Co/Pt has a strong DMI supporting chiral Néel walls is a decent indicator that skyrmions are being controlled for at least part of the phase space. Prior studies on the domain structure as a function of field in Co/Pt films support this claim, and the results by Davies, *et al.* are particularly illustrative [72] (Figure 5.14). They show that the transition from positive to negative saturation, or vice versa, can be divided into three regions - irreversible domain nucleation, reversible domain expansion and contraction, and irreversible domain annihilation. Second, they showed that isolated skyrmions can remain for fields much higher than the film's apparent saturation. Our

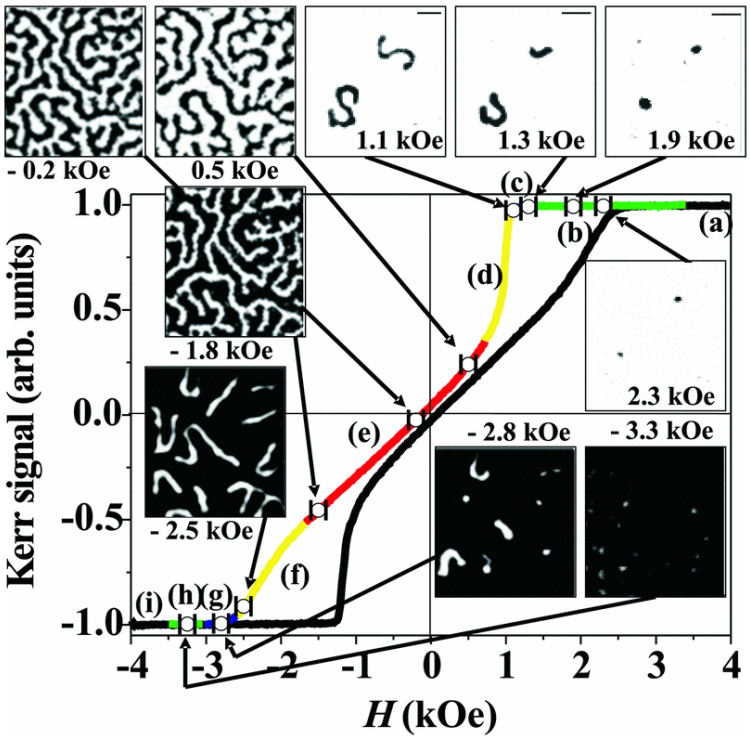

Figure 5.14: Transmission X Ray Microscopy images of the domain structure of $[Co(4\ Å)/Pt(7\ Å)]_{50}$ at various points along its hysteresis loop. Starting at positive saturation (**a**) and decreasing the field, isolated domains nucleate (**b**) and expand into small stripes (**c**). Then, using the isolated domains as nucleation sites, a sudden avalanche of stripes causes an abrupt switch (**d**). The domains reversibly expand or contract (**e**) and then start to annihilate irreversibly (**f**). After apparent saturation, isolated domains shrink into skyrmions (**g-h**) and then annihilate until the film is fully saturated (**i**). Figure from [72].

MOKE data (Figure 2.7) and our mumax simulations are qualitatively similar to these observations.

This helps to explain the shape of our GMR hysteresis curve. The gradual, nonhysteretic slope in Figure 5.7d corresponds to the domain shrinking as the field increases, or expanding as the field decreases. At around 50 mT the domain annihilates, which is irreversible. It is likely that immediately before domain annihilation, there is a skyrmion bubble under the pillar, and our simulations

support this claim. However there are still open questions. When the field is ramped back down, does the bubble simply expand in diameter or does it become a localized stripe domain? How long do skyrmion bubbles remain in the rest of the film, i.e. is the domain under the pillar the only one left? Better imaging techniques, like Lorentz TEM, will help resolve these questions.

Once the film is fully antiparallel to the pillar, the abrupt switch down corresponds to domain nucleation, and the slight slope after corresponds to its expansion. The abrupt transition resulting from nucleation can be shifted to higher fields using a DC current and cannot be reversed with current alone. At these higher fields, as demonstrated with MOKE, stripe domains do not exist. Since at least initially, the localized domain is almost certainly a skyrmion bubble, we have effectively demonstrated skyrmion creation via spin transfer torque. However, our simulations do not accurately model this effect, likely because thermal effects play an important role in our devices.

While we have been unable to produce a spin transfer torque strong enough to annihilate domains, we have demonstrated domain creation in a soft Co/Pt bilayer. We have also demonstrated that a perpendicularly magnetized nanopillar has a strong effect on the domains in the bilayer underneath. With a much larger spin polarization, even further control at higher applied fields is likely and domain annihilation may be possible. Compared to other experimentally proven techniques for skyrmion creation, ours is compact and can be utilized in ambient conditions using relatively simple equipment. The main downside is the very challenging fabrication process. Finding a way to deposit more uniform films and exploring different materials would be beneficial. Regardless, this work suggests that spin transfer torque may perhaps be a viable tool for

skyrmion creation and manipulation.

CHAPTER 6

CONCLUSION

In this work, we have investigated the effects spin transfer torques from a nanopillar have on Co/Pt bilayers with strong DMI. We fabricated spin-valve-like devices with a geometry that allowed us to separate bulk and local behavior of the bilayer using electrical techniques. In the process, we have also studied ways to effectively deposit and characterize these films.

While we did not see conclusive evidence of skyrmion dynamics in hard Co/Pt bilayers, we did observe a promising feature in the GMR signal, and we laid the groundwork for future research in this area. It would be useful to try a stronger polarizer, although the associated challenges with deposition and fabrication must be overcome. Low temperature measurements are another area to explore. Reduced thermal noise and increased impedance may make it easier to measure dynamics.

In our second project, we studied soft Co/Pt films that have a chiral domain structure at low fields. We demonstrated that coupling between the pillar and the bilayer can cause an isolated domain to persist after the bulk has fully saturated. We have also demonstrated that thermally assisted spin transfer torque can be used to nucleate an isolated domain. Further work in this area could include using a stronger polarizer to investigate whether spin transfer torque can also be used to annihilate domains. We could also determine the nature of the coupling between pillar and bilayer by changing the thickness of the copper spacer. Lastly, domain nucleation in other materials, such as CoFeB/Pt could be studied using this geometry.

Better imaging techniques would resolve some of the remaining questions involved in this research. It would be particularly useful to image full devices, perhaps by fabricating them on a silicon nitride membrane for investigation via Lorentz TEM. Scanning SQUID is another option, especially if a material with a larger bubble domain size, for example Ta/CoFeB/TaOx, is chosen. Another interesting direction would be to image a device with an in-plane polarizer. As suggested by micromagnetics simulations, an in plane polarizer should generate skyrmions at an experimentally viable current density. This effect would not produce a strong enough GMR signal to be detected using electrical techniques alone, so imaging is necessary.

In any case, while we did not observe all of the behavior we originally intended to, we have evidence of possible skyrmion generation via spin transfer torque in soft Co/Pt films. This research will hopefully be a good starting point for further work in the so-called field of skyrmionics, and perhaps with additional fine tuning of materials parameters, device geometry, and characterization techniques, spin transfer torque will prove to be a viable technique for creating skyrmions and topological dynamics.

APPENDIX A

TOPOLOGICAL INSULATORS

My initial research when I first joined the Ralph group focused on spin transport in topological insulators. The work with Alex Mellnik studying the spin Hall effect in bismuth selenide was a success [73] [74], however my follow up project was not. Since valuable information may still be gleaned from this failed project, particularly on the topic of fabrication, and since I spent a significant amount of my time as a graduate student on this work, I include an overview in this appendix.

A.0.1 Introduction

Three dimensional topological insulators (TIs), first predicted by Fu, Kane, and Mele in 2006 [75], are a novel state of matter characterized by an insulating bulk and conducting surface states. These materials have strong spin-orbit coupling, which results in states that would typically be in the valence band moving to the conduction band and vice versa. This band inversion leads to the formation of topologically-protected surface states traversing the band gap in the form of a Dirac cone. The surface states have many interesting and unusual properties. They are gapless, except in cases where time reversal symmetry is broken. The surface states are characterized by a spin texture with electron spin locked perpendicular to momentum. Backscattering is suppressed, and the surface states are expected to have high carrier mobility. These special properties may have applications in the future in areas such as spintronics and quantum computation [76] [77].

TI/FM bilayers have been predicted to have a higher spin-torque efficiency than any system observed to date [78]. This is important in magnetic memory applications since a high spin-torque efficiency results in a low switching current. Members of our group fabricated topological insulator bismuth selenide (Bi_2Se3_3 / permalloy (Py) bilayers and measured in-plane and out-of-plane spin Hall ratios of order 1, in agreement with theory [73]. However, the out-of-plane torque is much larger than can be attributed to the Oersted field alone.

To help determine the origin of the large out-of-plane torque and to investigate the effects of the surface states, we fabricated dual-gated Bi_2Se3_3 devices pictured in Figure A.1. With static gating as shown, the gated regions will have different surface state carrier densities, which will result in a voltage-dependent net spin current flowing into the Py wire. Such a device is interesting because it should be possible to generate a spin torque on the Py without flowing a charge current in the topological insulator. If we apply gate voltages such that the chemical potential is in the band gap, this should eliminate spin Hall contributions from the bulk and we can investigate the effects of the surface states alone.

A.0.2 Methods

In this project, we attempted to measure spin currents in a dual-gated Bi_2Se3_3 device. Using values found in the literature, the maximum change in surface state carrier density achieved by gating is $\Delta n_{surface} = 2.5 \times 10^{13}$ cm^{-2} [79], and the Fermi velocity for Bi_2Se_3 is $v_F = 4.2 \times 10^5$ m/s [80]. Then the maximum spin

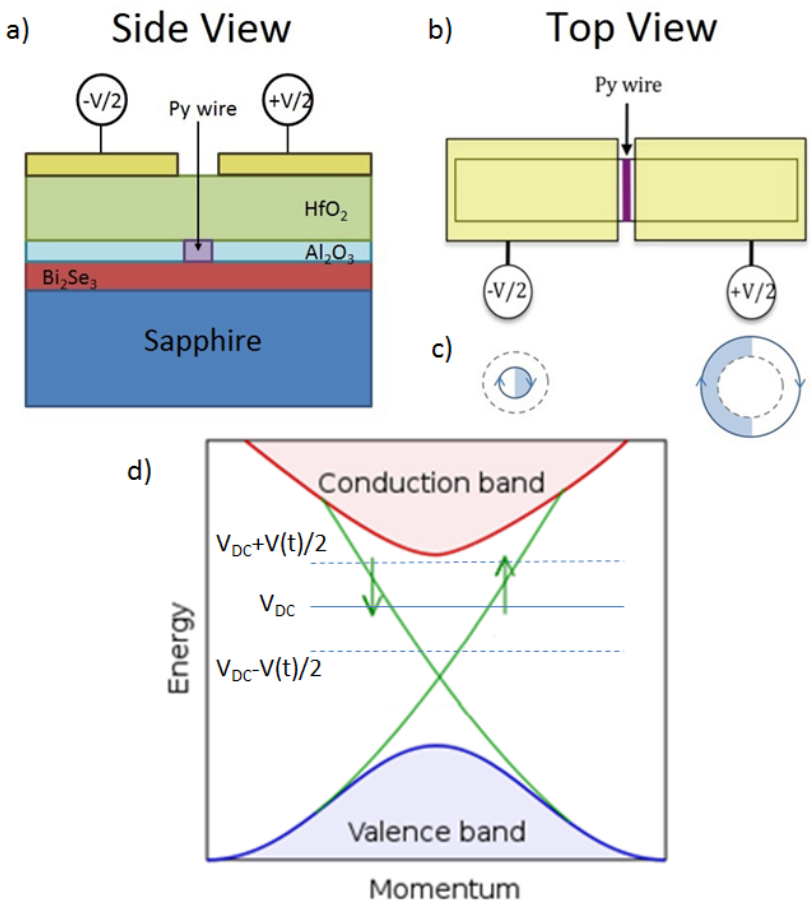

Figure A.1: Schematic of the side **(a)** and top **(b)** of our dual gate Bi_2Se3_3 device. Gate voltages are applied such that a net spin current flows into the permalloy (Py) wire in the central region. **(c)** shows a cartoon of the Fermi surface in k space. Gating moves the chemical potential up or down on the Dirac cone, changing the spin current flowing in a given direction. The dotted line indicates the ungated case. **(d)** Dirac cone showing voltages required in this experiment. A DC voltage is required to tune the chemical potential into the band gap. The AC voltage offsets as in **(c)**.

current flowing into the permalloy nanowire per unit length is,

$$J_s = (n_\uparrow - n_\downarrow)v_F \sim 10^{17}\left(\frac{\hbar}{2}\right)s^{-1}\mu m^{-1}. \tag{A.1}$$

One way to measure the spin current is to oscillate the gate voltages near the ferromagnetic resonance (FMR) frequency of Py. This will result in an oscillating

spin current flowing into the Py wire, and spin torque driven ferromagnetic resonance (ST-FMR) will occur. The resulting magnetization precession will cause the resistance to oscillate in the wire due to the strong anisotropic magnetoresistance (AMR) of Py. If an RF current is applied through the Py wire, then we should be able to measure a DC mixing voltage. Using ST-FMR theory, the mixing voltage signal per micron segment in the wire can be calculated using [81] [82],

$$|V_{mix}| = \frac{1}{4}\frac{dR}{d\theta}\frac{\gamma I_{RF}}{M_s Vol}\frac{\sin\theta}{\sigma}\frac{\hbar}{2e}I_{(S,RF)} \tag{A.2}$$

where R is the resistance of the wire, γ is the gyromagnetic ratio, I_{RF} is the RF charge current flowing through the Py, $M_S Vol$ is the total magnetic moment of the micron segment of wire, θ is the angle between the magnetization and the spin axis, $I_{(S,R)}\hbar/2e$ is the amplitude of the RF spin current, and $\sigma \approx \alpha\gamma 2\pi M_{eff}$, where α is the Gilbert damping parameter and $4\pi M_{eff}$ is the demagnetization field. If we assume the Py wire is 50 nm wide and 5 nm thick and the RF current is 1 mA, then we estimate the mixing voltage signal to be roughly 0.03 volts for the 1 micron segment of wire.

A second way to measure the predicted spin current is to apply DC voltages to the gates. This will result in a DC spin current in the central region, which will change the effective magnetic damping in the Py. Using either a microwave cavity or coplanar waveguides to generate an external RF magnetic field with frequency f and magnitude H_{ext}, FMR can be excited in the nanowire. The change in magnetic damping should increase or decrease the FMR linewidth, Δ, which we can measure as a function of DC gate voltage and use to calculate the spin current [81]:

$$\Delta = \frac{2\pi f}{\gamma}(\alpha + \frac{\sin\theta}{(H_{ext} + 2\pi M_{eff})M_s Vol}\frac{\hbar}{2e}I_{(S,DC)}). \tag{A.3}$$

If we assume the external field has a frequency of 8 GHz, a magnitude of 1000

Oe, and is applied at an angle of 45° relative to the wire in the sample plane, then we expect a change in the damping coefficient of at least 0.028, which should be measurable.

A.0.3 Fabrication

A few factors made working with Bi_2Se_3 challenging. First, it oxidizes when exposed to air, so there must always be a protective layer on top of the film. Second, Bi_2Se_3 has poor adhesion on most substrates, so sonication must be avoided. It is also etched by most plasmas, so oxygen plasma cleaning should also be avoided. Lastly, processing has been known to introduce selenium vacancies into the film, which brings the Fermi level into the conduction band. We compensated for this through gating.

We start with Bi_2Se_3 thin films grown by molecular beam epitaxy on sapphire by the Nitin Samarth group at Penn State University (Figure A.2a). To protect the bismuth selenide from exposure to air, the samples are covered in an amorphous selenium capping layer, which is removed by baking the samples at 240°C for an hour in our sputter system. We then sputter a 4 nm thick layer of aluminum before removing the samples from vacuum. The thin aluminum layer oxidizes when exposed to air (Figure A.2b).

The next step is to fabricate Py nanowires using electron beam lithography (Figure A.2c,h). We used an insulating sapphire substrate suitable for RF measurements, and so, to prevent charging, we had to develop a recipe using a conducting thin film, ESpacer 300Z. After developing, and immediately before deposition, we etch the exposed Al_2O_3 by soaking for 30 seconds in MIF726 de-

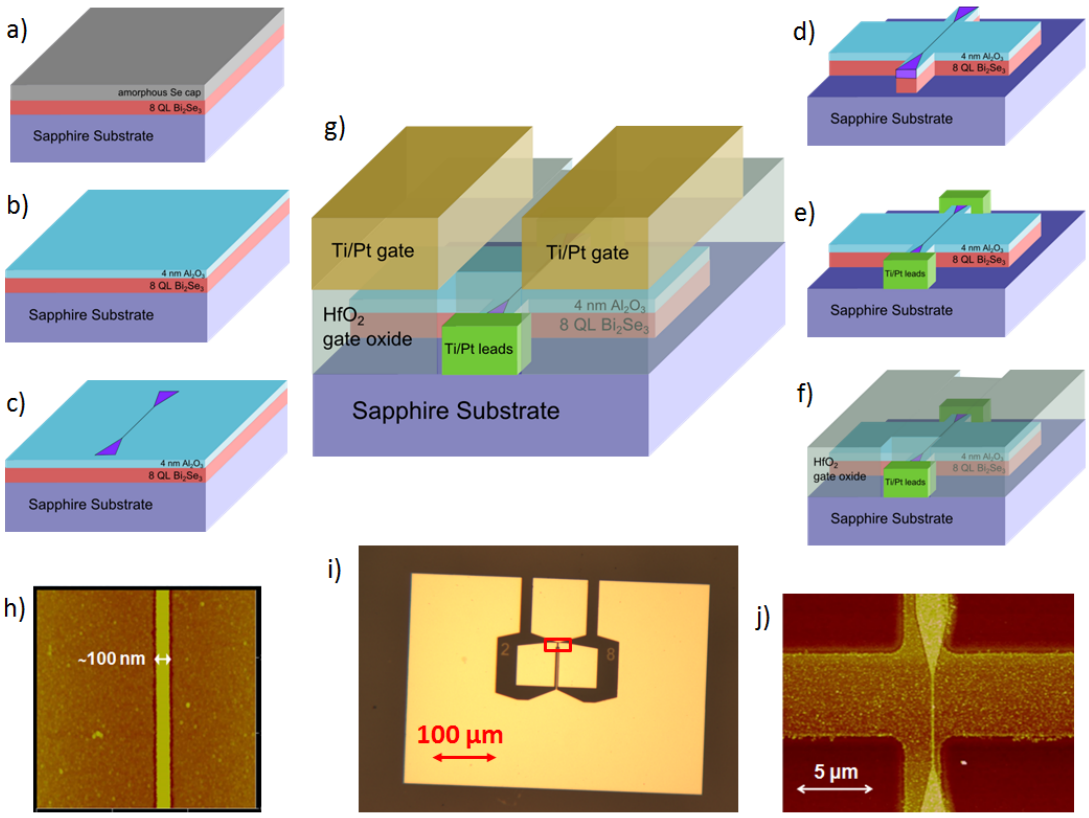

Figure A.2: Dual gate Bi_2Se3_3 devices fabrication. **(a)** Bulk film. **(b)** Remove Se cap and deposit 4 nm Al. **(c)** Etch Al_2O_3 and deposit Py nanowire. **(d)** CF_4 etch into bars. **(e)** Deposit contact pads. **(f)** Deposit gate oxide. **(g)** Deposit gates and etch oxide to expose contact pads. **(h)** MFM image of Py nanowire. **(i)** Optical image of finished device. The Bi_2Se_3 bar is in the red box. **(j)** MFM image of bar and Py nanowire.

veloper (TMAH etches aluminum). Permalloy is evaporated in the Odd Hour tool in CNF. Because we couldn't sonicate or plasma clean without damaging the Bi_2Se_3, we had difficulties removing residual PMMA resist from our samples. We were able to remove the majority of the resist by soaking in acetone followed by 1165 stripper, heated to 120°C, for two days. The exact recipe can be found in Appendix B.

Next, we etched the Bi_2Se_3 into smaller bars needed for our devices using a CF_4 reactive ion etch process (Figure A.2d). After etching, we put down gold contact pads, deposit the gate oxide, 15-20 nm hafnia, on top of the entire sample using atomic layer deposition, and make the gold top gates (Figure A.2e-f). Lastly, we plasma etch through the hafnia to expose the contact pads (Figure A.2g). We later switched to Ti/Pt contact pads and gates because of improved adhesion and ease of deposition (using the AJA sputter system in CNF).

A.0.4 Measurements and Discussion

Due to its relative ease, we focused on the first measurement scheme discussed in the Methods section (ST-FMR). We observed an interesting field dependent, hysteretic background in the mixing voltage signal. The background had a strong dependence on the RF power and DC gating, and possibly on wire length (Figure A.3a,b). A similar background was observed in control samples consisting of a permalloy wire on blank sapphire (Figure A.3c,d). Because of its angle and power dependence, we believe it is due to the Anomalous Nernst Effect (ANE), which is a heating effect observed in ferromagnetic materials. When there is a temperature gradient in a ferromagnet, a voltage gradient develops perpendicular to the plane made by the magnetization and the temperature gradient. The differences in thermal conductivity on the bottom and top interfaces of the Py wire could cause a slight out of plane temperature gradient from Joule heating. The ANE would then be at it's maximum when the field is 90° to the wire, which agrees with the behavior of the background signal. Secondly, the fact that it scales linearly with power indicates it could be a heating effect.

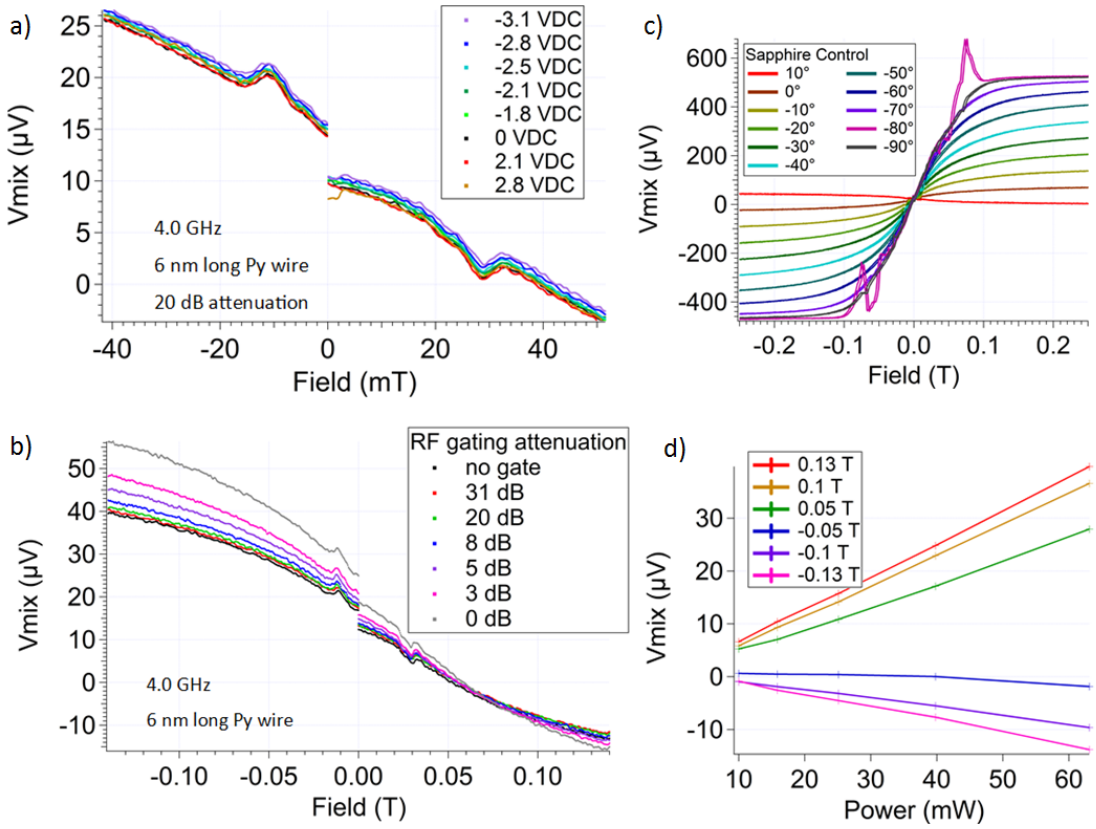

Figure A.3: ST-FMR data for an example device showing the **(a)** DC and **(b)** RF gating dependence of the mixing voltage. **(c-d)** Measurements of a permalloy wire on blank sapphire show a similar background. The angle **(c)** and power **(d)** dependence indicate this could be a heating effect.

Another interesting feature we observed in our ST-FMR data was the two resonance peaks. We would expect any signal resulting from spin currents in the Bi_2Se_3 to depend on the DC and RF gating, but this is not the case. The peaks are also unaffected by gating, and so we believe they are most likely due to the Oersted field.

Other than the Nernst effect, we did not observe any interesting behavior in our devices. There are several possible reasons why this project didn't work. It is likely that so many fabrication steps damaged the Bi_2Se_3, destroying the

surface states, or perhaps DC gating was not strong enough to bring the Fermi level into the gap. Another issue is that high frequency gating is nontrivial. It's possible most of the RF signal was getting reflected from the gates rather than transmitted, due to the large impedance mismatch.

APPENDIX B

NANOFABRICATION RECIPES

To perhaps make life simpler for future graduate students, here I list some of the recipes used in my fabrication processes, which were explained in detail in Chapter 3 and Appendix A.

B.1 Photolithography - LOR3A / Shipley 1805 Bilayer

This is my standard recipe that works for all photolithography steps in Co/Pt spin valve and dual gate Bi_2Se_3 device fabrication.

1) LOR 3A - 3000 rpm, 1000 rpm/s, 60 seconds, bake at 180°C for 5 minutes.

2) S1805 - 3000 rpm, 1000 rpm/s, 60 seconds, bake at 115°C for 1 min 15 sec.

3) Expose 0.26 seconds in 5X stepper.

4) Develop for 1 minute in MIF 726. Rinse in DI water. Do not use acetone or IPA, as they react with LOR3A, making it nearly impossible to remove!

If using only Shipley resist, the same recipe can be used, omitting the first step and decreasing the develop time to 45 seconds. A shorter develop time is also necessary for patterns with very small features, ~ 1-5 μm. I typically start with 40 seconds and increase the time as required.

B.2 Nanopillar Ebeam Lithography Recipe

This is the recipe I used to make nanopillars in my spin valve devices. Make sure to use new resist for this process. Otherwise the pillars may not lift off properly.

1) Omnicoat - 2000 rpm, 1000 rpm/s, 60 seconds, bake at 180°C for 1 minute.

2) Repeat step 1.

3) 4% 495K PMMA - 2000 rpm, 500 rpm/s, 120 seconds, bake at 170°C for 10 minutes.

4) 6% HSQ - 2000 rpm, 500 rpm/s, 60 seconds, bake at 170°C for 1 minute.

5) JEOL 6300 - lens 4, 2 nA, dose 2000 $\mu C/cm^2$.

B.2.1 Development

Because the pattern doesn't adhere very well to the surface, be very gentle with these steps. Don't move the sample around in developer too much, and blow dry mostly from the back.

1) MIF 726 - 2 minutes.

2) Rinse in DI water, gently dry with N_2.

3) Oxford 81 - O_2 plasma clean - 1 min 30 sec, 100 W, 20 sccm, 50 mTorr.

B.2.2 Ion Mill and SiO_2 Deposition

1) Ion Mill - 150° angle, timed (calibrate using mass spectrometer as described in Chapter 3), 30 seconds on / 10 seconds off.

2) Ion Mill - in situ aluminum deposition - 90° angle, 13 minutes, 40 W, 50 sccm, 2.5 mTorr.

3) Even Hour Evaporator - 80 nm SiO_2 (Make sure to transfer quickly from ion mill. Pillars may degrade over time when exposed to air).

B.2.3 Liftoff

Repeating these steps may be necessary.

1) PG Remover - 130°C, ~ 5 hours. (Don't be alarmed if the PG Remover turns dark brown or black. This just means the developer has started to break down a bit from heating. We haven't noticed any change in sample quality when this happens.)

2) Sonicate at least 90 minutes.

3) Rinse in DI water, blow dry with N_2, and check in optical microscope.

B.2.4 Troubleshooting

If pillars are not lifting off properly -

1) Repeat liftoff steps at least once.

2) Verify that all of the resists have been replaced recently. If the HSQ is more than a couple weeks old, it should be replaced. Dirty resist may also cause liftoff problems.

3) Check that the neutralizer filament in the ion mill is 0.007" W wire. Thicker wires have been known to cause more sample heating.

4) Check that the hotplate is clean and functioning properly.

If there are lots of bubbles in the resist after developing -

1) While developing in MIF 726, gently lift the sample out and let the liquid run off for a couple seconds. Do this a few times until the bubbles are gone.

2) Bake the PMMA for longer. Increasing the time from 2 minutes to 10 minutes was an improvement. We suspect even longer may help get rid of bubbles, although it may also make liftoff more difficult.

3) Clean your samples before spinning resist. Dirt nucleates bubbles.

4) Check that all of the resists have been replaced recently and are not dirty.

B.3 Bottom Contacts for Co/Pt Devices

This recipe corresponds to lithography step 3 of the spin valve device fabrication (see Chapter 3). 80 nm SiO_2 is removed using a plasma etch prior to sputtering the pads.

1) After patterning sample, etch SiO_2 using the Oxford 81. CF_4, 40 mTorr, 150 W, 30 sccm, 2 minutes.

2) Sputter contact pads in AJA. 2 minutes Ar clean, 5 nm Ti, 100 nm Pt.

3) Strip using 1165. Sonication may also be necessary.

B.4 Permalloy Nanowire Ebeam Lithography Recipe

This recipe was used to make 100 nm diameter Py nanowires in my dual gate bismuth selenide devices. It was designed to work on insulating sapphire substrates and assumes the film has a 4 nm Al_2O_3 cap. The PMMA bilayer has an undercut that works well for liftoff of small features. Because Bi_2Se_3 has poor adhesion, the resist stripping process avoids sonication. If adhesion is not an issue, sonication and a shorter soak in heated 1165 should be sufficient for resist removal.

1) Spin 11% 1:2 PMMA(8.5)MAA copolymer, 2000 rpm, 60 seconds. Bake 170° C for 15 minutes.

2) Spin 2% 495K PMMA, 3000 rpm, 60 seconds. Bake 170° C for 15 minutes.

3) Spin ESpacer 300Z, 3000 rpm, 15 seconds. Bake 90° C for 60 seconds. ESpacer

300Z is a conducting polymer used to prevent charging on insulating substrates, so this step can be skipped, depending on the substrate.

4) Expose pattern in JEOL 6300, 2 nA, lens 4. Area dose 5000 μC/cm^2. Line dose 8000 μC/cm^2.

5) If you used ESpacer, dip in DI water for a few seconds to remove prior to developing.

6) Develop in 1:3 MIBK:IPA for 1 minute 15 seconds.

7) To improve the undercut, dip in methanol for 15 seconds, then rinse with IPA.

8) Immediately before Py deposition, etch 4 nm Al_2O_3 cap by dipping in MIF726 for 30 seconds.

9) Evaporate Py in the Odd Hour. The following parameters were used - ρ_{Py} = 8.691 g/cm^3 and Z = 0.360. We deposited thickness up to 15 nm, although thicker wires are probably possible.

10) Strip resist by soaking for roughly 24 hours in acetone. Be careful it doesn't completely evaporate or the Py will be impossible to remove!

11) Remove remaining resist by soaking for 1-2 days in hot 1165 stripper (~ 120°C).

B.5 Recipe for Etching 8 QL of Bi_2Se_3

RIE etching was used to etch Bi_2Se_3 into bars. We tried ion milling, but because sonication was not an option, "baked on" resist was very difficult to remove.

Plasma etching is a shorter process, with less heating, so resist was easier to remove afterward. This process uses the Oxford 81 tool in CNF.

1) 30 seconds CF_4, 30 sccm, 40 mTorr, 150 W.

2) 1 minute O_2 chamber clean after removing sample (required by CNF staff). Soak sample in 1165 to remove resist.

BIBLIOGRAPHY

[1] R. Tomasello et al. A Strategy for the Design of Skyrmion Racetrack Memories. *Scientific Reports*, 4:6784, 2014.

[2] I. Dzyaloshinsky. A Thermodynamic Theory of "Weak" Ferromagnetism of Antiferromagnets. *Journal of Physics and Chemistry of Solids*, 4(4):241–255, 1958.

[3] T. Moriya. Anisotropic Superexchange Interaction and Weak Ferromagnetism. *Physical Review*, 120:91, 1960.

[4] A. Fert, N. Reyren, and V. Cros. Magnetic Skyrmions: Advances in Physics and Potential Applications. *Nature Reviews Materials*, 2(17031), 2017.

[5] N. Nagaosa and Y. Tokura. Topological Properties and Dynamics of Magnetic Skyrmions. *Nature Nanotechnology*, 8:899–911, 2013.

[6] A. P. Malozemoff and J. C. Slonczewski. *Magnetic Domain Walls in Bubble Materials*. Academic Press.

[7] Y. S. Lin, J. Grundy, and E. A Giess. Bubble Domains in Magnetostatically Coupled Garnet Films. *Applied Physics Letters*, 23:485–487, 1973.

[8] T. Suzuki. A Study of Magnetization Distribution of Submicron Bubbles in Sputtered Ho-Co Thin Films. *Journal of Magnetism and Magnetic Materials*, 31, 1983.

[9] T. Okubo, S. Chung, and H. Kawamura. Multiple-q States and the Skyrmion Lattice of the Triangular-Lattice Heisenberg Antiferromagnet under Magnetic Fields. *Physical Review Letters*, 108:017206, 2012.

[10] S. Heinze et al. Spontaneous Atomic-Scale Magnetic Skyrmion Lattice in Two Dimensions. *Nature Physics*, 7:713–718, 2011.

[11] S. Muhlbauer et al. Skyrmion Lattice in a Chiral Magnet. *Science*, 323(5916):915–919, 2009.

[12] X. Z. Yu et al. Real-Space Observation of a Two-Dimensional Skyrmion Crystal. *Nature*, 465:901–904, 2010.

[13] A. Tonomura et al. Real-Space Observation of Skyrmion Lattice in Helimagnet MnSi Thin Samples. *Nano Letters*, 12(3):1673–1677, 2012.

[14] X. Z. Yu et al. Near Room-Temperature Formation of a Skyrmion Crystal in Thin-Films of the Helimagnet FeGe. *Nature Materials*, 10:106–109, 2011.

[15] W. Munzer et al. Skyrmion Lattice in the Doped Semiconductor $Fe_{1-x}Co_xSi$. *Physical Review B*, 81:041203, 2010.

[16] K. Shibata et al. Towards Control of the Size and Helicity of Skyrmions in Helimagnetic Alloys by SpinOrbit Coupling. *Nature Nanotechnology*, 8:723–728, 2013.

[17] S. Seki, X. Z. Yu, S. Ishiwata, and Y. Tokura. Observation of Skyrmions in a Multiferroic Material. *Science*, 336(6078):198–201, 2012.

[18] I. Kezsmarki et al. Néel-Type Skyrmion Lattice with Confined Orientation in the Polar Magnetic Semiconductor GaV_4S_8. *Nature Materials*, 14:1116–1122, 2015.

[19] C. Moreau-Luchaire et al. Additive Interfacial Chiral Interaction in Multilayers for Stabilization of Small Individual Skyrmions at Room Temperature. *Nature Nanotechnology*, 11:444–448, 2016.

[20] A. Kubetzka, M. Bode, O. Pietzsch, and R. Wiesendanger. Spin-Polarized Scanning Tunneling Microscopy with Antiferromagnetic Probe Tips. *Physical Review Letters*, 88(5):057201, 2002.

[21] M. Heide, G. Bihlmayer, and S. Blugel. Dzyaloshinskii-Moriya interaction Accounting for the Orientation of Magnetic Domains in Ultrathin Films: Fe/W(110). *Phyical Review B*, 78:140403, 2008.

[22] H. Yang et al. Controlling Dzyaloshinskii-Moriya Interaction via Chirality Dependent Atomic-Layer Stacking, Insulator Capping and Electric Field. arXiv:1603.01847, 2016.

[23] H. Yang et al. Significant Dzyaloshinskii-Moriya Interaction at Graphene-Ferromagnet Interfaces due to Rashba-effect. arXiv:1704.09023, 2017.

[24] C. Moreau-Luchaire et al. Skyrmions at Room Temperature: From Magnetic Thin Films to Magnetic Multilayers. arXiv:1502.07853, 2015.

[25] O. Boulle et al. Room-Temperature Chiral Magnetic Skyrmions in Ultrathin Magnetic Nanostructures. *Nature Nanotechnology*, 11:449–454, 2016.

[26] W. Jiang et al. Blowing Magnetic Skyrmion Bubbles. *Science*, 349(6245):283–286, 2015.

[27] A. Soumyanarayanan et al. Tunable Room Temperature Magnetic Skyrmions in Ir/Fe/Co/Pt Multilayers. arXiv:1606.06034, 2016.

[28] G. Chen, A. Mascaraque, A. N'Diaye, and A. Schmid. Room Temperature Skyrmion Ground State Stabilized Through Interlayer Exchange Coupling. *Applied Physics Letters*, 106:242404, 2015.

[29] D. Gilbert et al. Realization of Ground-State Artificial Skyrmion Lattices at Room Temperature. *Nature Communications*, 6:8462, 2015.

[30] A. K. Nandy, N. S. Kiselev, and S. Blugel. Interlayer Exchange Coupling: A General Scheme Turning Chiral Magnets into Magnetic Multilayers Carrying Atomic-Scale Skyrmions. *Physical Review Letters*, 116:177202, 2016.

[31] H. Yang et al. Anatomy of Dzyaloshinskii-Moriya Interaction at Co/Pt Interfaces. *Physical Review Letters*, 115:267210, 2015.

[32] N. Romming et al. Writing and Deleting Single Magnetic Skyrmions. *Science*, 341(6146):636–639, 2013.

[33] P. Hsu et al. Electric-Field-Driven Switching of Individual Magnetic Skyrmions. *Nature Nanotechnology*, 12:123–126, 2017.

[34] G. Yu et al. Room-Temperature Skyrmion Shift Device for Memory Application. *Nano Letters*, 17(1):261–268, 2017.

[35] F. Buttner et al. Field-Free Deterministic Ultra Fast Creation of Skyrmions by Spin Orbit Torques. arXiv:1705.01927, 2017.

[36] J. C. Slonczewski. Current-Driven Excitation of Magnetic Multilayers. *Journal of Magnetism and Magnetic Materials*, 159(1-2):L1–L7, 1996.

[37] L. Berger. Emission of Spin Waves by a Magnetic Multilayer Traversed by a Current. *Physical Review B*, 54:9353, 1996.

[38] D. C. Ralph and M. D. Stiles. Spin Transfer Torques. *Journal of Magnetism and Magnetic Materials*, 320:1190–1216, 2008.

[39] D. C. Ralph and R. A. Buhrman. Spin-Transfer Torques and Nanomagnets. In S. Maekawa, editor, *Concepts in Spin Electronics*, chapter 5, pages 195–238. Oxford University Press, Oxford, UK, 2006.

[40] G. Binasch, P. Grunberg, F. Saurenbach, and W. Zinn. Enhanced Magnetoresistance in Layered Magnetic Structures with Antiferromagnetic Interlayer Exchange. *Physical Review B*, 39:4828, 1989.

[41] M. N. Baibich et al. Giant Magnetoresistance of (001)Fe/(001)Cr Magnetic Superlattices. *Physical Review Letters*, 61:2472, 1988.

[42] I. Ennen et al. Giant Magnetoresistance: Basic Concepts, Microstructure, Magnetic Interactions and Applications. *Sensors(Basel)*, 16(6):904, 2016.

[43] M. Kisielewski et al. Magnetic Anisotropy and Magnetization Reversal Processes in Pt/Co/Pt Films. *Journal of Magnetism and Magnetic Materials*, 260:231–243, 2003.

[44] M. Belmeguenai et al. Interfacial Dzyaloshinskii-Moriya Interaction in Perpendicularly Magnetized Pt/Co/AlOx Ultrathin Films Measured by Brillouin Light Spectroscopy. *Physical Review B*, 91:180405, 2015.

[45] J. Park et al. Co/Pt Multilayer Based Magnetic Tunnel Junctions Using Perpendicular Magnetic Anisotropy. *Journal of Applied Physics*, 103(7), 2007.

[46] O. Lee. Non-Collinear Spin-Torque Driven Excitation in Nanomagnets. PhD Thesis, School of Applied and Engineering Physics, Cornell University, 2013.

[47] F. Delille et al. Thermal Variation of Current Perpendicular-to-Plane Giant Magnetoresistance in Laminated and Nonlaminated Spin Valves. *Journal of Applied Physics*, 100:013912, 2006.

[48] A. Deac et al. Current-Induced Magnetization Switching in Exchange-Biased Spin Valves for Current-Perpendicular-to-Plane Giant Magnetoresistance Heads. *Physical Review B*, 73:064414, 2006.

[49] D. Houssameddine et al. Spin-Torque Oscillator Using a Perpendicular Polarizer and a Planar Free Layer. *Nature Materials*, 6:447–453, 2007.

[50] S. Mangin et al. Current-Induced Magnetization Reversal in Nanopillars with Perpendicular Anisotropy. *Nature Materials*, 5:210–215, 2006.

[51] A. Hendrych, R. Kubinek, and A. V. Zhukov. The Magnetic Force Microscopy and its Capability for Nanomagnetic Studies - The Short Compendium. In A. Mendez-Vilas and J. Diaz, editors, *Modern Research and Educational Topics in Microscopy*, pages 805–811. Formatex, Badajoz, Spain, 2007.

[52] F. A. Ferri, M. A. Pereira-da Silva, and E. Marega Jr. Magnetic Force Microscopy: Basic Principles and Applications. In V. Bellitto, editor, *Atomic Force Microscopy - Imaging, Measuring and Manipulating Surfaces at the Atomic Scale*, chapter 3, pages 39–56. InTech, Rijeka, Croatia, 2012.

[53] A. Rugar. Construction of a Widefield Magneto-Optic Kerr Effect Microscope for Studies of Current-Driven Dynamics of Chiral Magnetic Domains. Undergraduate Honors Thesis, School of Applied and Engineering Physics, Cornell University, 2017.

[54] S. G. Je et al. Asymmetric Magnetic Domain-Wall Motion by the Dzyaloshinskii-Moriya Interaction. *Physical Review B*, 88:214401, 2013.

[55] A. Hrabec et al. Measuring and Tailoring the Dzyaloshinskii-Moriya Interaction in Perpendicularly Magnetized Thin Films. *Physical Review B*, 90:020402(R), 2014.

[56] M. R. Freeman and W. K. Hiebert. Stroboscopic Microscopy of Magnetic Dynamics. In B. Hillebrands and K. Ounadjela, editors, *Spin Dynamics in Confined Magnetic Structures I*, volume 83, pages 93–126. Springer, Berlin, Heidelberg, 2002.

[57] M. Huber et al. Gradiometric Micro-SQUID Susceptometer for Scanning Measurements of Mesoscopic Samples. *Review of Scientific Instruments*, 79:053704, 2008.

[58] S. Pollard et al. Observation of Stable Néel Skyrmions in Cobalt/Palladium Multilayers with Lorentz Transmission Electron Microscopy. *Nature Communications*, 8:14761, 2017.

[59] M. Carpentieri, R. Tomasello, R. Zivieri, and G. Finocchio. Topological, Non-Topological and Instanton Droplets Driven by Spin-Transfer Torque in Materials with Perpendicular Magnetic Anisotropy and Dzyaloshinskii-iMoriya Interaction. *Scientific Reports*, 5:16184, 2015.

[60] A. Vansteenkiste et al. The Design and Verification of MuMax3. *AIP Advances*, 4:107133, 2014.

[61] A. Vansteenkiste. Mumax3 Webpage. http://mumax.github.io/.

[62] J. Sampaio et al. Nucleation, Stability and Current-Induced Motion of Isolated Magnetic Skyrmions in Nanostructures. *Nature Nanotechnology*, 8:839–844, 2013.

[63] W. Kang et al. Skyrmion-Electronics: And Overview and Outlook. *Proceedings of the IEEE*, pages 2040–2061, 2016.

[64] J.C.S. Kools, T.G.S.M. Rijks, A.E.M. De Veirman, and R. Coehoorn. On the Ferromagnetic Interlayer Coupling in Exchange-Biased Spin-Valve Multilayers. *IEEE Transactions on Magnetics*, 31(6):3918–3920, 1995.

[65] L. Néel. A New Method of Coupling the Magnetization of Two Thin Ferromagnetic Films. *C.R. Acad. Sci. Paris*, 255:1676, 1962.

[66] J. Moritz, F. Garcia, J.C. Toussaint, B. Dieny, and J. P. Nozieres. Orange Peel Coupling in Multilayers with Perpendicular Magnetic Anisotropy: Application to (Co/Pt)-based Exchange-Biased Spin-Valves. *Europhysics Letters*, 65(1):123, 2004.

[67] M.T. Johnson, P.J.H. Bloemen, F.J.A. den Broeder, and J.J. de Vries. Magnetic Anisotropy in Metallic Multilayers. *Reports on Progress in Physics*, 59:1409–1458, 1996.

[68] C. Kooy and U. Enz. Experimental and Theoretical Study of the Domain Configuration in Thin Layers of $BaFe_{12}O_{19}$. *Philips Research Reports*, 15:7–29, 1960.

[69] C. Kittel. Physical Theory of Ferromagnetic Domains. *Reviews of Modern Physics*, 21:4, 1949.

[70] S. Woo et al. Observation of Room-Temperature Magnetic Skyrmions and their Current-Driven Dynamics in Ultrathin Metallic Ferromagnets. *Nature Materials*, 15:501–506, 2016.

[71] M. Yamanouchi et al. Domain Structure in CoFeB Thin Films With Perpendicular Magnetic Anisotropy. *IEEE Magnetics Letters*, 2:3000304, 2011.

[72] J. E. Davies et al. Magnetization Reversal of Co/Pt Multilayers: Microscopic Origin of High-Field Magnetic Irreversibility. *Physical Review B*, 70:224434, 2004.

[73] A.R. Mellnik et al. Spin-Transfer Torque Generated by a Topological Insulator. *Nature*, 511:449–451, 2014.

[74] A. Mellnik. Measurements Of Spin Torques Generated By Topological Insulators And Heavy Metals. PhD Thesis, Physics Department, Cornell University, 2015.

[75] L. Fu, C.L. Kane, and E.J. Mele. Topological Insulators in Three Dimensions. *Physical Review Letters*, 98:106803, 2007.

[76] M.Z. Hasan and C.L. Kane. Colloquium: Topological Insulators. *Review of Modern Physics*, 82:3045, 2010.

[77] L. Fu and C.L. Kane. Topological Insulators with Inversion Symmetry. *Physical Review B*, 76:045302, 2007.

[78] M.H. Fischer, A. Vaezi, A. Manchon, and E.A. Kim. Spin-Torque Generation in Topological-Insulator-Based Heterostructures. *Physical Review B*, 93:125303, 2016.

[79] J. Chen et al. Gate-Voltage Control of Chemical Potential and Weak Antilocalization in Bi_2Se_3. *Physical Review Letters*, 105:177602, 2010.

[80] J. Analytis et al. Two-Dimensional Surface State in the Quantum Limit of a Topological Insulator. *Nature Physics*, 6:960–964, 2010.

[81] L. Liu et al. Spin-Torque Ferromagnetic Resonance Induced by the Spin Hall Effect. *Physical Review Letters*, 106:036601, 2011.

[82] C. Wang et al. Bias and Angular Dependence of Spin-Transfer Torque in Magnetic Tunnel Junctions. *Physical Review B*, 79:224416, 2009.